



RENO: An Experiment  
for Neutrino Oscillation Parameter  $\theta_{13}$   
Using Reactor Neutrinos at Yonggwang

(Proposal and Technical Design Report)



March 11, 2010

## RENO Collaboration

J. K. Ahn,<sup>8</sup> S. R. Baek,<sup>12</sup> S. Choi,<sup>11</sup> Y. Choi,<sup>12</sup> I. S. Chung,<sup>1</sup> N. Danilov,<sup>6</sup> J. S. Jang,<sup>1</sup> E. J. Jeon,<sup>9</sup> K. K. Joo,<sup>1</sup> Y. H. Jung,<sup>7</sup> B. R. Kang,<sup>11</sup> W. K. Kang,<sup>9</sup> A. Kim,<sup>7</sup> B. C. Kim,<sup>1</sup> D. H. Kim,<sup>12</sup> H. S. Kim,<sup>2</sup> J. Y. Kim,<sup>1</sup> S. B. Kim,<sup>11\*</sup> S. H. Kim,<sup>1</sup> W. Y. Kim,<sup>7</sup> Y. D. Kim,<sup>9</sup> Yu. Krylov,<sup>5</sup> V. Kuznetsov,<sup>7</sup> H. S. Lee,<sup>8</sup> J. Lee,<sup>11</sup> I. T. Lim,<sup>1</sup> K. J. Ma,<sup>9</sup> G. Novikova,<sup>5</sup> Y. D. Oh,<sup>7</sup> M. Y. Pac,<sup>3</sup> C. W. Park,<sup>12</sup> J. S. Park,<sup>11</sup> K. S. Park,<sup>10</sup> J. W. Shin,<sup>11</sup> S. Stepanyan,<sup>7</sup> J. S. Suh,<sup>7</sup> E. Yanovich,<sup>5</sup> I. Yu,<sup>12</sup>

<sup>1</sup> Chonnam National University, Kwangju, 500-757, Korea

<sup>2</sup> Chonbuk National University, Jeonju, 561-756, Korea

<sup>3</sup> Dongshin University, Naju, 520-714, Korea

<sup>4</sup> Gyeongsang National University, Jinju, 660-701, Korea

<sup>5</sup> Institute for Nuclear Research, Moscow, 117312, Russia

<sup>6</sup> Institute of Physical Chemistry and Electrochemistry, Moscow, 117071, Russia

<sup>7</sup> Kyungpook National University, Taegu, 702-701, Korea

<sup>8</sup> Pusan National University, Pusan, 609-753, Korea

<sup>9</sup> Sejong University, Seoul, 143-747, Korea

<sup>10</sup> Seokyeong University, Seoul, 136-704, Korea

<sup>11</sup> Seoul National University, Seoul, 151-742, Korea

<sup>12</sup> Sungkyunkwan University, Suwon, 440-746, Korea

\* Contact person: Soo-Bong Kim (sbkim@phya.snu.ac.kr)

# Project Summary

An experiment, RENO (*Reactor Experiment for Neutrino Oscillation*), is under construction to measure the smallest but yet to be measured neutrino mixing angle ( $\theta_{13}$ ) using anti-neutrinos emitted from the Yonggwang nuclear power plant in Korea with world-second largest thermal power output of 16.4 GW.

A high precision measurement of reactor anti-neutrino oscillation can be achieved by a multiple detector experiment because the experimental sensitivity would be nearly unaffected by the uncertainties related to anti-neutrino source and interaction <sup>1</sup>. Consideration of the RENO began in early 2004 based on “White Paper for a New Nuclear Reactor Neutrino Experiment” <sup>2</sup>. The Yonggwang site was chosen due to a large number of anti-neutrinos from the nuclear power plant at the site and a mountainous geography suitable for constructing underground detectors.

The experimental setup consists of two identical 16-ton Gadolinium loaded liquid scintillator detector located near and far from the reactor array to measure the deviations from the inverse square distance law. The near and far detectors are to be placed roughly 290 m and 1.4 km from the center of the reactor array, respectively. The near detector will be constructed at underground of a 70 m high hill and the far detector at underground of a 260 m high mountain.

The basic feature of RENO experiment is to search for energy dependent  $\bar{\nu}_e$  disappearance using two identical detectors for comparison of neutrino fluxes at two different locations. The detectors are necessary to be located underground in order to reduce backgrounds from cosmic rays and cosmic ray induced spallation products. The detectors need to be designed identically in order to reduce systematic uncertainties to 1% or less. Controlling of the relative detector efficiency, fiducial volume, and good energy calibration are critical to the successful measurement.

The construction of experimental halls and access tunnels for both near and far detector sites was completed in early 2009. The experiment is planned to start data-taking in mid 2010. An expected number of observed anti-neutrino is roughly 510 and 80 per day in the near detector and far detector, respectively. An estimated systematic uncertainty associated with the measurement is less than 0.6%. Based on three years of data, it would be sensitive to measure the neutrino mixing angle in the range of  $\sin^2(\theta_{13}) > 0.02$ . This sensitivity is ten times better than the current limit obtained by CHOOZ. The RENO collaboration is presently consists of 12 institutions from Korea and Russia. It anticipates more international institutions to join the experiment. The RENO experiment was approved by the Ministry of Science and Technology in Korea in May 2005.

A measurement of or stringent limit on  $\theta_{13}$  would be crucial as part of a long term program to measure the CP violation parameter of  $\delta$  using accelerators. A sufficient value of  $\theta_{13}$  mea-

---

<sup>1</sup>Yu. Kozlov, L. Mikaelyan, and V. Sinev, “*Two Detector Reactor Neutrino Oscillation Experiment Kr2Det at Krasnoyarsk. Status Report,*” Phys. Atom. Nucl. 66 (2003) 469-471; Yad. Fiz. 66 (2003) 497-499.

<sup>2</sup>K. Anderson *et al.* (2004), hep-ex/0402041.

sured in this reactor experiment would strongly motivate the investment required for a new round of accelerator based neutrino experiments.

# Contents

<b>1</b>	<b>Overview</b>	<b>8</b>
1.1	Experimental Goals and Descriptions . . . . .	8
1.2	Experimental Setup . . . . .	9
1.2.1	Yonggwang Nuclear Power Plant . . . . .	9
1.2.2	Near and Far Detectors . . . . .	11
1.2.3	Geographical Data . . . . .	12
1.2.4	Tunneling and Experiment Halls . . . . .	12
1.3	Site Survey . . . . .	12
1.4	RENO Detectors . . . . .	14
1.4.1	Neutrino Target, Gamma Catcher, and Acrylic Vessels . . . . .	16
1.4.2	Non-Scintillating Buffer and Stainless Steel Vessel . . . . .	17
1.4.3	PMT . . . . .	17
1.4.4	Veto System . . . . .	17
1.5	Time Scale . . . . .	17
<b>2</b>	<b>Physics Goals</b>	<b>20</b>
2.1	Motivation . . . . .	20
2.2	Neutrino Oscillations . . . . .	20
2.2.1	Neutrino Mixing . . . . .	20
2.2.2	Experimental Results of Neutrino Oscillation . . . . .	21
2.3	Mixing Angle $\theta_{13}$ . . . . .	22
2.3.1	Current Knowledge of $\theta_{13}$ . . . . .	22
2.3.2	Significance of $\theta_{13}$ . . . . .	22
2.4	Reactor Neutrino Experiment . . . . .	25
2.4.1	Reactor Neutrinos . . . . .	25
2.4.2	Inverse Beta Decay . . . . .	25
2.4.3	Neutrino Oscillations in Reactor Experiments . . . . .	27
2.5	Determination of $\theta_{13}$ . . . . .	29
2.5.1	Measurement of Reactor Neutrino Flux . . . . .	29
2.5.2	Effects on Reactor Neutrino Flux Due to $\theta_{13}$ . . . . .	30
2.5.3	Experimental Extraction of $\theta_{13}$ . . . . .	31
2.6	Additional Physics . . . . .	34
2.6.1	Supernova Neutrinos . . . . .	34
2.6.2	Sterile Neutrinos . . . . .	34
2.6.3	Mass Varying Neutrinos . . . . .	35
2.6.4	Geo-neutrinos . . . . .	35
2.6.5	Precise Measurement of $\theta_{12}$ . . . . .	36
2.6.6	Reactor Physics . . . . .	36

2.6.7	Study of the Directionality . . . . .	37
<b>3</b>	<b>Detector</b>	<b>41</b>
3.1	Overview . . . . .	41
3.2	Target and Gamma Catcher . . . . .	42
3.2.1	Structure . . . . .	42
3.2.2	Acrylic Vessels . . . . .	43
3.2.3	Chimney . . . . .	44
3.3	Buffer . . . . .	44
3.4	Veto System . . . . .	46
3.4.1	Design Criteria . . . . .	46
3.4.2	Structure . . . . .	46
3.5	Detector Assembly . . . . .	47
3.6	PMT and HV System . . . . .	48
3.6.1	PMT Requirements and Specification . . . . .	48
3.6.2	Tests on PMT performance . . . . .	48
3.6.3	PMT Holder . . . . .	51
3.6.4	HV system . . . . .	51
3.7	Prototype Detector . . . . .	53
3.7.1	Detector Design . . . . .	53
3.7.2	Liquid Scintillator Mixture . . . . .	55
3.7.3	Electronics, Trigger, and DAQ Systems . . . . .	56
3.7.4	Performance . . . . .	56
3.8	Mock-up Detector . . . . .	56
3.8.1	Design of the Mock-up Detector . . . . .	56
3.8.2	Performance of Mock-up Detector . . . . .	58
3.9	DAQ System for Mock-Up Detector . . . . .	59
<b>4</b>	<b>Liquid Scintillator</b>	<b>62</b>
4.1	Introduction . . . . .	62
4.2	Liquid Scintillator and Buffer Fluids . . . . .	62
4.2.1	Specification . . . . .	63
4.2.2	Organic Solvent . . . . .	63
4.2.3	Various Fluors . . . . .	64
4.2.4	Target . . . . .	65
4.2.5	Synthesis of Gd-Complex . . . . .	66
4.2.6	Gamma Catcher . . . . .	67
4.2.7	Buffer . . . . .	67
4.3	Fluor and Wavelength Shifter . . . . .	68
4.4	Long-term Stability . . . . .	69
4.5	Material Compatibility . . . . .	69
4.6	R&D on LAB based Liquid Scintillator . . . . .	70
4.6.1	Introduction . . . . .	70
4.6.2	Purification of LAB . . . . .	71
4.6.3	LAB Composition Measurement with GC-MS . . . . .	72
4.6.4	Optical Properties . . . . .	73
4.6.5	Titration of Gd Concentration . . . . .	76
4.7	Radiopurity . . . . .	76
4.8	Liquid Handling and Purification System . . . . .	77

<b>5</b>	<b>Front-End Electronics, DAQ, Trigger, and Slow Control</b>	<b>79</b>
5.1	Front-End Electronics . . . . .	79
5.1.1	Specification of RENO Electronics . . . . .	79
5.1.2	QBEE Board . . . . .	80
5.2	DAQ . . . . .	81
5.2.1	Data Readout and Run Control . . . . .	82
5.2.2	Event Builder . . . . .	82
5.2.3	Software Trigger . . . . .	83
5.3	Trigger . . . . .	83
5.3.1	Energy Threshold . . . . .	83
5.3.2	Event Building . . . . .	83
5.3.3	Online Software Trigger . . . . .	83
5.4	Slow Control and Monitoring . . . . .	84
<b>6</b>	<b>Monte Carlo Simulation</b>	<b>85</b>
6.1	Overview . . . . .	85
6.2	Event Generation . . . . .	85
6.2.1	Inverse Beta Decay Events . . . . .	85
6.2.2	Kinematics for Positron and Neutron . . . . .	86
6.2.3	Neutrino Flux . . . . .	87
6.3	Detector Simulation . . . . .	89
6.3.1	Software Tools . . . . .	90
6.3.2	Optical Photon Processes . . . . .	91
6.3.3	Event Reconstruction . . . . .	94
6.4	Optimization of the Detector Design . . . . .	97
6.4.1	Target Mass . . . . .	97
6.4.2	$\gamma$ -Catcher Thickness . . . . .	98
6.4.3	Buffer Thickness . . . . .	98
6.5	Detection Efficiencies and Uncertainties . . . . .	100
6.5.1	Introduction . . . . .	100
6.5.2	Positron Detection Efficiency . . . . .	100
6.5.3	Neutron Detection Efficiency . . . . .	102
6.5.4	Dead Time . . . . .	104
6.5.5	Summary . . . . .	104
6.6	Background Simulation . . . . .	105
6.6.1	Simulation of Muon Background . . . . .	105
6.6.2	External Neutron Background . . . . .	106
6.6.3	Radioactive Isotopes Induced by Cosmic Ray Muons . . . . .	108
6.6.4	Radioactive Backgrounds . . . . .	109
6.7	Summary of Backgrounds . . . . .	111
<b>7</b>	<b>Calibration</b>	<b>114</b>
7.1	Overview . . . . .	114
7.2	Radioactive Sources . . . . .	114
7.3	Light Sources . . . . .	115
7.4	Source Driving System . . . . .	115

<b>8 Systematic Uncertainties and Sensitivity</b>	<b>118</b>
8.1 Systematic Uncertainties . . . . .	118
8.1.1 Reactor Related Uncertainties . . . . .	118
8.1.2 Detector Related Uncertainties . . . . .	120
8.1.3 Background Subtraction Uncertainties . . . . .	122
8.2 Sensitivity and Discovery Potentials . . . . .	122
8.2.1 Experiment Parameters . . . . .	122
8.2.2 Sensitivity . . . . .	123

# Chapter 1

## Overview

### 1.1 Experimental Goals and Descriptions

There has been great progress in understanding the neutrino sector of elementary particle physics in the last decade. The discovery of neutrino oscillations is a direct indication of physics beyond the Standard Model and it provides a unique new window to explore physics at high mass scale including unification, flavor dynamics and extra dimensions. The smallness of neutrino masses and the large lepton flavor violation associated with neutrino mixing are both fundamental properties that give insights into modifications of current theories. Since neutrino oscillations now have been established, the next step is to map out the parameters associated with neutrino masses and mixings. The experimental programme to accomplish this goal will require a wide range of experiments using neutrinos from solar, atmospheric, reactor, and accelerator sources.

In the presently accepted paradigm to describe the neutrino oscillations, there are three mixing angles ( $\theta_{12}$ ,  $\theta_{23}$ ,  $\theta_{13}$ ) and one phase angle ( $\delta$ ). There is now a world-wide experimental programme underway to measure the parameters associated with neutrino oscillations. One of the three mixing angles,  $\theta_{12}$ , is measured by solar neutrinos and the KamLAND experiment, and another,  $\theta_{23}$ , by atmospheric neutrinos and the long-baseline accelerator K2K experiment. Both angles are large, unlike mixing angles among quarks. MiniBooNE is searching for  $\nu_\mu \rightarrow \nu_e$  appearance signal in the LSND  $\Delta m^2$  region from 0.2 to 1.0 eV<sup>2</sup>. Current longer-baseline ( $\sim 700$  km) experiments are NuMI/MINOS at Fermilab and CNGS at CERN that will study  $\nu_\mu$  oscillations in the atmospheric  $\Delta m^2$  region. Several new long-baseline experiments are planned which will use off-axis beams including the approved J-PARC to Super-Kamiokande experiment (T2K) and the developing NuMI off-axis experiment (NO $\nu$ A). Following these experiments, the next stage might be neutrino superbeam experiments with even longer baseline that could possibly be combined with large proton decay detectors.

The third angle,  $\theta_{13}$ , has not yet been measured to be non-zero but is constrained to be small in comparison by the CHOOZ reactor neutrino experiment. Future measurement of  $\theta_{13}$  is possible using reactor neutrinos and accelerator neutrino beams. Reactor neutrino experiment can provide  $\theta_{13}$  measurement without the ambiguities associated with matter effects and CP violation. In addition, initially the reactor neutrino experiment does not necessarily have to have large detectors and it does not need construction of a neutrino beam line. The previous measurement had a single detector which was placed about 1 km from the reactors. Future reactor experiments using two detectors of 10 ~ 30 tons at near (100 ~ 500 m) and far (1 ~ 2 km) locations will have significantly improved sensitivity for  $\theta_{13}$  down to the  $\sin^2(2\theta_{13}) \sim 0.01$  level. With  $\theta_{13}$  determined, measurements of  $\nu_\mu \rightarrow \nu_e$  and  $\bar{\nu}_\mu \rightarrow \bar{\nu}_e$

oscillations using accelerator neutrino beams impinging on large detectors at long baselines will improve the knowledge of  $\theta_{13}$  and also allow access to matter or CP violation effects.

During the past several years, there have been competitively proposed several reactor neutrino experiments to measure  $\theta_{13}$ . They include a new experiment at Chooz called Double Chooz, the Braidwood experiment in the US, the KASKA experiment in Japan, the Daya Bay experiment in China and the RENO experiment in Korea. The experiments that have been approved for funding are summarized in Table 1.1.

The basic feature of this reactor experiment is to search for distance dependent  $\bar{\nu}_e$  disappearance using two or more detectors, for comparison of neutrino fluxes at two different locations. The detectors need to be located underground in order to reduce backgrounds from cosmic rays and cosmic ray induced spallation products. The detectors need to be designed identically in order to reduce systematic uncertainties to 1% or less. Controlling of the relative detector efficiency, fiducial volume, and good energy calibration are needed.

The Yonggwang nuclear power plant with world-second largest thermal power output of 16.4 GW, is an intense source of low energy anti-neutrinos suitable for measuring neutrino oscillations due to  $\theta_{13}$ . The anti-neutrino fluxes from the nuclear reactors are measured nearby before their oscillations, and measured again at a distance of about 1.4 km away from the reactor center. A neutrino mixing parameter  $\theta_{13}$  is obtained by finding the reduction of neutrino fluxes by comparison of the two measured fluxes.

The experimental setup consists of two 16 ton liquid scintillator detectors with one at a near site, roughly 290 m away from the reactor array center, and the other at a far site, roughly 1.4 km away from the reactor array center. The near detector will be located at underground of a 70 m high hill, and the far detector at underground of a 260 m high mountain.

It is now widely recognized that the possibility exists for a rich programme of measuring CP violation and matter effects in future accelerator based neutrino experiments, which has led to intense efforts to consider new programmes at neutrino superbeam, off-axis detectors, neutrino factories, and beta beams. However, the possibility of measuring CP violation can be fulfilled only if the value of neutrino mixing parameter  $\theta_{13}$  is such that  $\sin^2(2\theta_{13})$  should be greater than the order of 0.01. It is believed that a timely new experiment using nuclear reactors, sensitive to the neutrino mixing parameter  $\theta_{13}$  in this range has a great opportunity for an exciting discovery.

A measurement of or stringent limit on  $\theta_{13}$  would be crucial as a part of a long term programme to measure CP violation parameters at accelerators, even though a reactor  $\bar{\nu}_e$  disappearance experiment does not measure any CP violation parameter. A sufficiently large value of  $\theta_{13}$  measured in this reactor experiment would strongly motivate the investment required for a new round of accelerator neutrino experiments. A reactor experiment's unambiguous measurement of  $\theta_{13}$  would also strongly support accelerator based measurements by helping to resolve degeneracies and ambiguities. The combination of measurements from reactors and accelerator neutrino beams will allow early probe for CP violation without the necessity for long running at accelerators with anti-neutrino beams.

## 1.2 Experimental Setup

### 1.2.1 Yonggwang Nuclear Power Plant

The Yonggwang nuclear power plant is located in the west coast of southern part of Korea, about  $\sim 250$  km from Seoul as shown in Fig. 1.1. The power plant has six reactors producing total thermal output of 16.4 GW<sub>th</sub>, the second largest in the world. The reactors at the Yonggwang nuclear power plant are Pressurized Water Reactors (PWR). There are six reactors

Experiment	Location	Total Reactor Thermal Output (GW <sub>th</sub> )	Detector Distance Near/Far (m)	Overburden Near/Far (mwe)	Target Mass (Near/Far) (tons)
Double Chooz	France	8.7	410/1067	115/300	10/10
Daya Bay	China	11.6(17.4)	360(500)/1985(1613)	260/910	40 × 2/10
RENO	Korea	16.4	292/1380	110/450	16.1/16.1

Table 1.1: Planned reactor based neutrino oscillation experiments around the world. The detector distance represents the distance of the detector from the center of the reactor group(s).



Figure 1.1: Yonggwang nuclear power plant. The power plant is located about 250 km south of Seoul. Three other nuclear power plant sites in Korea are also shown.

and the reactor units 1 and 2 are of the Combustion Engineering (CE, now Westinghouse) System 80 design. Units 3 to 6 are of the Korean Standard Nuclear Power Plant (KSNP) design, which incorporates many improvements on the CE System 80. The first reactor, unit 1, became operational in 1986 and the last one, unit 6, in 2002. These reactors are lined up in roughly equal distances and spans  $\sim 1.3$  km as shown in Fig. 1.2.

A reactor core is comprised of 177 fuel assemblies and 73 control element assemblies. The fuel assemblies are arranged to form a cylinder with an equivalent diameter of 3.12 m and an active length of 3.81 m. Reactor fuelling cycle varies from 12 months to 24 months and refuellings are done with the plant shutdown. The fuel is a low enrichment UO<sub>2</sub> type supplied by Korea Nuclear Fuel Co., Ltd.

The average total thermal power output of the six reactor cores is 16.4 GW<sub>th</sub> with each reactor core generating about equal power. The average cumulative operating factors for all reactors are above 90%. The power plant is operated by Korea Hydro & Nuclear Power Co. Ltd. (KHNP).



Figure 1.2: The layout of the Yonggwang experiment site. Red dots and yellow dots represent reactors and detectors, respectively. Six reactors are roughly equally spaced in a 1280 m span. The near and far detectors are 290 m and 1380 m away from the reactor array, respectively. The image taken from Google Earth™ and copyrighted therein.

Reactor No.	Near Detector (m)	Far Detector (m)
1	667.9	1556.5
2	451.8	1456.2
3	304.8	1395.9
4	336.1	1381.3
5	513.9	1413.8
6	739.1	1490.1

Table 1.2: Distances of the reactor cores from the near and far detectors.

### 1.2.2 Near and Far Detectors

One of the main sources of systematic uncertainties is the uncertainty in the number of antineutrinos coming from the reactors. To minimize the effects of this problem, two identical detectors, near and far detectors are needed. Each detector will contain  $18.7 \text{ m}^3$  of liquid scintillator target doped with 0.1% of Gadolinium by weight (see Chapter 3).

Figure 1.2 shows the layout of six reactors and two detectors and Table 1.2 shows the distances between reactors and detectors. The near and far detectors are to be located 290 m and 1400 m from the center of the reactor array, respectively. The near detector is to be under an 70 m (AMSL) ridge with an overburden of  $\sim 110 \text{ mwe}$  whereas the far detector is to be located under a 260 m mountain with the overburden of  $\sim 450 \text{ mwe}$  as shown in Figs. 1.2 and 1.3.

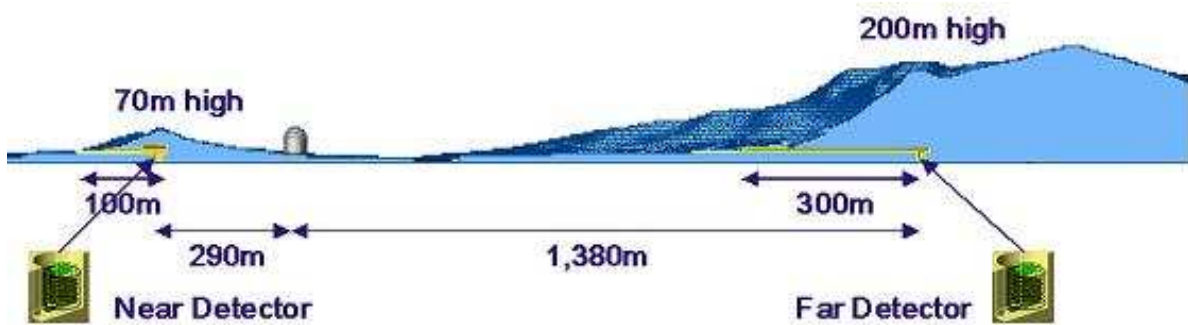


Figure 1.3: Overall side view of RENO experiment. The near detector is under a 70 m hill located within the perimeter of the power plant whereas the far detector is located under a 200 m mountain near the power plant.

### 1.2.3 Geographical Data

An interesting feature of RENO is having a sufficient overburden for the near detector due to a 70 m hill of  $2.8 \text{ g/cm}^3$  rock which is quite close (290 m) to the center of the reactor array. A detector close to the nuclear reactor is necessary for cancelling the systematic uncertainties related to the nuclear reactors such as ambiguities of the anti-neutrino flux and spectrum, as well as for reducing systematic uncertainties related to the detector and to the event selection. The near detector laboratory will be located inside the restricted area of the Yonggwang nuclear power plant.

### 1.2.4 Tunneling and Experiment Halls

The underground laboratories are constructed with two horizontal tunnels, 100 m long for the near detector and 300 m long for the far detector, as shown in Fig. 1.3. The tunnels are constructed using NATM (New Austrian Tunneling Method). The tunnel plan and schematic of experimental hall are shown in Fig. 1.4

The access tunnels are 95 m and 272 m long for near and far detector sites, respectively. The cross section of the access tunnel is shown in Fig. 1.4. The gradient toward the experimental hall is 0.3% for both tunnels for natural drainage. It is designed to accommodate the passage of a 10 ton truck.

## 1.3 Site Survey

To check the suitability of constructing experimental halls and access tunnels at the experiment site, geological surveys were performed. The site surveys were conducted by Daewoo Engineering Co., Ltd. in May, 2007.

The rocks at the experimental site are precambrian granite gneiss covered with Cretaceous plutonic rocks forming unconformity between the layers. There are fault lines near the site running north-south.

Two methods are used in the geophysical survey of the site; electrical resistivity survey and seismic refraction imaging. Figure 1.5 shows the locations of the survey done at the experimental site. The electrical resistivity survey results are shown in Fig. 1.6. The resulting rock classification maps are shown in Fig. 1.7.

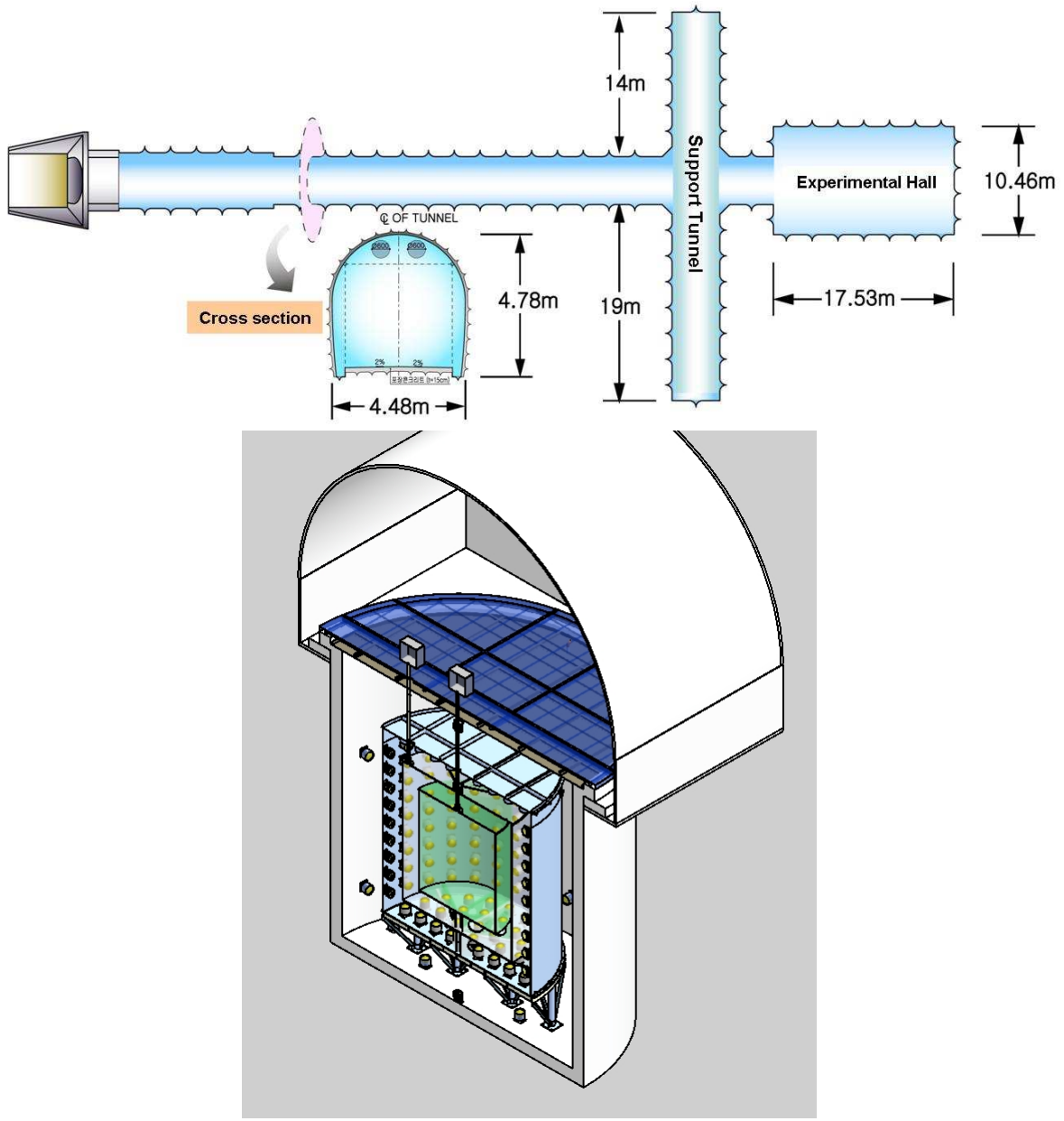


Figure 1.4: Plan of the access tunnel (top) and 3D schematic for experimental hall (bottom). The tunnels are constructed using NATM.

Most of tunneling sections at both near and far detector sites contains hard rocks of class II and III except near the entrance of the tunnels as shown in Fig. 1.7. Also no significant faults are found along the tunnels.

Based on the results from the electrical resistivity survey and the seismic refraction tests, four borehole positions and three borehole positions are selected for near and far detector sites, respectively. Figure 1.8 shows the rock samples from boreholes. The samples are used to determine various properties of rocks, such as chemical composition, compressive strength, density, and radioactivities.

Four on-site tests at the boreholes were also performed: televiewer, borehole loading, hy-

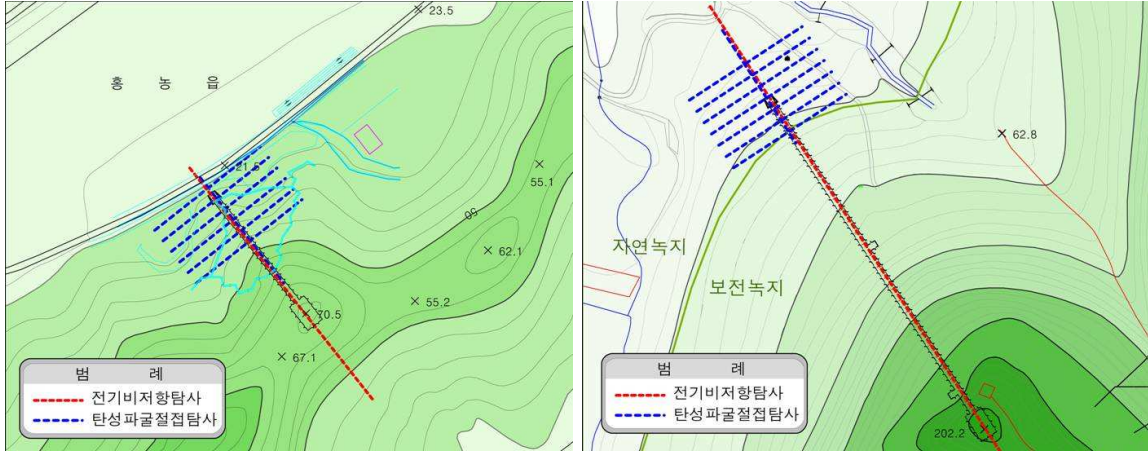


Figure 1.5: Locations of the electrical resistivity survey (red) and seismic refraction test (blue) performed in near (left) and far (right) detector sites.

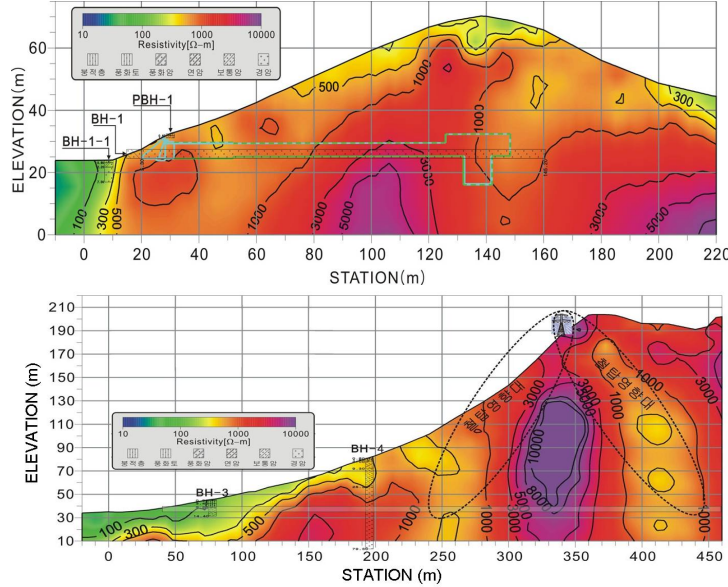


Figure 1.6: Electrical resistivity survey results at the near (top) and far (bottom) detector sites along the access tunnel.

draulic fracture, and downhole.

## 1.4 RENO Detectors

Both RENO near and far detectors will consist of a cylindrical target of 140 cm in radius and 320 cm in height, providing a volume of 18.7 m<sup>3</sup>. Identical arrangement of the near and far detectors will significantly reduce the systematic errors of relative normalization to 0.6%. However, they will have different cosmic ray background levels because of unequal overburdens ( $\sim 110$  mwe vs.  $\sim 450$  mwe). Although the near detector will suffer from higher cosmic ray background, it will observe much more signal events of reactor anti-neutrinos due to shorter distance from the nuclear cores and thus allows a high signal-to-background ratio. A detailed

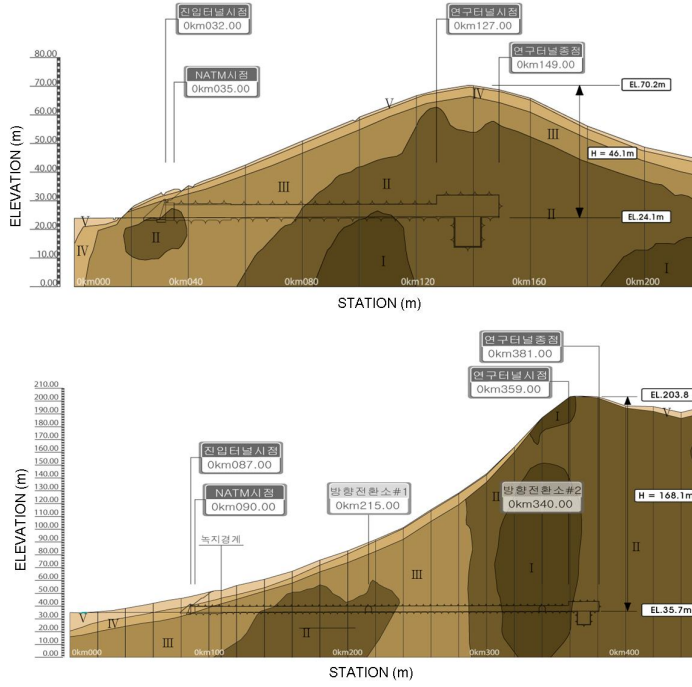


Figure 1.7: Rock classification maps of the near (top) and far (bottom) detector sites along the access tunnel.



Figure 1.8: Borehole rock samples from the near and far detector sites.

description of the backgrounds at both sites is given in Sect. 6.6.

The RENO detector consists of a neutrino target, a gamma catcher, a buffer and a veto. Target and gamma catcher vessels will be made from acrylic plastic material, having transparency to the light of wavelengths above 400 nm. The acrylic vessels should hold aromatic liquids without leakage and its properties should not change for the duration of the experiment.

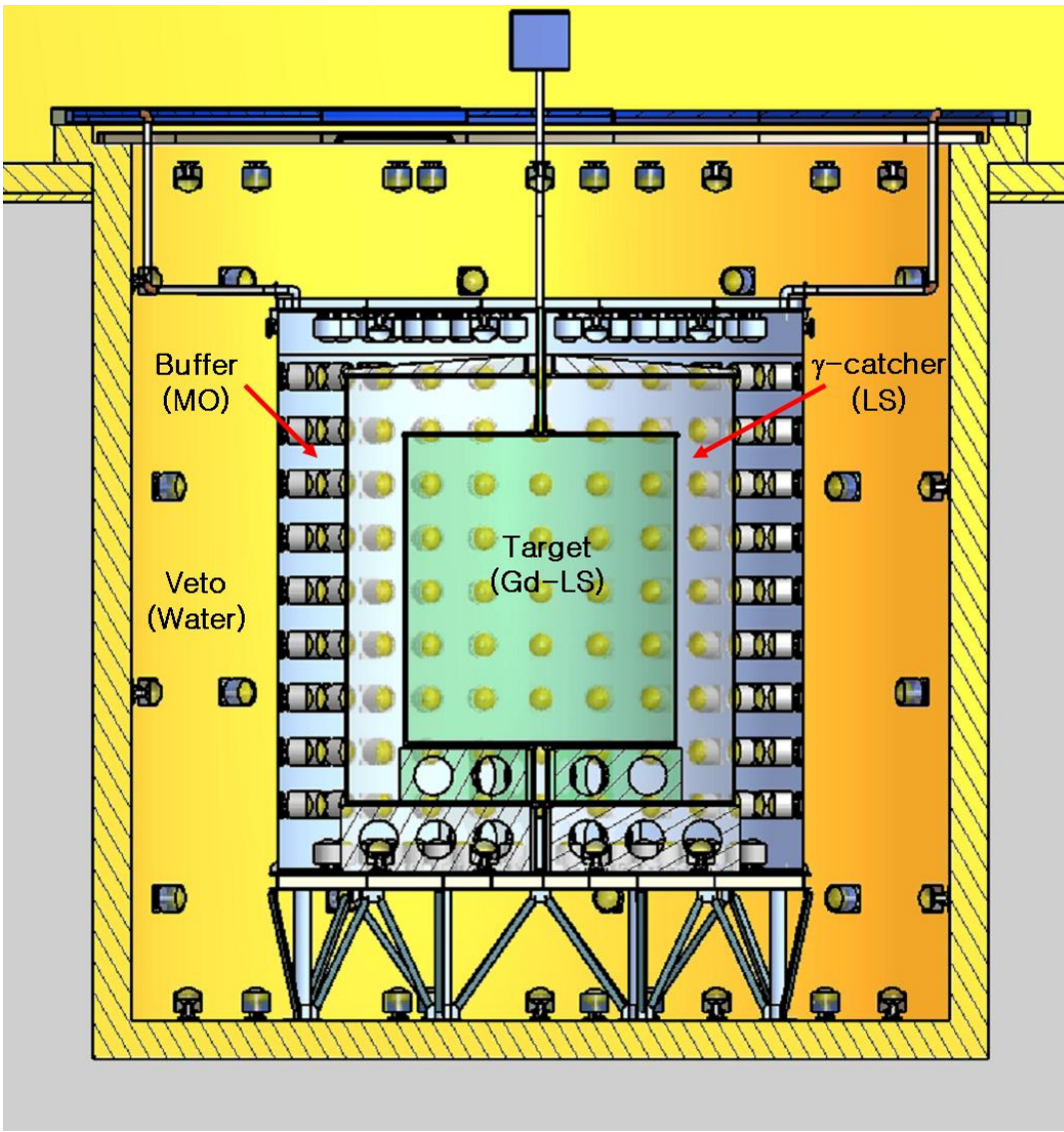


Figure 1.9: A schematic view of RENO detector. A neutrino target of  $18.7 \text{ m}^3$  Linear Alkyl Benzene (LAB) based liquid scintillator doped with Gd is contained in a transparent acrylic vessel, and surrounded by  $33.2 \text{ m}^3$  unloaded liquid scintillator of gamma catcher and  $76.5 \text{ m}^3$  non-scintillating buffer. There are 354 and 67 10-inch PMTs mounted on buffer and veto vessel walls, respectively.

They should not develop any chemical reaction with the scintillating liquids of neutrino target, gamma catcher and buffer for a long time period. Overview of each detector component is given below.

#### 1.4.1 Neutrino Target, Gamma Catcher, and Acrylic Vessels

The neutrino target consists of 0.1% Gd loaded liquid scintillator in a cylindrical acrylic container of 140 cm in radius, 320 cm in height, and 25 mm in thickness. It has a total volume of  $18.7 \text{ m}^3$  and a target mass of 16.1 tons. Gamma catcher surrounds the neutrino target with 60 cm thick *unloaded* liquid scintillator of  $33.2 \text{ m}^3$  in volume and 28.5 tons in mass. The gamma

Parameter	Value	Description
Thermal Power (GW)	16.4(average)/17.3(peak)	6 reactor
Target Size (ton)	16 (near/far)	Gd loaded Liquid Scintillator
PMT Coverage	14% (near/far)	surface area
Baseline Distance(m)	292 (near)/1380 (far)	
Overburden (mwe)	110 (near)/450 (far)	Vertical
Number of Events per Year	$2.6 \times 10^5$ (near)/ $3.0 \times 10^4$ (far)	$\epsilon_{total} = 56\%(\text{near})/72\%(\text{far})$
90% CL Sensitivity (3 years)	$\sin^2(2\theta_{13}) \sim 0.02 - 0.03$	$\Delta m_{13}^2 = (2 - 3) \times 10^{-5} \text{ eV}^2$

Table 1.3: Summary of RENO experimental parameters.

catcher is contained in a cylindrical acrylic vessel of 200 cm in radius, 440 cm in height, and 30 mm in thickness. The gamma catcher vessel should be chemically compatible with mineral oil of the buffer region as well as the scintillating liquids inside. This scintillating volume is necessary for efficient tagging of the gammas from neutron capture by Gd and from positron annihilation, and for rejecting the backgrounds from the fast neutrons.

#### 1.4.2 Non-Scintillating Buffer and Stainless Steel Vessel

A 70 cm thick non-scintillating liquid surrounds the gamma catcher to reduce the accidental backgrounds coming from outside (mainly from radioactivity in the photomultiplier tubes), by almost two orders of magnitude. A total of  $76.5 \text{ m}^3$  (64.2 tons) mineral oil is contained in a stainless steel vessel of 270 cm in radius, 580 cm in height, and 6-12 mm in thickness. This buffer is necessary for keeping the background single rate below 10 Hz in the neutrino target and gamma catcher regions.

#### 1.4.3 PMT

A total of 354 10-inch photomultipliers in a uniformly distributed array are mounted on the inner surface of the buffer vessel, providing a 14% photo-sensitive surface area coverage. The cylindrical stainless steel vessel optically isolates the inner detector part from the outer veto system.

#### 1.4.4 Veto System

A 1.5 m thick water layer of 353 tons surrounds the whole inner detector. A total of 67 10-inch PMTs are mounted on a cylindrical concrete tank painted with Titanium Oxide ( $\text{TiO}_2$ ) reflector. It is used for vetoing cosmic muons and reducing backgrounds coming from its surrounding rock.

Some of detector parameters or design may be changed afterwards according to the result of detection performance studies using a mock-up detector. A list of interesting parameters for the RENO experiment is given in Table 1.3. Some of RENO experimental parameters are compared with those of Double Chooz and Daya Bay experiments in Table 1.1.

### 1.5 Time Scale

An overall schedule of the RENO experiment is given in Fig. 1.10. The KHPN, the company operating the Yonggwang nuclear power plant, has allowed us to carry out the experiment in the Yonggwang's restricted area. The local government and residents have also expressed their

best cooperation for RENO. A company for geological survey and tunnel design was chosen through a bidding process in Feb, 2007. Civil construction for underground facility began in July 2008 and was completed in Feb. 2009. RENO has gone through rapid development stages, to date, of project planning, fund approval, administrative negotiation, and detector design. This was possible only due to the great worldwide interest in finding  $\theta_{13}$ . Excavation of two tunnels and construction of underground facility was completed in late 2008. Construction of both near and far detectors will be completed by mid-2010. Data taking is expected to start shortly afterward. RENO will reach  $\sin^2(2\theta_{13})$  sensitivity of 0.03 with a year of data in 2011, and 0.02 with three years of data, corresponding to the luminosity of 400 ton·GW·yr, in 2013. The sensitivity will rely on the evaluated systematic errors and background levels.

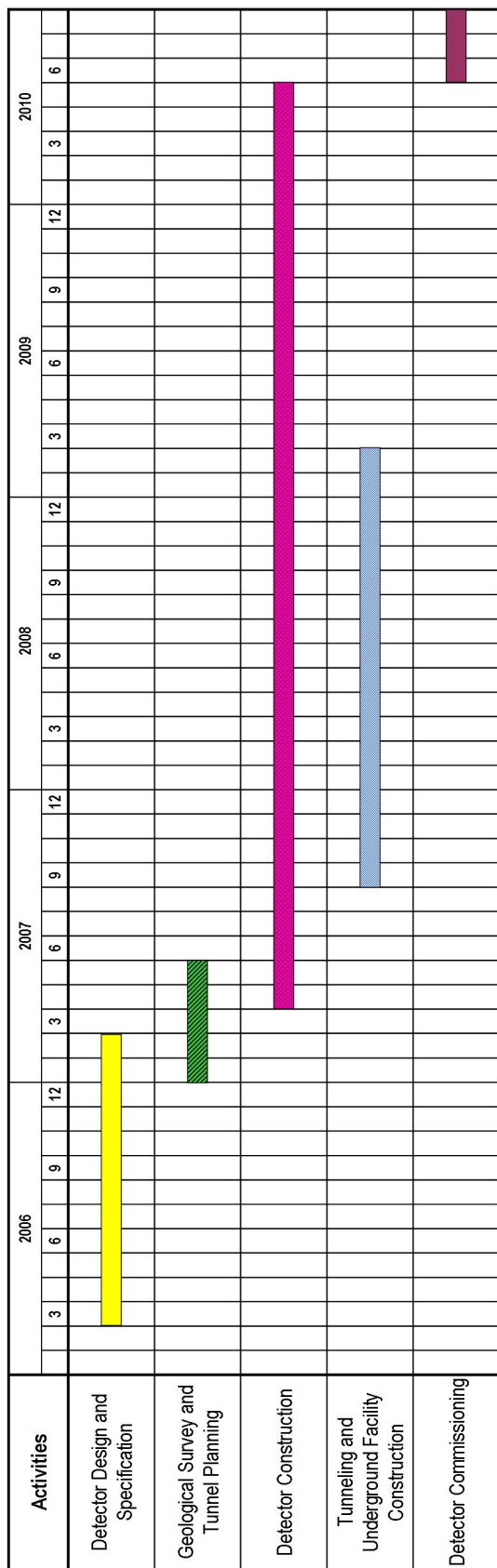


Figure 1.10: RENO construction schedule.

# Chapter 2

# Physics Goals

## 2.1 Motivation

As stated earlier,  $\theta_{13}$  is a key parameter in developing the future neutrino oscillation program. In addition to the general physics arguments, there is a point that brings urgency to the reactor neutrino experiments. Reactor experiments offer a straightforward and cost effective method to measure or constrain the value of  $\theta_{13}$ . The sensitivity of a two-detector experiment is comparable to that of the proposed initial off-axis long-baseline experiment. Since a reactor experiment would be relatively small and simple and use an existing reactor neutrino source with a well understood neutrino rate, it should be able to be done fairly quickly and at reduced costs. It is likely that such an early measurement of  $\theta_{13}$  will be necessary before the community invests a large amount of resources for a full off-axis measurement. For the longer term, a reactor neutrino experiment would be complementary to the off-axis experiments in separating the measurement of  $\theta_{13}$  from other physics parameters associated with matter effects and CP violation. A follow-up reactor experiment with much larger detectors at various baseline will continue to be an important component of the neutrino oscillation program.

It is now widely recognized that the possibility exists for a rich program of measuring CP violation and matter effects in future accelerator neutrino experiments, which has led to intense efforts to consider new programs at neutrino superbeams, off-axis detectors, neutrino factories, and beta beams. However, the possibility of measuring CP violation can be fulfilled only if the value of neutrino mixing parameter  $\theta_{13}$  is such that  $\sin^2(2\theta_{13})$  should be greater than or equal to the order of 0.01. It is believed that a timely new experiment using nuclear reactors sensitive to the neutrino mixing parameter  $\theta_{13}$  in this range would provide a great opportunity for an exciting discovery.

## 2.2 Neutrino Oscillations

### 2.2.1 Neutrino Mixing

Just as the CKM matrix parametrizes the mixing of the quark flavors, the neutrino flavor states can be related to the mass states through the MNS (Maki-Nakagawa-Sakata) lepton flavor mixing matrix assuming three flavors,

$$U = \begin{pmatrix} 1 & 0 & 0 \\ 0 & c_{23} & s_{23} \\ 1 & -s_{23} & c_{23} \end{pmatrix} \begin{pmatrix} c_{13} & 0 & s_{13}e^{i\delta} \\ 0 & 1 & 0 \\ -s_{13}e^{-i\delta} & 0 & c_{13} \end{pmatrix} \begin{pmatrix} c_{12} & s_{12} & 0 \\ -s_{12} & c_{12} & 0 \\ 0 & 0 & 1 \end{pmatrix} \quad (2.1)$$

$$= \begin{pmatrix} c_{12}c_{13} & s_{12}c_{13} & s_{13}e^{-i\delta} \\ -s_{12}c_{23} - c_{12}s_{23}s_{13}e^{i\delta} & c_{12}c_{23} - s_{12}s_{23}s_{13}e^{i\delta} & s_{23}c_{13} \\ s_{12}s_{23} - c_{12}c_{23}s_{13}e^{i\delta} & -c_{12}s_{23} - s_{12}c_{23}s_{13}e^{i\delta} & c_{23}c_{13} \end{pmatrix},$$

where  $c_{ij} = \cos \theta_{ij}$ ,  $s_{ij} = \sin \theta_{ij}$ , and  $\delta$  is a Dirac  $CP$  violating phase. The mixing angle  $\theta_{12}$  has been probed by solar and reactor neutrino experiments and is often referred to as  $\theta_{sol}$ , while the angle  $\theta_{23}$  has been investigated by atmospheric neutrino experiments and it is often identified as  $\theta_{atm}$ . Reactor neutrino experiments have probed the mixing angle  $\theta_{13}$ . If the mixing angle  $\theta_{13}$  vanishes exactly, then the  $CP$  violating matrix elements vanish and the  $CP$  violation would not be observed in the lepton sector, independently of the value of the phase  $\delta$ .

The probability of  $\nu_\alpha$  with energy  $E$  changing to  $\nu_\beta$  ( $\nu_{\alpha,\beta} = \nu_{e,\mu,\tau}$ ) after travelling distance  $L$  in vacuum is

$$P(\nu_\alpha \rightarrow \nu_\beta) = \delta_{\alpha\beta} - 2\text{Re} \sum_{j>i} U_{\alpha i} U_{\alpha j}^* U_{\beta i}^* U_{\beta j} \left( 1 - \exp i\Delta m_{ji}^2 L \frac{2}{E} \right), \quad (2.2)$$

where  $\Delta m_{ji}^2 \equiv m_j^2 - m_i^2$  and  $m_i$  is the mass of the  $i$ th eigenstate.

The results from solar neutrino experiments and a long baseline reactor experiment favor large mixing angle MSW solar solution with  $\Delta m_{21}^2 = m_2^2 - m_1^2 = \Delta m_{sol}^2 > 0$ , where  $m_1$  is the mass eigenstate with a larger electron neutrino component [1, 2, 3]. The large quadratic mass difference measured in the atmospheric neutrino experiment is therefore the mass splitting between eigenstate 3 and more closely spaced states 1 or 2. And it is unknown what the sign of the splitting between the state 3 and states 1 or 2 is. This leads to an ambiguity in the sign of  $\Delta m_{32}^2 = m_3^2 - m_2^2 = \Delta m_{atm}^2$ . A further theoretical description of neutrino mixing can be found in Ref. [4].

### 2.2.2 Experimental Results of Neutrino Oscillation

Various experiments using solar, atmospheric, reactor and accelerator neutrinos have observed oscillations among different flavors of neutrinos, providing rich information on the flavor structure of the lepton sector [5, 6, 7, 8, 9]. Based on a global analysis with  $\pm 2\sigma$  ( $\sim 95\%$  C.L.) ranges [11], neutrino oscillation data have determined; (1)  $\sin^2 \theta_{12}$  to 18% and  $\Delta m_{21}^2$  to 9%, (2)  $\sin^2 \theta_{23}$  to 41% and  $\Delta m_{32}^2$  to 26%, and (3) upper bounds on  $\theta_{13}$  due to null oscillation results. The  $CP$  phase angle  $\delta$  will be likely hard to measure with current and near future oscillation experiments. The results from the global fits are as follows:

$$\begin{aligned} \sin^2 \theta_{13} &= 0.009^{+0.023}_{-0.009} \\ \sin^2 \theta_{12} &= 0.314(1^{+0.18}_{-0.15}) & \Delta m_{21}^2 &= 7.92(1 \pm 0.09) \times 10^{-5} \text{ eV}^2 \\ \sin^2 \theta_{23} &= 0.44(1^{+0.41}_{-0.22}) & \Delta m_{32}^2 &= 2.4(1^{+0.21}_{-0.26}) \times 10^{-3} \text{ eV}^2. \end{aligned} \quad (2.3)$$

Another global analysis [10] including the first MINOS results has found similar oscillations parameters that overlap significantly with the above results. There are three unmeasured neutrino oscillation parameters of  $\theta_{13}$ , the Dirac  $CP$  phase  $\delta_{CP}$ , and the sign of  $\Delta m_{32}^2$  that determines the hierarchy of neutrino masses. Based on the measured mixing angles, the MNS matrix can be approximately written by

$$U \simeq \begin{pmatrix} 0.8 & 0.5 & < 0.2 \\ 0.4 & 0.6 & 0.7 \\ 0.4 & 0.6 & 0.7 \end{pmatrix} \quad (2.4)$$

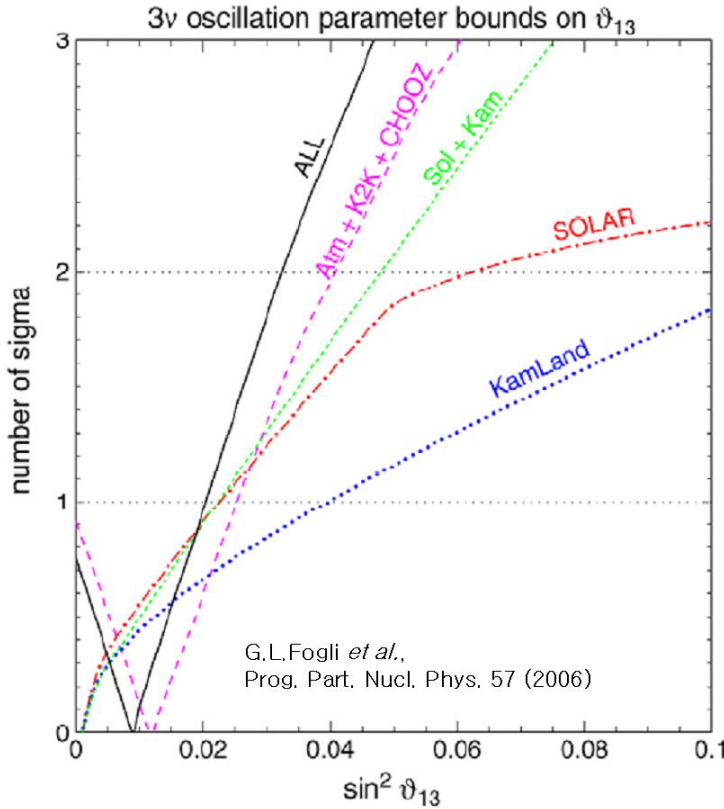


Figure 2.1: Bounds on  $\sin^2 \theta_{13}$  for different data sets. This figure is taken from Ref. [11].

The elements of the MNS matrix are quite different from those of the CKM matrix which is nearly diagonal. The  $U_{e3}$  element including  $\sin^2 \theta_{13}$  is small compared to other elements. This peculiar feature needs to be explained by the unified theory of elementary particles and thus the smallness of  $\theta_{13}$  may play an important role when constructing the unified theory.

## 2.3 Mixing Angle $\theta_{13}$

### 2.3.1 Current Knowledge of $\theta_{13}$

Figure 2.1 in Ref. [11] shows several fit results of  $\theta_{13}$  based on different inputs. Those fits with solar and atmospheric experiments separately favor values near  $\sin^2 \theta_{13} = 0$ , but their global analyses together find minimum  $\chi^2$  at non-vanishing values of  $\theta_{13}$  as listed above. The other global fit also has obtained a similar bound on  $\theta_{13}$  as shown in Fig. 2.2 [10].

At 95% C.L., the upper bound of  $\sin^2 2\theta_{13}$  from Ref. [11] is approximately 0.12, corresponding to the  $\theta_{13}$  value of  $10^\circ$ . This could be compared to the upper limit of 0.17 at 90% C.L. obtained by CHOOZ [8]. The mixing angle  $\theta_{13}$  is very small compared to  $\theta_{12}$  and  $\theta_{23}$ .

### 2.3.2 Significance of $\theta_{13}$

Genuine three flavor oscillation effects occur only for a finite value of  $\theta_{13}$ . Therefore, it is necessary to measure a finite value of  $\theta_{13}$  as one of the next milestones in further studies of neutrino oscillations. In addition,  $\theta_{13}$  is important in theoretical model building of neutrino

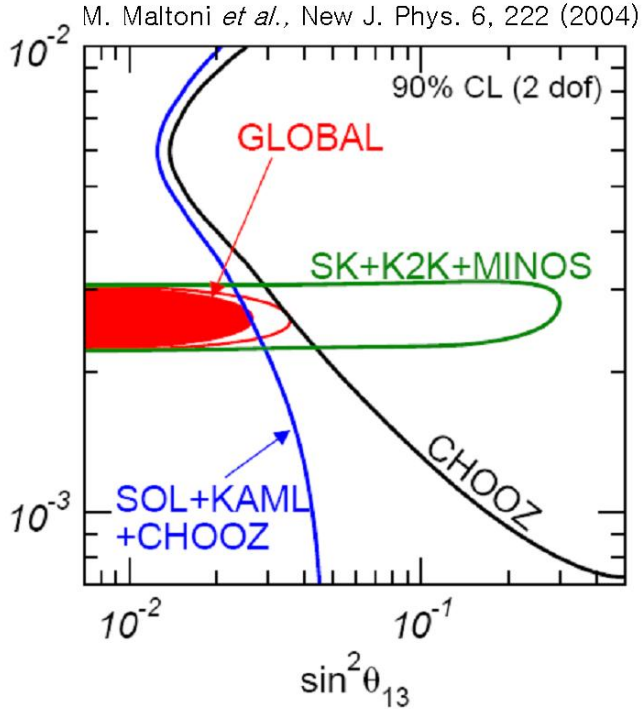


Figure 2.2: Bounds on  $\sin^2 \theta_{13}$  from the interplay of the global data. This figure is taken from Ref. [10].

mass matrix, which can serve as a guide to the theoretical understanding of physics beyond the Standard Model.

Leptonic CP violation is also a three flavor effect, but it can only be tested if  $\theta_{13}$  is finite. The CP phase angle  $\delta_{CP}$  appears always in the combination  $U_{e3} = \sin \theta_{13} e^{-i\delta_{CP}}$ . If  $\theta_{13}$  is zero then it is not possible to probe leptonic CP violation in neutrino oscillation experiments. If  $\sin^2(2\theta_{13}) > 0.01$ , then the design of experiments to measure the sign of  $\Delta m_{32}^2$  and the CP phase  $\delta_{CP}$  becomes straightforward extensions of current experiments [13, 14]. For this reason, there is a strong motivation that a  $\theta_{13}$  measurement should be the prime goal of the next round of experiments [15].

On the theoretical side it is quite interesting to know if the value of  $\theta_{13}$  happens to be small without any reason or has some theoretical backgrounds such as some symmetry argument being required to explain a tiny value. A reason for expecting a particular value of  $\theta_{13}$  does not clearly exist as long as one extends the SM only minimally to accommodate neutrinos masses.  $\theta_{13}$  is then simply some unknown parameter which could take an arbitrary small value, including zero. The situation changes in models of neutrino masses. Even then one should acknowledge that in principle any value of  $\theta_{13}$  can be accommodated. Therefore, today there is no particular reason to expect the third angle,  $\theta_{13}$ , to be extremely small or even zero.

Some neutrino mass models often have a tendency to predict also a sizable value of  $\theta_{13}$ . This is the case for models in the framework of Grand Unified Theories and for models using flavor symmetries. There exist also many different texture models of neutrino masses and mixings, which accommodate existing data and try to predict the missing information by assuming certain elements of the mass matrix to be either zero or identical. In general, if  $\theta_{13}$  is not too small e.g., close to the current upper limit of  $\sin^2(2\theta_{13}) \simeq 0.01$  and  $\theta_{23} \neq \pi/4$ ,

Reference	$\sin \theta_{13}$	$\sin^2 2\theta_{13}$
<i>SO(10)</i>		
Goh, Mohapatra, Ng [40]	0.18	0.13
<i>Orbifold SO(10)</i>		
Asaka, Buchmüller, Covi [41]	0.1	0.04
<i>SO(10) + flavor symmetry</i>		
Babu, Pati, Wilczek [42]	$5.5 \cdot 10^{-4}$	$1.2 \cdot 10^{-6}$
Blazek, Raby, Tobe [43]	0.05	0.01
Kitano, Mimura [44]	0.22	0.18
Albright, Barr [45]	0.014	$7.8 \cdot 10^{-4}$
Maekawa [46]	0.22	0.18
Ross, Velasco-Sevilla [47]	0.07	0.02
Chen, Mahanthappa [48]	0.15	0.09
Raby [49]	0.1	0.04
<i>SO(10) + texture</i>		
Buchmüller, Wyler [50]	0.1	0.04
Bando, Obara [51]	0.01 .. 0.06	$4 \cdot 10^{-4} .. 0.01$
<i>Flavor symmetries</i>		
Grimus, Lavoura [52, 53]	0	0
Grimus, Lavoura [52]	0.3	0.3
Babu, Ma, Valle [54]	0.14	0.08
Kuchimanchi, Mohapatra [55]	0.08 .. 0.4	0.03 .. 0.5
Ohlsson, Seidl [56]	0.07 .. 0.14	0.02 .. 0.08
King, Ross [57]	0.2	0.15
<i>Textures</i>		
Honda, Kaneko, Tanimoto [58]	0.08 .. 0.20	0.03 .. 0.15
Lebed, Martin [59]	0.1	0.04
Bando, Kaneko, Obara, Tanimoto [60]	0.01 .. 0.05	$4 \cdot 10^{-4} .. 0.01$
Ibarra, Ross [61]	0.2	0.15
<i><math>3 \times 2</math> see-saw</i>		
Appelquist, Piai, Shrock [62, 63]	0.05	0.01
Frampton, Glashow, Yanagida [64]	0.1	0.04
Mei, Xing [65] (normal hierarchy)	0.07	0.02
(inverted hierarchy)	> 0.006	$> 1.6 \cdot 10^{-4}$
<i>Anarchy</i>		
de Gouvêa, Murayama [66]	> 0.1	> 0.04
<i>Renormalization group enhancement</i>		
Mohapatra, Parida, Rajasekaran [67]	0.08 .. 0.1	0.03 .. 0.04

Table 2.1: Various predictions of  $\theta_{13}$  based on different theoretical models taken from Ref. [13]. The reference numbers in the table are the reference numbers in Ref. [13].

the neutrino mass matrix does not have any special symmetry features, sometimes referred as anarchy models, and the specific values of  $\theta_{13}$  can be understood as a numerical accident. However, if  $\theta_{13}$  is much smaller than the current limit, special symmetry of neutrino mass matrix will be required. For a large value of  $\theta_{13}$ , it leaves open questions on quark-lepton unification. Summary of various predictions is shown in Table 2.1.

Altogether there exist very good reasons to push the sensitivity limit from the current CHOOZ value by an order of magnitude and to hope that a finite value of  $\theta_{13}$  will be found. But as already mentioned, at this precision even a negative result would be very interesting, since it would test or rule out many neutrino mass models and restrict parameters relevant for quantum corrections to masses and mixings.

Isotope	Mean Energy Per Fission (MeV)
$^{235}\text{U}$	$201.8 \pm 0.5$
$^{238}\text{U}$	$205.0 \pm 0.7$
$^{239}\text{Pu}$	$210.3 \pm 0.6$
$^{241}\text{Pu}$	$212.6 \pm 0.7$

Table 2.2: Mean energy emitted per fission for four main isotopes in nuclear fuel [17].

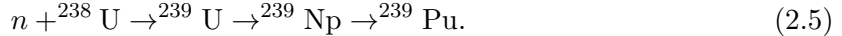
## 2.4 Reactor Neutrino Experiment

### 2.4.1 Reactor Neutrinos

Nuclear reactors have played crucial roles in experimental neutrino physics. The discovery of the neutrino was made at the Savannah River Reactor in 1956 by Reines and Cowan [16]. KamLAND observed disappearance of reactor antineutrinos and distortion in the energy spectrum because of neutrino oscillations due to mixing angle  $\theta_{12}$ . Furthermore, reactor neutrino experiments have the potential of uniquely determining  $\theta_{13}$  at a low cost and in a timely manner.

The Yonggwang nuclear power plant has six Pressurized Water Reactors (PWR), with average total thermal power output of  $16.4 \text{ GW}_{th}$ . The fissile material in the reactors mainly consists of  $^{235}\text{U}$  and  $^{239}\text{Pu}$ , which undergoes thermal neutron fission.

The dominant  $^{238}\text{U}$  is fissile only for fast neutrons but also undergoes fission process by thermal neutron capture and produces  $^{239}\text{Pu}$ ,



Similarly,  $^{241}\text{Pu}$  is generated from  $^{239}\text{Pu}$ ,



Four fissile isotopes,  $^{235}\text{U}$ ,  $^{239}\text{Pu}$ ,  $^{238}\text{U}$ , and  $^{241}\text{Pu}$ , are important and others contribute only at the 0.1% level. Fission fragments from these isotopes sequentially  $\beta$  decay and emit electron antineutrinos. The purity of the antineutrinos is very high and electron-neutrino contamination is only at a  $10^{-5}$  level above an inverse  $\beta$  decay threshold of 1.8 MeV.

The fission rates of the fissile isotopes are shown in Fig. 2.3. These four isotopes release similar energy, as shown in Table 2.2, when they undergo fission [17]. Therefore, even though the makeup of the fissile material in the reactor changes over a refuelling cycle, the average mean energy per fission does not change significantly. Assuming  $\sim 200$  MeV per fission, there are  $3.1 \times 10^{19}$  fissions per  $\text{GW}_{th}$ . Since one fission causes about six neutrino emissions above  $\sim 2$  MeV on average [19, 20, 21, 22], the neutrino intensity can be estimated to be  $\sim 2 \times 10^{20} / (\text{GW}_{th} \cdot \text{s})$ .

The neutrinos are radiated isotropically from the reactor core and, therefore, the inverse square law applied on the neutrino intensity at a distance. The neutrino energy spectrum from a reactor is shown in Fig. 2.5.

### 2.4.2 Inverse Beta Decay

When an electron antineutrino enters matter, it can be captured by a free proton via inverse neutron decay



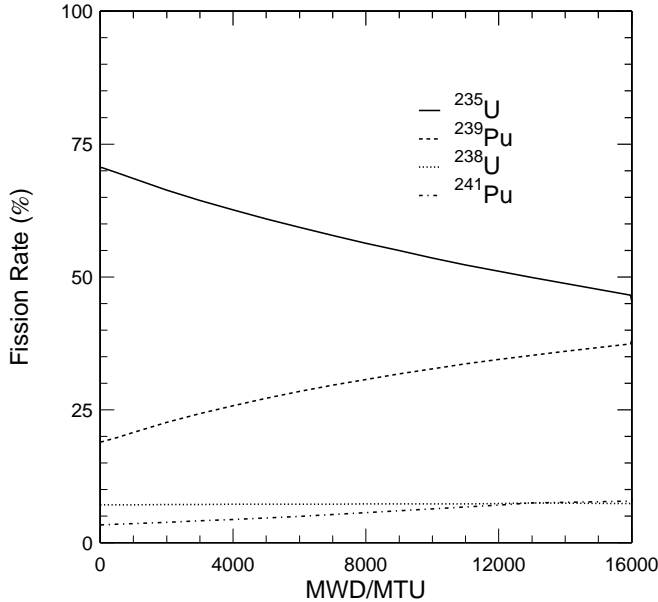


Figure 2.3: The evolution of fission rate of the four dominant fissile isotopes of a typical refuelling cycle. Courtesy of Ulchin Nuclear Power Plant Co.

which has an 1.8 MeV antineutrino energy threshold. The resulting neutron is subsequently captured by a proton in the following process:

$$n + p \rightarrow D + \gamma, \quad (2.8)$$

where  $D$  is a deuterium. The mean time for neutron capture is  $\sim 200 \mu\text{s}$ . The incident antineutrino energy is directly related to the energy of the positron by

$$E_{\bar{\nu}_e} = E_{e^+} + (m_n - m_p) + \mathcal{O}(E_{\bar{\nu}_e}/m_n), \quad (2.9)$$

where  $E_{e^+}$  is the energy of the positron coming out from the inverse neutron decay and  $m_n(m_p)$  is the neutron (proton) mass. The positron deposits its energy and then annihilates, yielding two photons each with 0.511 MeV, thus experimentally visible energy is  $(E_{e^+} + 0.511 \text{ MeV})$  with the minimum energy of 1.022 MeV. An electron antineutrino event then can be identified by a distinctive signature of a prompt positron signal followed by a photon from the delayed neutron capture.

However, if a neutron is captured by Gd in which a proton is bound, then the capture cross section becomes larger and additional gammas are produced to have total energy of about 8 MeV. The experimental signature for reactor neutrinos is a prompt energy deposit of 1-8 MeV, due to the positron kinetic energy and the annihilated  $e^+e^-$  masses, followed an average 30  $\mu\text{s}$  later by 8 MeV energy deposit of gammas from neutron capture on Gd. Exploiting the delayed coincidence is key to controlling backgrounds. Figure 2.4 shows both prompt and delayed signals produced by a reactor neutrino.

The inverse neutron decay process has the cross section of the form,

$$\sigma(E_{e^+}) \simeq \frac{2\pi^2\hbar^3}{m_e^5 f \tau_n} p_{e^+} E_{e^+}, \quad (2.10)$$

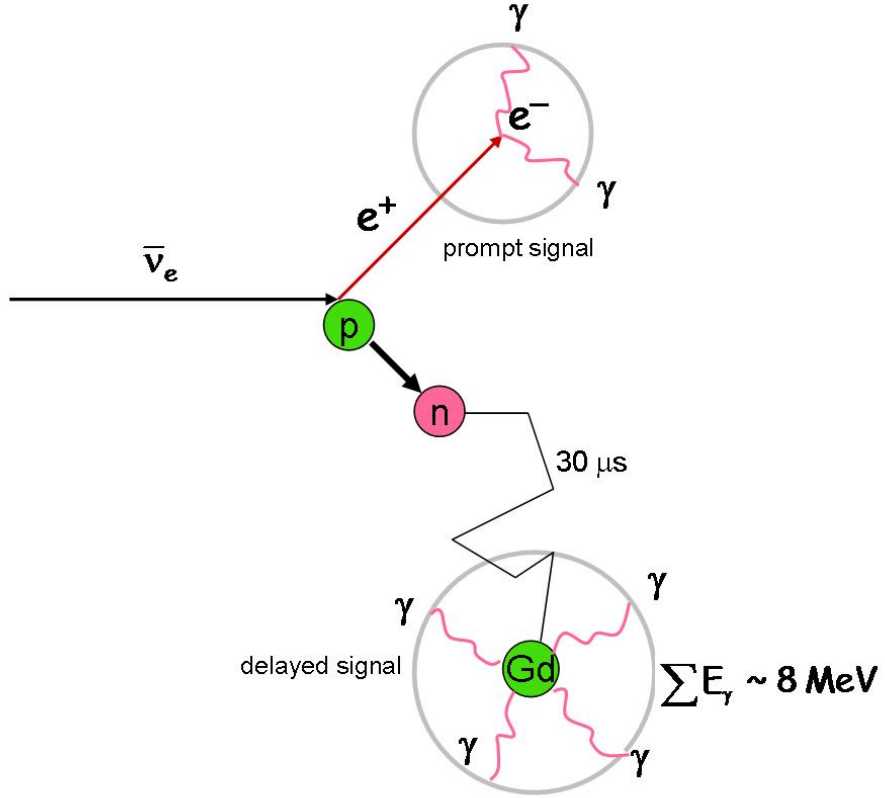


Figure 2.4: An electron antineutrino would be detected by a coincidence signal of a prompt positron and a delayed captured neutron. The neutrino energy is directly related to the measured energy of the outgoing positron.

where  $p_{e+}$  and  $m_e$  are the momentum and the mass of the positron, respectively,  $\tau_n$  is the lifetime of a free neutron, and  $f = 1.7152$  is the free neutron decay phase space factor [18].

Figure 2.5 shows the neutrino flux, inverse beta decay cross section, and interaction spectrum at a detector in arbitrary units calculated in Ref. [23]. The most probable neutrino energy interacting at a detector is  $\sim 3.8$  MeV.

#### 2.4.3 Neutrino Oscillations in Reactor Experiments

Because neutrinos from reactors have low energy of the order of a few MeV, they do not have enough energy to produce muons or taus through charged current interaction. Therefore, any reactor experiments can only be disappearance experiments, which measure the survival probability  $P(\bar{\nu}_e \rightarrow \bar{\nu}_e)$ .

It was shown in Ref. [24] that the survival probability does not depend on the  $CP$  phase  $\delta$ . And because of the low energy neutrinos and short baseline, matter effects are negligible in reactor experiments [25]. Thus one can use the neutrino survival probability in vacuum to model the neutrino oscillations in the reactor experiments. Assuming a mass hierarchy of

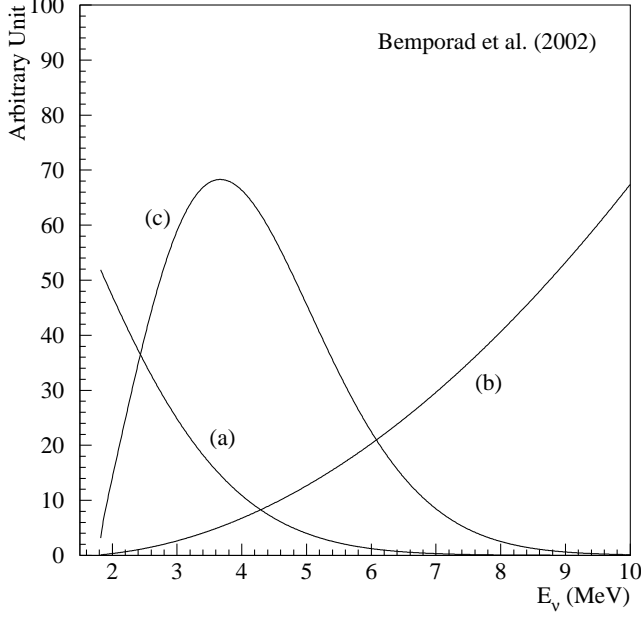


Figure 2.5: Reactor  $\bar{\nu}_e$  flux (a), inverse beta decay cross section (b), and interaction spectrum at a detector based on such reaction (c) in Ref. [23]. The cut-off at 1.8 MeV is due to the minimum neutrino energy required for inverse beta decay process.

$m_1 < m_2 < m_3$ , the expression for the  $\bar{\nu}_e$  disappearance probability is written as [25]

$$\begin{aligned}
1 - P(\bar{\nu}_e \rightarrow \bar{\nu}_e) &= 4 \sum_{j>k} |U_{ej}|^2 |U_{ek}|^2 \sin \left( \frac{\Delta m_{jk}^2 L}{4E} \right) \\
&= \sin^2(2\theta_{13}) \sin^2 \left( \frac{\Delta m_{31}^2 L}{4E} \right) \\
&\quad + \cos^4 \theta_{13} \sin^2(2\theta_{12}) \sin^2 \left( \frac{\Delta m_{21}^2 L}{4E} \right) \\
&\quad - \frac{1}{2} \sin^2 \theta_{12} \sin^2(2\theta_{13}) \sin \left( \frac{\Delta m_{31}^2 L}{2E} \right) \sin \left( \frac{\Delta m_{21}^2 L}{2E} \right) \\
&\quad + \sin^2 \theta_{12} \sin^2(2\theta_{13}) \cos \left( \frac{\Delta m_{31}^2 L}{2E} \right) \sin^2 \left( \frac{\Delta m_{21}^2 L}{4E} \right).
\end{aligned} \tag{2.11}$$

One can see that the oscillations are governed by two quadratic mass splittings,  $\Delta m_{21}^2$  and  $\Delta m_{31}^2$ . Equation 2.11 is plotted as a function of  $L/E$  in Fig. 2.6 with the current best values of  $\Delta m^2$ s and  $\sin^2(2\theta_{12})$ , and  $\sin^2(2\theta_{13})$  at the upper bound [8].

The KamLAND experiment has observed a 40% disappearance of  $\nu_e$  at the baseline of 180 km [3]. The detected deficit is presumably associated with the second term of Eq. 2.11. Since the uncertainties in  $\Delta m^2$ s are large, it is clear that the measuring the first dip in the survival probability is the key to the analysis.

Figure 2.7 shows the disappearance probability ( $= 1 - P(\bar{\nu}_e \rightarrow \bar{\nu}_e)$ ) of observable neutrinos as a function of distance from a reactor neutrino source. Here the term observable neutrinos refers to neutrinos undergoing inverse beta decay interaction, had there been no oscillation. The probability is integrated over energy from 1.806 MeV to 10 MeV. The probability term  $P_1$  and  $P_2$  are the first and the rest terms on the right side of Eq. 2.11, respectively. The first

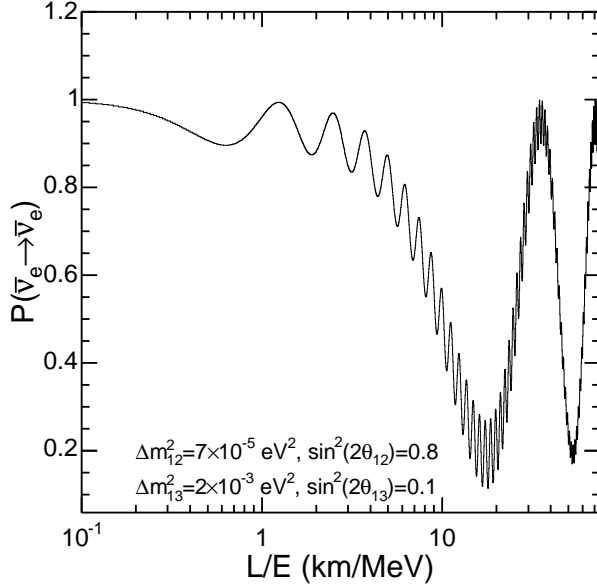


Figure 2.6: The survival probability of  $\bar{\nu}_e$  vs the ratio of the distance to the neutrino energy ( $L/E$ ) with  $\sin^2(2\theta_{13})$  set at the maximum value allowed in the current limit [8].

maximum in the disappearance probability occurs  $\sim 2$  km almost solely due to  $P_1$ , which is independent of  $\theta_{12}$  or  $\Delta m_{21}^2$ . The second peak is dominantly due to  $P_2$ , especially the second term in Eq. 2.11. The contributions from the third and fourth terms on the right side of Eq. 2.11 are inherently small compared to the first two terms due to the cross terms in  $\Delta m_{21}^2$  and  $\Delta m_{31}^2$  for the currently known values.

Since the first and the second terms in Eq. 2.12 can be combined due to  $\Delta m_{31}^2 \simeq \Delta m_{32}^2$ , the survival probability can be approximated as

$$P(\bar{\nu}_e \rightarrow \bar{\nu}_e) \simeq 1 - \sin^2(2\theta_{13}) \sin^2\left(\frac{\Delta m_{31}^2 L}{4E}\right) - \cos^4 \theta_{13} \sin^2(2\theta_{12}) \sin^2\left(\frac{\Delta m_{21}^2 L}{4E}\right). \quad (2.12)$$

## 2.5 Determination of $\theta_{13}$

### 2.5.1 Measurement of Reactor Neutrino Flux

The reactor  $\bar{\nu}_e$  flux is measured by a detector placed at a short distance from the reactor before the oscillation occurs. The RENO target consists of 0.1% Gd loaded liquid scintillator,  $18.7 \text{ m}^3$  in volume and 16.1 tons in mass. The liquid scintillator is made of Linear Alkybenzene (LAB) with a small amount of fluors and the Gd compound. This corresponds to  $1.21 \times 10^{30}$  free protons available for the inverse beta decay reaction.

The reactor  $\bar{\nu}_e$ 's are detected by the inverse beta decay  $\bar{\nu}_e + p \rightarrow n + e^+$  reaction. The ionization energy loss and subsequent annihilation of the positron from the inverse beta decay reaction result in a prompt signal. After an average of  $30 \mu\text{s}$ , a delayed signal will follow due to the neutron capture by Gd and subsequently emitting several gammas with a total energy of about 8 MeV. Exploiting the delayed coincidence is a key to controlling backgrounds.

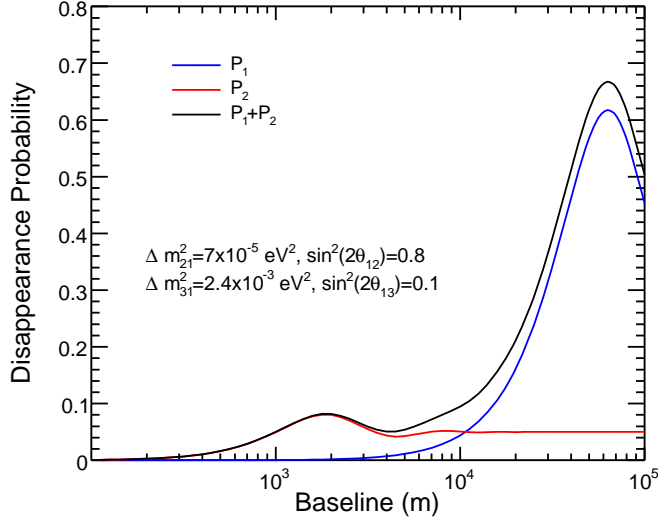


Figure 2.7: Reactor neutrino disappearance probability integrated over neutrino energy from 1.806 MeV to 10 MeV as a function of distance from the source.  $P_1$  and  $P_2$  are defined in the text.

The detector should be located underground in order to reduce background from cosmic rays and cosmic ray induced spallation products, such as neutrons and the radioactive isotope  $^9Li$ . One also needs to remove backgrounds due to gamma rays from natural radioactivity in the detector material and the surrounding rocks.

### 2.5.2 Effects on Reactor Neutrino Flux Due to $\theta_{13}$

RENO will measure the survival probability for at a baseline of about 1.4 km with neutrino energy ranging from 1.8 MeV to about 10 MeV. The disappearance probability  $P_{dis}$  of reactor antineutrinos is obtained from the survival probability  $P_{sur}$  of Eq. 2.12

$$P_{dis} = 1 - P_{sur} = \sin^2(2\theta_{13}) \sin^2\left(\frac{\Delta m_{31}^2 L}{4E}\right) + \cos^4 \theta_{13} \sin^2(2\theta_{12}) \sin^2\left(\frac{\Delta m_{21}^2 L}{4E}\right). \quad (2.13)$$

The disappearance probability can be expressed as sum of a  $\theta_{13}$ -dominant term  $P_{13}$  and a  $\theta_{12}$ -dominant term  $P_{12}$ ,

$$P_{dis} = P_{13} + P_{12} \quad (2.14)$$

where  $P_{13} = \sin^2(2\theta_{13}) \sin^2\left(\frac{\Delta m_{31}^2 L}{4E}\right)$  and  $P_{12} = \cos^4 \theta_{13} \sin^2(2\theta_{12}) \sin^2\left(\frac{\Delta m_{21}^2 L}{4E}\right)$ . Here,  $P_{13}$  is  $P_1$  and  $P_{12}$  is an approximation of  $P_2$  in Sect. 2.4.3.

The value of  $\theta_{13}$  will be obtained from  $P_{13}$  as a result of subtracting  $P_{12}$  from the experimental measurement of  $\bar{\nu}_e$  disappearance probability of  $P_{dis}$ . In Fig. 2.7, the disappearance probabilities of  $P_{13}$ ,  $P_{12}$ , and  $P_{dis}$  are shown as a function of the antineutrino flight distance from 100 m to 250 km. We chose  $\sin^2(2\theta_{13}) = 0.01$  for a convenient discussion. The rest of parameters are taken as follows

$$\Delta m_{21}^2 = 7.9 \times 10^{-5} \text{ eV}^2, \quad \Delta m_{31}^2 = 2.5 \times 10^{-3} \text{ eV}^2. \quad (2.15)$$

Figure 2.7 shows that the  $P_{12}$  contribution is negligible and thus the disappearance probability ( $P_{dis}$ ) is almost equal to  $P_{13}$ , within a few kilometers of the baseline. Since  $P_{13}$  is

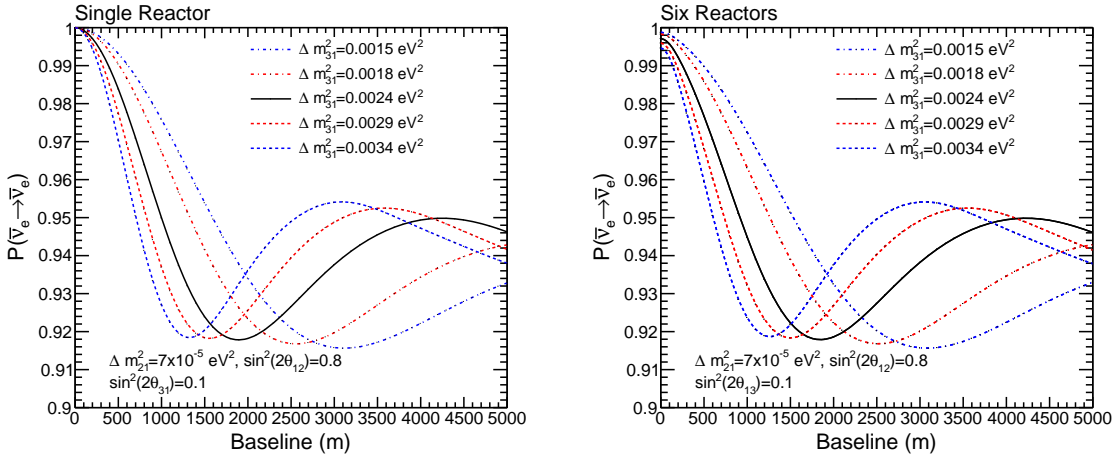


Figure 2.8: Survival probabilities of the reactor neutrinos with  $\sin^2(2\theta_{13}) = 0.1$  and various values of  $\Delta m_{31}^2$  as a function of the distance from a single reactor (left) and six reactors arranged as shown in Fig. 1.2 (right).  $\Delta m_{31}^2 = 0.0024 \text{ eV}^2$  represents the most probable value and the ranges  $0.0018 \sim 0.0029 \text{ eV}^2$  and  $0.0015 \sim 0.0034 \text{ eV}^2$  represent 63% and 90% CL, respectively. There is little difference between these two cases except at very small distances.

proportional to  $\theta_{13}$  exclusively, the disappearance measurement of reactor antineutrinos will directly probe the mixing angle of  $\theta_{13}$ . The first oscillation maximum of  $P_{13}^{max}(= \sin^2(2\theta_{13}))$  occurs near the baseline of  $\sim 2$  km. The best measurement of  $\theta_{13}$  could be possible at the first oscillation maximum. Beyond the first oscillation minimum the  $P_{12}$  contribution grows rapidly, and  $P_{13}$  and  $P_{dis}$  deviate from each other. As the baseline goes longer than 50 km, the  $P_{12}$  contribution becomes dominant in  $P_{dis}$ .

The maximum location differs within the measured error of  $\Delta m_{32}^2$ . Figure 2.8 shows  $P_{13}$  integrated over neutrino energy from 1.8 to 8 MeV, as a function of the baseline  $L$  for three values of  $\Delta m_{32}^2$  in its 95% C.L. allowed range. The curves show that  $P_{13}$  is sensitive to  $\Delta m_{32}^2$ , and its oscillation maxima occur at baselines of 1.5 to 2.5 km.

Since the measurement of disappearance probability includes the  $P_{12}$  contribution, determination of  $\theta_{13}$  from  $P_{13}(= P_{dis} - P_{12})$  will suffer from the uncertainties of  $\theta_{12}$  and  $\Delta m_{21}^2$ . At the first maximum the fraction of  $P_{12}$  relative to  $P_{13}$  is about 2.6% to 25% when  $\sin^2(2\theta_{13})$  varies from 0.01 to 0.10. The uncertainty in determining  $\sin^2(2\theta_{13})$  due to the uncertainty of  $P_{12}$  is less than 0.005. For  $\sin^2(2\theta_{13}) > 0.001$ , the  $P_{12}$  contribution to  $P_{dis}$  can be ignored. Therefore, the survival probability of reactor antineutrinos can be written without  $\theta_{12}$  and  $\Delta m_{21}^2$  and if the detector is located near the first oscillation maximum in

$$\begin{aligned} P_{sur} &= 1 - \sin^2(2\theta_{13}) \sin^2 \left( \frac{\Delta m_{31}^2 L}{4E} \right) \\ &= 1 - \sin^2(2\theta_{13}) \sin^2 \left( 1.27 \frac{\Delta m_{31}^2 [10^{-3} \text{ eV}^2] L [\text{km}]}{E_{\bar{\nu}_e} [\text{MeV}]} \right). \end{aligned} \quad (2.16)$$

### 2.5.3 Experimental Extraction of $\theta_{13}$

#### Single Detector Measurement

The current best limit on  $\theta_{13}$  comes from null results of neutrino oscillations by CHOOZ and Palo Verde [8, 9]. These experiments were at a baseline distance of about 1 km and thus were

Systematic Sources	Relative Uncertainties (%)
Reaction Cross Section	1.9
Number of Protons	0.8
Detection Efficiency	1.5
Reactor Power	0.7
Energy Released per Fission	0.6
Combined	2.7

Table 2.3: Systematic uncertainties in the absolute antineutrino normalization of CHOOZ.

Selection Criteria	$\epsilon$ (%)	Relative Uncertainties (%)
Positron Energy	97.8	0.8
Positron Geode Distance	99.9	0.1
Neutron Capture	84.6	1.0
Capture Energy Containment	94.6	0.4
Neutron Geode Distance	99.5	0.1
Neutron Delay	93.7	0.4
Positron-neutron Distance	98.4	0.3
Neutron Multiplicity	97.4	0.5
Combined	69.8	1.5

Table 2.4: Antineutrino detection efficiency of CHOOZ.

more sensitive to the second term of Eq. 2.12. Both experiments looked for a deficit in the  $\bar{\nu}_e$  flux at the location of the detector by comparing the observed rate with the expected rate from the reactors based on no oscillation. Those experiments with only one detector at a fixed baseline could not have greatly improved sensitivity to  $\theta_{13}$  because of uncertainties related to knowledge of neutrino flux from the reactors and to the detector acceptance. A single detector measurement had to calculate the expected rate relying on the reactor operation data such as the generated thermal power as a function of time and the nuclear fuel composition.

CHOOZ and Palo Verde detected the reactor  $\bar{\nu}_e$  events by the inverse beta decay reaction utilizing the 0.1% Gd loaded liquid scintillator. The value of  $\sin^2(2\theta_{13})$  was determined by comparing the observed antineutrino rate and energy spectrum with expected ones based on no oscillation. If the observed event rate is smaller than the expected one, the number of detected antineutrinos ( $N_{\bar{\nu}_e}$ ) finds the value of  $\sin^2(2\theta_{13})$  by the following equation

$$N_{\bar{\nu}_e} = \frac{N_p}{4\pi L^2} \int \int \epsilon_{det} P(\bar{\nu}_e \rightarrow \bar{\nu}_e) \frac{d\sigma}{dE_{e+}} \frac{d\phi_{\bar{\nu}_e}}{dE_{\bar{\nu}}} dE_{e+} dE_{\bar{\nu}}, \quad (2.17)$$

where  $N_p$  is the number of free protons in the detector target,  $L$  is the distance of the detector from the reactor,  $\epsilon_{det}$  is the efficiency of detecting an antineutrino,  $P(\bar{\nu}_e \rightarrow \bar{\nu}_e)$  is the survival probability from oscillation as a function of  $\sin^2(2\theta_{13})$ ,  $\frac{d\sigma}{dE_{e+}}$  is the differential cross sections of the inverse beta decay reaction, and  $\frac{d\phi_{\bar{\nu}_e}}{dE_{\bar{\nu}}}$  is the differential energy distribution at the reactor.

For CHOOZ, the background rate was  $1.41 \pm 0.24$  events per day in the 1997 run, and  $2.22 \pm 0.14$  events per day after its trigger was modified in 1998. The background events were subtracted from the observed event rated before extracting the value of  $\sin^2(2\theta_{13})$ . The systematic uncertainties and efficiencies of CHOOZ are summarized in Tables 2.3 and 2.4, respectively.

Neither CHOOZ nor Palo Verde observed any deficit in the observed antineutrino rate.

The negative result gave rise to set a limit on the neutrino mixing angle as shown in Fig. 2.1. CHOOZ obtained the best limit of 0.17 for  $\sin^2(2\theta_{13})$  for at the 90% C.L.

## Multi Detector Measurement

Since the effective disappearance will be extremely small, new experiment for  $\theta_{13}$  would need to improve the previous systematic limitations. This could be achieved by two or more identical detectors.

Mikaelyan and Sinev pointed out that the systematic uncertainties can be greatly suppressed or totally eliminated when two detectors positioned at two different baselines are utilized [26]. The near detector close to the reactor is used to measure the flux and energy spectrum of the antineutrinos before oscillation effects take place, and thus relaxes the requirement of knowing the details of the fission process and operational conditions of the reactor. The value of  $\sin^2(2\theta_{13})$  can be measured by comparing the flux and energy distribution of antineutrinos observed with the far detector to those of the near detector after considering a reduction factor due to distance squared.

With multiple detector setup, one will obtain the ratio in the number of observed antineutrinos with energy between  $E$  and  $E + dE$ , at a far distance  $L_{far}$  to that at a near distance  $L_{near}$  as follows:

$$\frac{N_{far}^\nu}{N_{near}^\nu} = \left( \frac{L_{near}}{L_{far}} \right)^2 \left( \frac{N_{far}^p}{N_{near}^p} \right) \left( \frac{\epsilon_{far}}{\epsilon_{near}} \right) \left[ \frac{P(\bar{\nu}_e \rightarrow \bar{\nu}_e; E, L_{far})}{P(\bar{\nu}_e \rightarrow \bar{\nu}_e; E, L_{near})} \right], \quad (2.18)$$

where  $N_{near(far)}^p$  and  $\epsilon_{near(far)}$  are the number of target protons and the detection efficiency at near (far) detector. If the two detectors are identical and thus have the same efficiency and the same number of target protons, the ratio is given only by the ratio of detector distances and the ratio of survival probabilities. Suppose the near detector is located fairly close to a single reactor core, the value of  $\sin^2(2\theta_{13})$  is approximately given by

$$\sin^2(\theta_{13}) \simeq \frac{1}{\sin^2 \left[ 1.267 \Delta m_{31}^2 (\text{eV}^2) \times 10^3 \frac{L_{far}(\text{km})}{E(\text{MeV})} \right]} \left[ 1 - \left( \frac{N_{far}^\nu}{N_{near}^\nu} \right) \left( \frac{L_{near}}{L_{far}} \right) \right], \quad (2.19)$$

where  $L_{far}$  and  $E$  are given in the units of km and MeV, respectively. From this simplified discussion, it is clear that the two detector scheme is an excellent approach in the further sensitive measurement of  $\sin^2(2\theta_{13})$ .

The projected statistical uncertainty of RENO is 0.3% with three year data-taking. The goal of RENO is to reduce the total systematic uncertainty to less than 0.6%. Due to the multiple ( $> 2$ ) reactor with a single near detector configuration, the reactor related systematic uncertainties are expected to cancel out because of two identical detectors and isotropic reactor neutrino fluxes, and will be less than 0.1%. The RENO detector design differs slightly from CHOOZ in a sense that a non-scintillating buffer region shields the active region (target and  $\gamma$  catcher) from the intrinsic PMT radioactivity. This allows us to remove a few selection cuts and expected systematic uncertainty will be  $\sim 0.3\%$ . The systematic uncertainty of H/C ratio and the target mass will be significantly reduced to  $\sim 0.2\%$  due to the two identical detectors and accurate measurement of detector volumes. In overall, based on an order of magnitude smaller than CHOOZ in both statistical and systematic uncertainties as shown in Table 2.5, RENO is expected to measure the value of  $\sin^2(2\theta_{13})$  above 0.02.

Uncertainty Source		CHOOZ	RENO (Goal)
Reactor Related	Neutrino Flux and Cross Section	1.9	<0.1
	Reactor Power	0.7	0.4
	Energy Released per Fission	0.6	<0.1
Detector Related	H/C Ratio	0.8	0.2
	Target Mass	0.3	0.2
	H/Gd Ratio	1.0	<0.4
	Positron Energy	0.8	0.1
	Positron Geode Distance	0.1	–
	Capture Energy Containment	0.4	0.2
	Neutron Geode Distance	0.1	–
	Neutron Delay	0.4	<0.1
	Positron–Neutron Distance	0.3	–
Neutron Multiplicity		0.5	–
Combined		2.7	<0.6

Table 2.5: Systematic uncertainties of CHOOZ [8] and RENO.

## 2.6 Additional Physics

The main goal of the RENO experiment is to measure the value of neutrino mixing angle. It is worthwhile to explore other physics that can be done with this experiment.

### 2.6.1 Supernova Neutrinos

Liquid scintillator detectors will be sensitive to a burst of neutrinos of all flavors from a Galactic supernova in the energy of a few to tens of MeV range. The time scale of the burst is tens of seconds. The RENO detector background in a 10 second period is enough low for a successful observation of the supernova signal. Identical near and far RENO detectors have roughly 100 tons of liquid scintillators in total, sensitive to the supernova neutrinos. The RENO detector contains  $6.0 \times 10^{30}$  free protons,  $4.5 \times 10^{31}$  carbons, and  $3.3 \times 10^{31}$  electrons, and thus would observe 35 events from a supernova at 10 kpc [27, 28]. Twenty-six events are expected via the inverse beta decay,  $\bar{\nu}_e + p \rightarrow e^+ + n$ . Neutral current interactions of  $\nu(\bar{\nu}) + ^{12}\text{C} \rightarrow \nu(\bar{\nu}) + ^{12}\text{C}^*$  would produce 7.5 events with a 15.5 MeV de-excitation  $\gamma$ -ray from  $^{12}\text{C}^*$  [29]. Charged current interactions of  $\bar{\nu}_e + ^{12}\text{C} \rightarrow ^{12}\text{B} + e^+$  and  $\nu_e + ^{12}\text{C} \rightarrow ^{12}\text{N} + e^-$  would produce 1.5 events. Elastic neutrino-electron scattering  $\nu + e^- \rightarrow \nu + e^-$  would produce 1.6 events. The observation will probably require an accurate clock and an effective trigger of minimal dead time.

### 2.6.2 Sterile Neutrinos

The discovery of sterile neutrinos would have a revolutionary impact on neutrino and particle physics. The idea of sterile neutrinos was initially introduced by Pontecorvo in 1967 [30] and has been considered later by many physicists [31, 32, 33, 34, 35]. Further information and references on sterile neutrinos can be found in the paper by Berezinsky, Narayan, and Vissani [36].

While recent neutrino oscillation results are understood in the framework of 3 active neutrino mixing, they do not completely exclude admixture of sterile neutrinos. An experimental hint in favor of sterile neutrinos comes from the unconfirmed observation by the LSND collab-

oration on  $\nu_\mu \rightarrow \nu_s$  [37]. The mixing with sterile neutrinos based on the LSND signal predicts disappearance of reactor neutrinos with  $\Delta m^2 \sim \text{eV}^2$  very close to the current upper bound from the Burgey experiment [38].

In case of only one sterile neutrino one obtains for the survival probability at nuclear reactors

$$P_{\bar{\nu}_e \rightarrow \bar{\nu}_e} = 1 - \sin^2(2\theta_{13}) \sin^2\left(\frac{\Delta m_{atm}^2 L}{4E}\right) - \sin^2(2\theta_s) \sin^2\left(\frac{\Delta m_s^2 L}{4E}\right), \quad (2.20)$$

where  $\theta_s$  and  $\Delta m_s^2 = m_4^2 - m_1^2$  are the mixing parameters of the sterile neutrinos. It is evident from this equation that a sterile neutrino would have modification in the measured neutrino flux of the RENO experiment if the associated mixing parameter  $\sin^2(2\theta_s)$  is not too small and the mass difference is the relevant range.

If  $\Delta m_s^2 \sim \Delta m_{atm}^2$  and the total rate measurement only is available, it will be rather difficult at the RENO experiment to disentangle  $\bar{\nu}_e \rightarrow \bar{\nu}_{\mu/\tau}$  oscillations due to  $\theta_{13}$  from oscillations due to  $\theta_s$ . The RENO experiment might be able to separate the two oscillation effects if  $\Delta m_s^2$  differs sufficiently from  $\Delta m_{atm}^2$  and/or enough spectral information is available.

If  $\Delta m_s^2 \gg \Delta m_{atm}^2$  and the oscillations due to  $\theta_s$  are already averaged out at the near detector, no information on the sterile neutrino mixing can be obtained from the comparison of the far and near detectors, and the transformation into the sterile neutrinos will not affect the  $\theta_{13}$  measurement. In this case, the information on the sterile neutrino mixing can be obtained from the near detector if relatively precise measurement of the initial reactor neutrino flux is available, or if a very-near detector at  $\sim 10$  m could be installed.

### 2.6.3 Mass Varying Neutrinos

The idea of mass varying neutrinos came from a scalar field of acceleron associated with the dark energy of the universe [39, 40, 41, 42]. Possible couplings of acceleron to matter fields could introduce a very different feature of neutrino oscillation parameters [43]. A possible effect due to the mass varying neutrinos may be possibly tested in the RENO experiment because of different path lengths in air and matter. A different parametrization of  $\theta_{13}$  and  $\Delta m_{31}^2$  for air and matter introduces arbitrary oscillation effects different in air and matter [44]. Combination of reactor and accelerator neutrino experiments with different path lengths in air and matter will give meaningful information on the mass-varying neutrinos.

### 2.6.4 Geo-neutrinos

Geo-neutrinos, the antineutrinos from the progenies of U, Th and K decays in the Earth, provide the surface information on the content of radioactive elements in the whole planet. Their detection can shed light on the sources of the terrestrial heat flow, on the present composition, and on the origins of the Earth. A recent review on geo-neutrinos is found in Ref. [45]. The first measurement of geo-neutrinos was made by the KamLAND detector in 2005 (see Fig. 2.9) [46]. KamLAND and Borexino detectors are collecting geo-neutrino data, while several planned experiments (*e.g.* SNO+, LENA, HANOHANO, and EARTH) have geo-neutrino measurements among their primary goals.

All experiments, either running or in preparation, use the inverse beta decay on free protons as the reaction for geo-neutrino detection. The measured shape of neutrino spectrum will be essential for determining observation of geo-neutrinos and their radioactive progenitors. The RENO detector is not large enough for the sensitive geo-neutrino measurement, but may observe some number of geo-neutrinos.

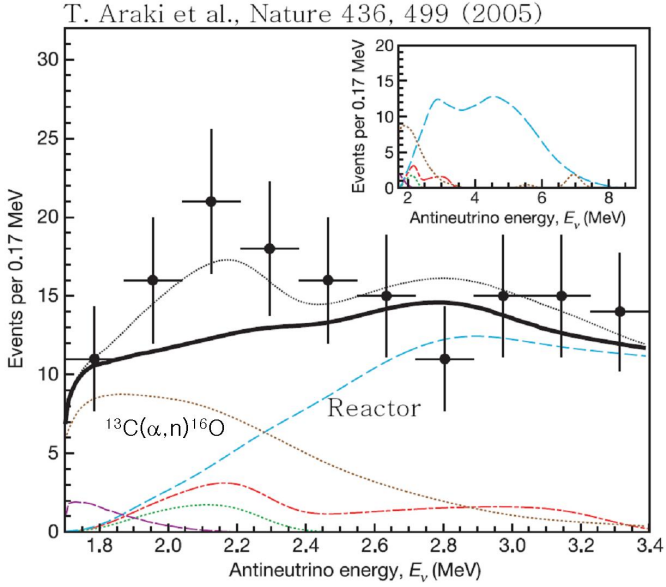


Figure 2.9: KamLAND observed 152 events in the geo-neutrino energy range from the 749 live days of data. The extracted signal events of geo-neutrinos are  $25^{+19}_{-18}$  while backgrounds are 127 events (82 reactor antineutrinos (dashed light blue line), 42 fake events from  $^{13}\text{C}(\alpha, n)^{16}\text{O}$  (dotted brown line), and 3 random coincidences (dashed purple line)). Figure is taken from Ref. [46].

### 2.6.5 Precise Measurement of $\theta_{12}$

After completing  $\theta_{13}$  measurement effort, the RENO experimental scope could be extended to the precise measurement of  $\theta_{12}$  by adding one more detector of a few hundred tons for the target mass at a distance  $50 \sim 70$  km from the reactor center. The near and far detectors of RENO could be used as near detectors, and thus would reduce relevant systematic uncertainties significantly for the new precise measurement of  $\theta_{13}$ . For baselines longer than 50 km, the reactor antineutrino oscillations due to  $\Delta m_{31}^2$  average out and the survival probability becomes

$$P = \cos^4 \theta_{13} \left[ 1 - \sin^2(2\theta_{12}) \sin \left( \frac{\Delta m_{21}^2 L}{4E} \right) \right]. \quad (2.21)$$

The oscillations due to  $\theta_{12}$  and  $\Delta m_{21}^2$  were observed in the KamLAND experiment.

The optimal baseline for measuring  $\theta_{12}$  is about 70 km because the antineutrino survival probability becomes minimal for  $\sin^2 \left( \frac{\Delta m_{21}^2 L}{4E} \right) \approx 1$ , *i.e.*  $P \approx 1 - \sin^2(2\theta_{12})$  very sensitive to the value of  $\theta_{12}$  [47]. The extension version of RENO detector is expected to improve the error of the  $\theta_{12}$  value.

On the other hand, an intermediate baseline detector with  $L \sim 20 - 30$  km from the reactor will see the maximum of survival probability for  $\sin^2 \left( \frac{\Delta m_{21}^2 L}{4E} \right)$  and becomes highly sensitive to the value of  $\Delta m_{21}^2 \ll 1$  [48, 49].

### 2.6.6 Reactor Physics

The RENO near detector will detect an order of one-million neutrino events per year, and measure the flux and energy distribution of the reactor neutrinos with a greater accuracy than

ever. This information would lead to meaningful comparison of thermal power and reactor fuel loading between measurements and calculations. Such a successful comparison will allow us to do a real-time and direct measurement of reactor thermal power with a neutrino detector. In addition, a precise determination of the reactor neutrino spectrum might be useful for reducing the flux uncertainty. There might be an interesting spin-off of such a precise measurement of reactor neutrino spectrum and flux, to reactor design and operation although it is not quite sure at the moment. Another application could be the direct check of nuclear non-proliferation treaties.

### 2.6.7 Study of the Directionality

The near detector of RENO will detect enough statistics of antineutrino events, and will allow us to do a detailed exploration of the directionality effect of incident reactor neutrinos. The incident neutrino direction could be determined from the forward scattering of the outgoing neutron in the inverse beta decay reaction. Successive multiple scatterings of the neutron introduce a broad distribution of their capture location. Therefore, the incoming neutrino direction cannot be determined on an event by event basis. However, the neutron would have a slightly larger probability to be captured in forward direction. This directional correlation between the reactor neutrino direction and neutron captured direction may be measured with sufficient high statistics and resolution. This directional effect was first seen in the Burgey experiment [50] and even better in the CHOOZ experiment [8].

The near detector will record data when some of six reactor cores are off, or all on. Comparison of these different data sets, in combination with a modeling of the expected event distributions, will allow us to understand and test the directionality much better. The directionality information could be used for astrophysics, reactor physics, or geo-neutrino detection.

# Bibliography

- [1] Y. Ashie *et al.*, Phys. Rev. D **71**, 112005 (2005).
- [2] Q. R. Ahmad *et al.*, Phys. Rev. Lett. **89**, 011301 (2002).
- [3] K. Eguchi *et al.* (KamLAND Collaboration), Phys. Rev. Lett. **90**, 021802 (2003).
- [4] R. N. Mohapatra *et al.*, “Theory of Neutrinos:A white paper” (2005), hep-ph/0510213.
- [5] B. T. Cleveland *et al.*, Astrophys. J. **496**, 505 (1998); Y. Fukuda *et al.* (Kamiokande Collaboration), Phys. Rev. Lett. **77**, 1683 (1996); J. N. Abdurashitov *et al.* (SAGE Collaboration), J. Exp. Theor. Phys. **95**, 181 (2002); W. Hampel *et al.* (GALLEX Collaboration), Phys. Lett. B **447**, 127 (1999); M. Altmann *et al.* (GNO Collaboration), Phys. Lett. B **490**, 16 (2000); M. Altmann *et al.* (GNO Collaboration), Phys. Lett. B **616**, 174 (2005); M. B. Smy *et al.* (Super-Kamiokande Collaboration), Phys. Rev. D **69**, 011104 (2004); Q. R. Ahmad *et al.* (SNO Collaboration), Phys. Rev. Lett. **87**, 071301 (2001); Q. R. Ahmad *et al.* (SNO Collaboration), Phys. Rev. Lett. **89**, 011301 (2002); Q. R. Ahmad *et al.* (SNO Collaboration), Phys. Rev. Lett. **89**, 011302 (2002); S. N. Ahmed *et al.* (SNO Collaboration), Phys. Rev. Lett. **92**, 181301 (2004); B. Aharmim *et al.* (SNO Collaboration), Phys. Rev. C **72**, 055502 (2005).
- [6] Y. Fukuda *et al.* (Super-Kamiokande Collaboration), Phys. Rev. Lett. **81**, 1158 (1998); S. Fukuda *et al.* (Super-Kamiokande Collaboration), Phys. Rev. Lett. **85**, 3999 (2000); Y. Ashie *et al.* (Super-Kamiokande Collaboration), Phys. Rev. Lett. **93**, 101801 (2004); Y. Ashie *et al.* (Super-Kamiokande Collaboration), Phys. Rev. D **71**, 112005 (2005); M. C. Sanchez *et al.* (Soudan 2 Collaboration), Phys. Rev. D **68**, 113004 (2003); M. Ambrosio *et al.* (MACRO Collaboration), Eur. Phys. J. C **36**, 323 (2004).
- [7] K. Eguchi *et al.* (KamLAND Collaboration), Phys. Rev. Lett. **90**, 021802 (2003); T. Araki *et al.* (KamLAND Collaboration), Phys. Rev. Lett. **94**, 081801 (2005); E. Aliu *et al.* (K2K Collaboration), Phys. Rev. Lett. **94**, 081802 (2005); D. G. Michael *et al.* (MINOS collaboration), Phys. Rev. Lett. **97**, 191801 (2006).
- [8] M. Apollonio *et al.* (Chooz Collaboration), Eur. Phys. J. C **27**, 331 (2003).
- [9] F. Boehm *et al.* (Palo Verde Collaboration), Phys. Rev. D **62**, 072002 (2000).
- [10] M. Maltoni, T. Schwetz, M. Tortola, and J. Valle, New J. Phys. **6**, 122 (2004).
- [11] G. L. Fogli *et al.*, Prog. Part. Nucl. Phys. **57** (2006) 71–78.
- [12] M. Maltoni, T. Schwetz, M. A. Tortola, and J. W. F. Valle, Phys. Rev. D **68**, 113010 (2003).

- [13] K. Anderson *et al.*, “White paper report on using nuclear reactors to search for a value of  $\theta_{13}$ ” (2004), hep-ex/0402041.
- [14] Members of the APS Multi-Divisional Neutrino Study, “The Neutrino Matrix” (2004).
- [15] M. Freund, P. Huber and M. Lindner, Nucl. Phys. **B615**, 331-357 (2001).
- [16] C. L. Cowan, F. Reines, F. B. Harrison, H. W. Kruse, and A. D. McGuire, Science **124**, 103 (1956).
- [17] V. I. Kopeikin, *Preprint Kurchatov Institute of Atomic Energy*, Moscow **IAE-4305/2** (1998).
- [18] D. H. Wilkinson, Nucl. Phys. **A377**, 474 (1982).
- [19] K. Schreckenbach, G. Colvin, W. Gelletly, and F. Von Feilitzsch, Phys. Lett. B **160**, 325 (1985).
- [20] A. A. Hahn *et al.*, Phys. Lett. B **218**, 365 (1989).
- [21] H. V. Klapdor and J. Metzinger, Phys. Rev. Lett. **48**, 127 (1982).
- [22] P. Vogel, G. K. Schenter, F. M. Mann, and R. E. Schenter, Phys. Rev. C **24**, 1543 (1981).
- [23] C. Bemporad, G. Gratta, and P. Vogel, Rev. Mod. Phys. **74**, 297 (2002).
- [24] H. Minakata and S. Watanabe, Phys. Lett. B **468**, 256 (1999).
- [25] H. Minakata *et al.*, Phys. Rev. D **68**, 033017 (2003); *ibid.* D **70**, 059901 (E) (2004).
- [26] L. A. Mikaelyan and V. V. Sinev, Phys. Atomic Nucl. **63**, 1002 (2000).
- [27] K. Scholberg, “Supernova neutrino detection” (2007), arXiv:astro-ph/070108v1.
- [28] L. Cadonati, F. P. Calaprice, and M. C. Chen, “Supernova Neutino Detection in Borexino,” Astropart. Phys. **16**, 361-372 (2002).
- [29] E. Kolbe, K. Langanke, and P. Vogel, Phys. Rev. D **66**, 013007 (2002).
- [30] B. Pontecorvo, J. Exp. Theor. Phys. **53**, 1717 (1967) [Sov. Phys. JETP **26**, 984 (1968)].
- [31] D. Caldwell and R. Mohapatra, Phys. Rev. D **46**, 3259 (1993).
- [32] J. T. Peltoniemi, D. Tommasini, and J. W. F. Valle, Phys. Lett. B **298**, 383 (1993); J. T. Peltoniemi and J. W. F. Valle, Nucl. Phys. B **406**, 409 (1993).
- [33] S. Bilenky, C. Giunti, and W. Grimus, Eur. Phys. J. **C1**, 247 (1998).
- [34] K. Benakli and A. Smirnov, Phys. Rev. Lett. **79**, 4314 (1997).
- [35] B. Kayser, (1998) hep-ph/9810513.
- [36] V. Berezinsky, M. Narayan, F. Vissani, Nucl. Phys. B **658**, 254 (2003).
- [37] C. Athanassopoulos *et al.* (LSND Collaboration), Phys. Rev. Lett. **77**, 3082 (1996); Phys. Rev. Lett. **81**, 1774 (1998); Phys. Rev. D **64**, 112007 (2001).
- [38] M. Maltoni, T. Schwetz, M. A. Tortola, and J. W. F. Valle, Nucl. Phys. B **643**, 321 (2002).

- [39] P. Q. Hung, “Sterile neutrinos and accelerating Universe” (2000) hep-ph/0010126.
- [40] Peihong Gu, Xiulian Wang, and Xinmin Zhang, “Dark energy and neutrino mass limits from baryogenesis,” Phys. Rev. D **68**, 087301 (2003).
- [41] Rob Fardon, Ann E. Nelson, and Neal Weiner, “Dark energy from mass varying neutrinos,” JCAP 0410, 005 (2004).
- [42] R. D. Peccei, “Neutrino models of dark energy,” Phys. Rev. D **71**, 023527 (2005).
- [43] David B. Kaplan, Ann E. Nelson, and Neal Weiner, “Neutrino oscillations as a probe of dark energy,” Phys. Rev. Lett. **93**, 091801 (2004).
- [44] Thomas Schwetz and Walter Winter, “Testing mass-varying neutrinos with reactor experiments,” Phys. Lett. B **633**, 557-562 (2006).
- [45] G. Fiorentini, M. Kissia, and F. Mantovani, “Geo-neutrinos and earth’s interior,” Phys. Rep. 453/5-6, 117-172 (2007).
- [46] T. Araki *et al.*, Nature **436**, 499 (2005).
- [47] A. Bandyopadhyay, S. Choubey, and S. Goswami, Phys. Rev. D **67**, 113011 (2003).
- [48] S. T. Petcov and M. Piai, Phys. Lett. B **533**, 94 (2002).
- [49] S. Choubey, S. T. Petcov, and M. Piai, “Precision neutrino oscillation physics with an intermediate baseline reactor neutrino experiment,” Phys. Rev. D **68**, 113006 (2003).
- [50] Y. Declais *et al.*, Nucl. Phys. B 434, 503-534 (1995).

# Chapter 3

## Detector

### 3.1 Overview

The RENO experiment uses two identical detectors, one located at  $\sim 300$  m from the reactor array baseline and another at  $\sim 1400$  m. They are called near detector and far detector, respectively. By using identical design for both detectors, a number of systematic uncertainties cancel out due to normalization of the neutrino flux at the far detector using that of the near detector.

The detectors have a layered structure similar to other reactor neutrino experiments, *i.e.* Daya Bay and Double Chooz experiments. The RENO detectors consist of four cylindrical shape layers. They are, from the center, target,  $\gamma$ -catcher, buffer, and veto, where an outer layer almost enclosing an inner layer. The PMTs for detecting neutrino interaction will be in the buffer layer. The cutaway view of a RENO detector is shown in Fig. 3.1.

The “target” is Gadolinium (Gd) doped liquid scintillator contained in a transparent cylindrical vessel made of acrylic plastic. An inverse beta decay event produces a positron and neutron pair. The positron loses energy through scintillating process before being converted into two gammas via a pair annihilation. The neutron thermalizes, and then is captured by Gd nucleus producing several gammas. The gammas produced close to the boundary of target can escape target without completely depositing its energy in scintillator. To contain the energy carried by gammas escaping from the target, the “ $\gamma$ -catcher,” another liquid scintillator layer, surrounds target. Unlike the target, the liquid scintillator in the  $\gamma$ -catcher is not loaded with Gd since this layer is intended to augment the target in energy measurement of gammas emitted in target. As with target, a transparent cylindrical acrylic vessel contains  $\gamma$ -catcher liquid.

Surrounding the  $\gamma$ -catcher is a non-scintillating liquid layer called the “buffer.” Mineral oil is used as the buffer and is contained in a cylindrical vessel made of stainless steel. The photomultiplier tubes (PMTs) are mounted on the inner surface of the buffer vessel immersed in buffer. The buffer acts as a shield against gammas mainly coming from radioactive isotope contained in PMTs entering the scintillating volume.

The outermost layer of the RENO detector is the “veto,” a water Cerenkov detector layer. Its purpose is to reduce background gammas and neutrons from the surrounding environment (such as rocks) as well as cosmic muon induced background events. The veto container is constructed with 40 cm thick concrete and the top lid is made of stainless steel. PMTs are mounted on the inner surface of veto container for detecting Cerenkov light from cosmic muons.

The various design parameters have been determined for optimal performance using detailed simulation. The simulation includes background  $\gamma$ s from PMTs and surrounding rocks,

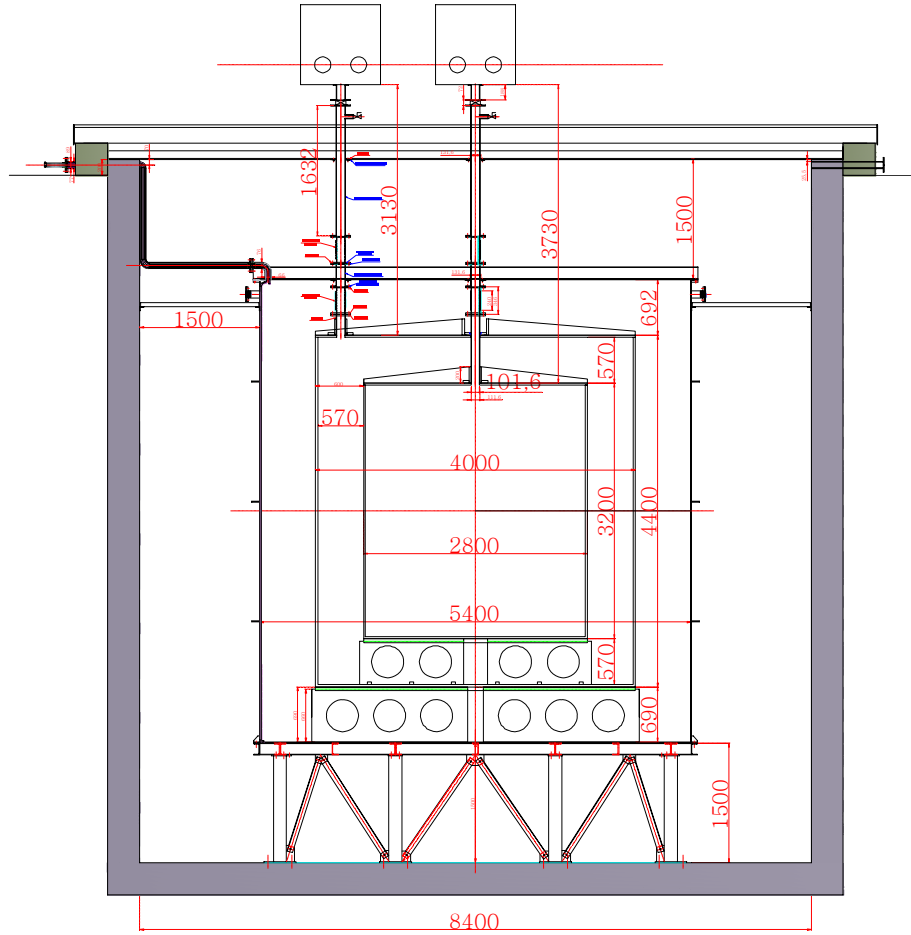


Figure 3.1: RENO detector. From the center, there are liquid scintillator filled target and gamma catcher with transparent acrylic vessel, mineral oil filled buffer with stainless steel vessel, and water filled veto layers. The PMTs for the inner and outer detectors are inwardly mounted on buffer and veto vessels, respectively.

cosmic muons reaching the detector site as well as inverse beta decay from the reactor anti-neutrinos. The detector layers and vessels are summarized in Table 3.1.

## 3.2 Target and Gamma Catcher

### 3.2.1 Structure

The two innermost layers, target and  $\gamma$ -catcher, will be contained in vessels made of acrylic plastic. This acrylic plastic is transparent to photons with wavelengths above 400 nm. Two important issues for these layers are considered; chemical compatibility between the contents and the vessel, and mechanical stability.

As for the chemical compatibility, the liquid scintillating material for both the target and  $\gamma$ -catcher should not chemically interact with the vessel for the duration of the experiment. At the same time, the  $\gamma$ -catcher vessel should be chemically inert to the mineral oil in buffer

Detector Component	Outer Diameter(mm)	Outer Height(mm)	Thickness (mm)	Material	Volume (m <sup>3</sup> )	Mass (tons)
Target	2750	3150	—	Gd-loaded LS	18.70	16.08
Target Vessel	2800	3200	25	Acrylic	0.99	1.18
γ-catcher	3940	4340	570	LS	33.19	28.55
γ-catcher Vessel	4000	4400	30	Acrylic	2.38	2.83
Buffer	5388	5788	694	Oil	76.46	64.22
Buffer Vessel	5400	5800	6/12*	SUS	1.05	8.39
Veto	8400	8890	1500	Water	354.84	354.84

Table 3.1: Dimensions of the mechanical structure of the detector. (\*)The buffer vessel thickness is 6 mm for the top and barrel sections and 12 mm for the bottom section.

layer. There have already been extensive studies on chemical compatibility of these materials for CHOOZ experiment and others. The RENO collaboration has conducted various R&D on the chemical interaction of acrylic plastic and other materials used in the experiment. The compatibility test results are in Chapter 4.

Mechanically, these vessels are required to withstand the mechanical stresses that they are subjected to during the all phases of the experiment and maintain structural integrity. When loaded with liquids, the volume of the vessels can change slightly from the nominal volume. This change should be within specified tolerances.

The target vessel an acrylic cylinder with a height of 3.2 m, a diameter of 2.8 m, and a thickness of 25 mm. The mass of the target vessel is 1.2 tons. The target vessel has an inner volume of 18.7 m<sup>3</sup> and the combined mass of the target liquid and vessel is ∼ 17 tons. Inside the γ-catcher vessel, the target vessel is mounted on the supporting structure made of the same acrylic plastic. When both target and γ-catcher are filled, the net load on the target supporting structure will be ∼ 300 kg including buoyancy. At the center of the top of the vessel, a pipe connects the target volume to the outside of the detector for filling target liquid and inserting calibration sources.

The design of the γ-catcher is similar to that of the target but about three times larger in volume. The γ-catcher vessel is an acrylic cylinder with a height of 4.4 m and a diameter of 4.0 m. Its wall is 3 cm thick. The γ-catcher vessel is mounted on the supporting structure made of acrylic plastic and placed inside the buffer vessel. It has a pipe connecting the top of the γ-catcher vessel and the outside of the detector for liquid filling and calibration source insertion. The γ-catcher vessel has a mass of ∼ 2.8 tons. The combined mass of the γ-catcher vessel and γ-catcher liquid scintillator is 31.4 tons. When the γ-catcher is immersed in buffer liquid, the total load on the γ-catcher supporting structure would be 2.2 tons.

### 3.2.2 Acrylic Vessels

The target and γ-catcher vessels are made of transparent acrylic plastic called Polymethyl-methacrylate (PMMA). The molecular formula of PMMA is (C<sub>5</sub>O<sub>2</sub>H<sub>8</sub>)<sub>n</sub>. PMMA can be found under trade names like Plexiglas, R-Cast, and Lucite. The properties of PMMA are shown in Table 3.2. With additional ingredients in PMMA the UV below 400 nm is absorbed.

The target and γ-catcher vessels are made from cast acrylic sheets (Plexiglass, GS-233) supplied by Degussa GmbH, Germany. The cast acrylic sheet has better mechanical and chemical properties than the extruded acrylic sheet. The production of the vessels is done by KOA Tech in Korea. These vessels are manufactured in several pieces for ease of manufacture and will be assembled mostly at the manufacturing site. The vessel parts will be bonded by

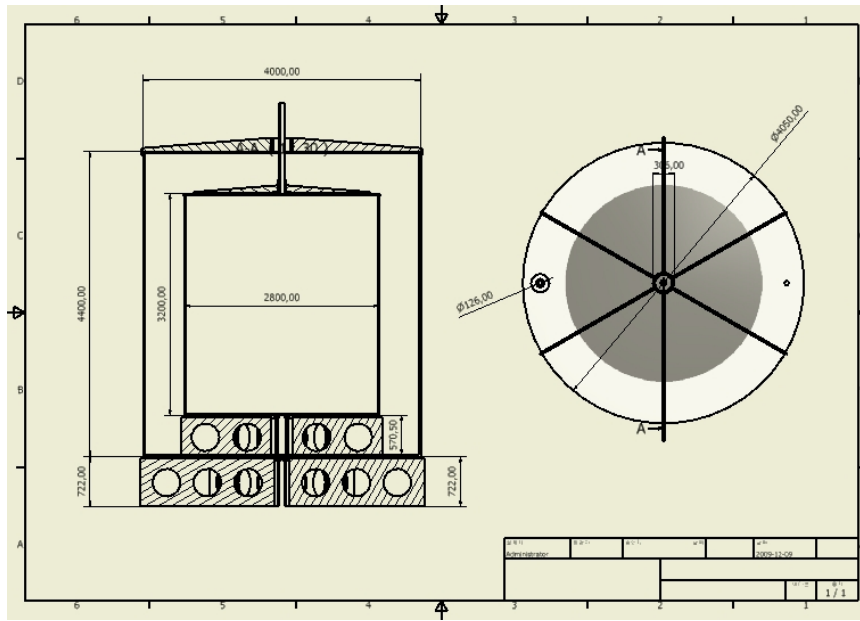


Figure 3.2: Target and gamma catcher vessels with supporting structures. The supporting structures are made with the same transparent acrylic plastic as the vessels.

Properties	Value
Density	1.19 g/cm <sup>3</sup>
Melting point	130-140 °C
Refractive index	1.491
Transmittance	92%

Table 3.2: The mechanical and optical properties of cast acrylic, such as Plexiglas GS-233 from Degussa GmbH, Germany and R-Cast from Reynolds Co., USA.

polymerization and the joined sections will be treated with annealing process.

The manufacturing precision of the vessels will be 0.1% in volume (2 mm in 1 dimension), therefore, 0.14% difference in target vessel volume between near and far detector could incur. This difference could be measured and corrected by mass flow meter and weight measurement.

### 3.2.3 Chimney

Each target and  $\gamma$ -catcher has a chimney for filling liquids and transporting calibration sources from the top lid of the veto vessel into and out of either target or  $\gamma$ -catcher. A chimney is made of about 4-inch transparent acrylic tubing with a flexible convoluted PTFE tube connecting the buffer vessel and the acrylic tubing to ease the stress. From the top lid of the buffer the chimney is made of stainless steel pipes extending to the top lid of the veto vessel.

## 3.3 Buffer

The buffer vessel is a stainless steel cylinder of 5.8 m height and 5.4 m diameter containing target,  $\gamma$ -catcher, and buffer liquid. The buffer contains non-scintillating oil to shield the scintillating volume within from background sources outside, including radioactivity in PMTs.

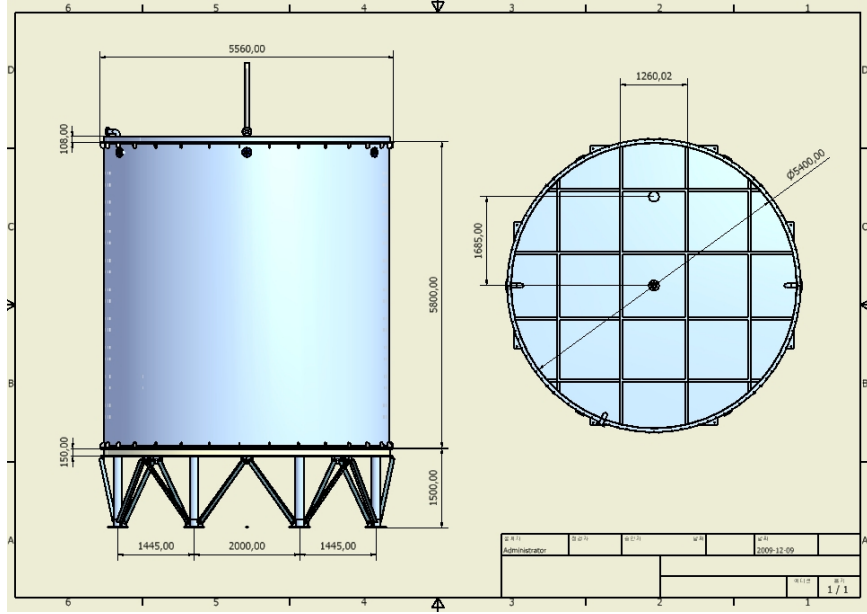


Figure 3.3: External view of the buffer vessel. The vessel is made of stainless steel (304L) and the supporting truss structure is made of nickel-plated steel pipes and rods.

The buffer vessel also acts as the PMT mounting surface where 354 PMTs are mounted pointing inward and optically isolates these PMTs from the veto volume. The size of the buffer vessel has been determined from the MC simulations.

The buffer vessel should be chemically inert against mineral oil inside and water outside. Also, it should withstand the stress from the loads coming from liquids and structures contained within. The buffer vessel is constructed with 6 mm thick 304L stainless steel for the top lid and barrel section, 12 mm thick for the bottom plate for extra mechanical support. The external view is shown in Fig. 3.3. The surface of the vessel is not polished. When the detector is filled with required liquids, the buffer vessel will experience buoyant force due to the density difference between the organic liquids inside the buffer vessel and water in veto layer. The buoyant force is estimated to be 11.5 tons and the buffer vessel supporting structure is designed to counter this force.

The buffer vessels are manufactured by Nivak co., Korea. They are transported as segmented pieces to the experiment site and assembled in the experimental halls. The barrel section consists of eight segments and top and bottom plates each consist of three segments. The bottom plate is welded to the barrel section and the top plate is bolted to the barrel section.

There are total 354 10-inch PMTs mounted on the inner side walls of the buffer vessel, 234 PMTs mounted on the barrel section, 60 each on the top and bottom plates, as shown in Fig. 3.4. PMTs will be mounted upright on the walls using the PMT holding structure described in Sect. 3.6.3.

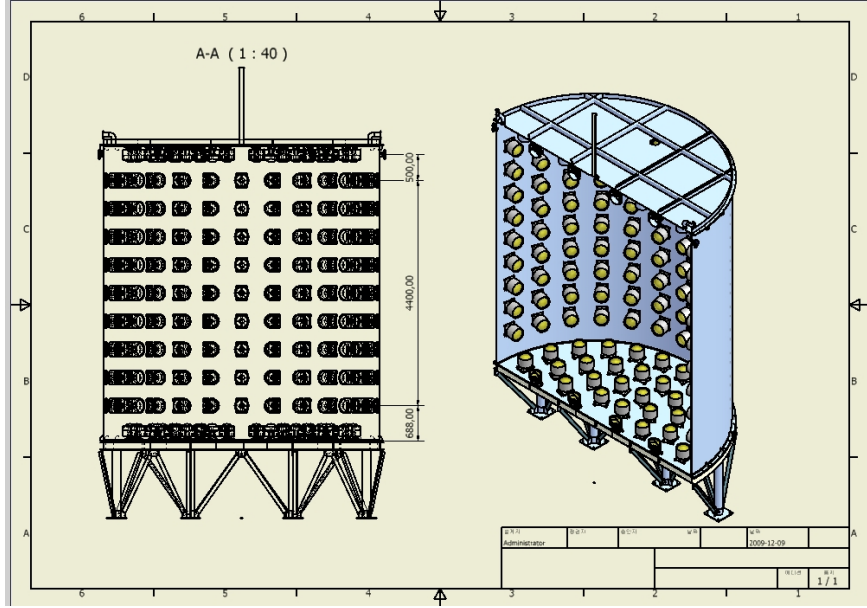


Figure 3.4: Inner detector PMT array on the buffer vessel. The PMTs are mounted on the vessel wall using the PMT holders. There are total 354 10-inch PMTs.

## 3.4 Veto System

### 3.4.1 Design Criteria

The veto system is located just outside of the buffer tank. The main background of the experiment is caused by cosmic muons, and it is very important to identify the entering muons since they can produce neutrons by muon-nucleus interaction in the detector. There are also correlated backgrounds by  $^9\text{Li}$  and  $^8\text{He}$  in the target and  $\gamma$ -catcher produced by muons. Although the veto system will not be included in the trigger, the muon signals in the veto system will be used to identify muon related background events for each candidate event from neutrino interaction. The veto vessel should be chemically compatible with water and strong enough to support all the three inner chambers before filling the liquids.

The rate of inverse beta neutrino events is about  $1 \text{ events} \cdot \text{km}^2 / (\text{GW} \cdot \text{ton} \cdot \text{day})$  for oil based liquid scintillator. One of the main backgrounds of RENO experiment will be fast neutrons which are generated in the surrounding rock and enter into the detector volume. We require that the fast neutron rate and the accidental coincidence rate from single rates of  $e^+$  signal ( $1 \text{ MeV} < E < 8 \text{ MeV}$ ) and neutron signal ( $6 \text{ MeV} < E < 10 \text{ MeV}$ ) are less than 1% of the inverse beta neutrino rate. The accidental rate from two uncorrelated single rates of  $R_1$  and  $R_2$  with a coincidence time window of  $\Delta T$  is  $R_{\text{accidental}} = R_1 R_2 \Delta T$ . The veto system should shield effectively the ambient gammas and also reduce the muon related background events by imposing an offline veto timing cut after each muon passing through the detector system. The results of Monte-Carlo simulations are described in Chapter 6. As a result, we set the thickness of the veto layer to be 1.5 m.

### 3.4.2 Structure

The inner diameter and height of the veto vessel are 8.4 m and 8.8 m, respectively. The vessel is constructed with a 40 cm thick concrete vessel. Inner surface of the concrete vessel

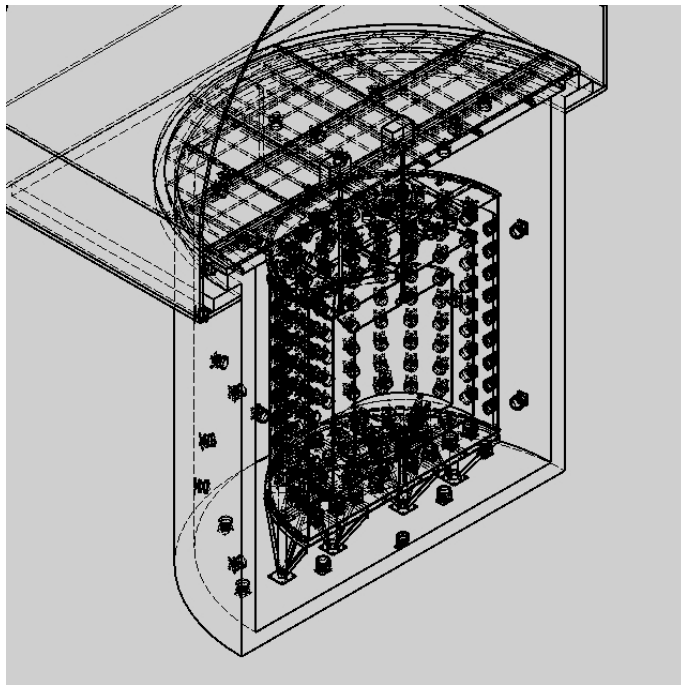


Figure 3.5: Transparent view of PMT arrays showing both the inner and outer PMTs.

was water-proofed with epoxy resin. The water will be purified at filling and continuously be circulated through a water purification system. There are 67 10-inch water-proof PMTs (R7081 Hamamatsu) attached on the inner surface of the veto vessel. The outer surface of buffer vessel and the inner surface of veto vessel will be coated with TiO<sub>2</sub> paint to increase the light collection of Cerenkov photons in the water. The whole PMT arrangements of both buffer and veto vessels are shown in Fig. 3.5.

### 3.5 Detector Assembly

The construction of the acrylic vessels, target and  $\gamma$ -catcher vessels, will be done at the manufacturer's facility but integrated into the detector system in the detector pit at the experiment site. The assembly procedure is as follows.

1. The target vessel with complete supporting structures and a chimney is assembled at the manufacturer's site. The  $\gamma$ -catcher vessel is also assembled at the manufacturer's facility. The lid and chimneys are for the  $\gamma$ -catcher vessel are not attached here.
2. The buffer vessel is constructed at the experiment hall pit. Shaping of the parts is done on site.
3. The  $\gamma$ -catcher and target vessels are transported to the experimental hall and integrated into the detector. The  $\gamma$ -catcher vessel is closed with a lid and chimneys are installed.
4. PMTs for the bottom and barrel sections are installed on both buffer and veto vessels.
5. PMTs are mounted on the buffer lid and the lid will be installed.
6. PMTs are mounted on the veto lid and the lid will be installed.

	R9512	R7081	XP1806	XP1804
Gain( $\times 10^7$ )	1.0 @1500 V	1.0 @ 1500 V	1.0 @1600 V	1.0 @1600 V
QE @ peak (nm)	22% @390	25% @390	24% @420	24% @420
DC (nA)	50	50	30	30
Size (inch)	8	10	8	10.6
Weight (g)	720	1150	880	1744
Rise Time (ns)	3.8	4.3	5	5
TTS (ns)	2.4	2.9	2.4	2.4
Afterpulse	2%	2%	12%	12%
Peak-to-valley ratio	4	3.5	3.5	3.5

Table 3.3: The specifications and measurements of the candidate PMTs. R5912 and R7081 are from Hamamatsu and XP1806 and XP1804 are from Photonis.

The detector construction will be done at the detector pit and in the service tunnel adjacent to it. The detector assembly area will be made a clean room of class 10 000. Environmental control units will keep the constant temperature and humidity. Near and far detectors will be constructed concurrently to reduce potential differences in the assembly procedure. After completing the assembly, all vessels will be filled simultaneously maintaining the differences in liquid levels within a few centimeter.

## 3.6 PMT and HV System

### 3.6.1 PMT Requirements and Specification

The scintillation lights from target and  $\gamma$ -catcher will be detected with PMTs attached on the inner surface of the buffer vessel. The number of detected photoelectrons is estimated to be 150 photoelectrons per MeV for an event occurring at the center of the target. Since the minimum energy deposited in the detector by a positron emitted in the inverse beta decay is 1.022 MeV, the average number of photoelectron per PMT in the buffer layer will be about 0.5. Therefore, the PMTs should be able to measure the single photoelectrons with high efficiency. The peak-to-valley ratio and the single photoelectron resolution of the PMTs are important parameters.

The main reason for having a non-scintillating buffer region is to shield the  $\gamma$ -catcher and the target from PMT's radioactivity. The radioactivity of PMTs needs to be studied to understand the rate of background originating from PMTs. The PMT background events are mainly in the low energy region of less than 2 MeV and could be misidentified as signals by accidental coincidence with neutron-like background events.

Since the PMTs will be immersed in a layer of mineral oil, it is also important that the whole PMT assembly is chemically inert to mineral oil. The oil proofing should be stable for the duration of the experiment.

The quantum efficiency of each PMT will be measured. We will measure the quantum efficiencies of all PMTs with a relative accuracy less than 5%. The outlying PMTs will be excluded from installation in the detectors.

### 3.6.2 Tests on PMT performance

We have tested four candidate PMTs for the RENO experiment; R5912 (8") and R7081 (10") from Hamamatsu, and XP1806 (8") and XP1804 (10") from Photonis. Table 3.3 shows the

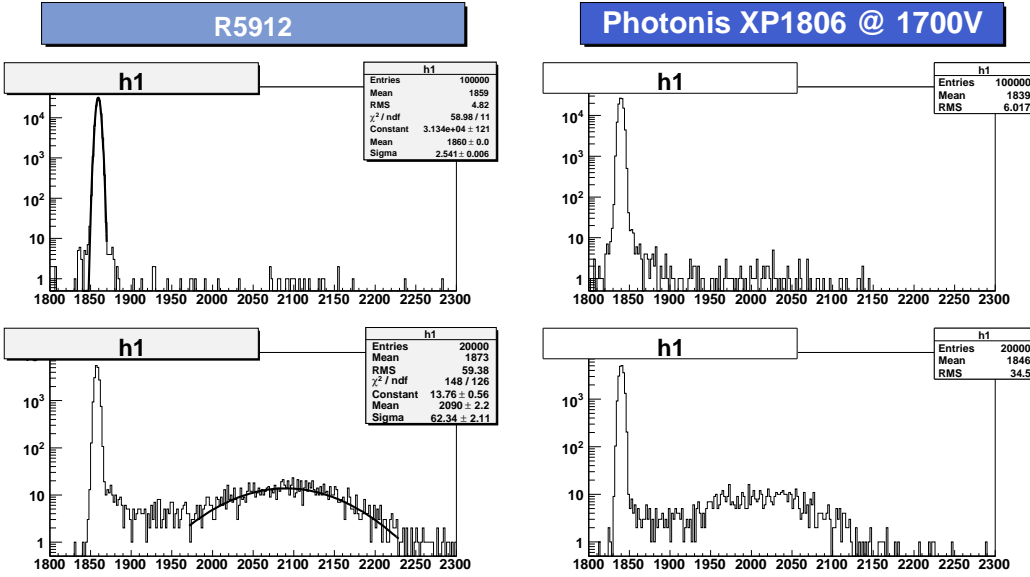


Figure 3.6: Single photoelectron spectra of 8-inch PMTs from Hamamatsu Co. and Photonis Co. Upper (lower) figure is obtained with LED off (on) for each PMT. X-axis is in ADC channel number.

company specifications and our measurements for the PMTs considered.

### Single photoelectron measurement

The single photoelectron spectra were measured with an LED flash system. The single photoelectron spectra of R5912 and XP1806 are shown in Fig. 3.6. The width-to-peak ratio of the single photoelectron measured with R5912 was 3.7. The operating voltages of R5912 and XP1806 were set to have the same gain of  $1 \times 10^7$  for the measurement.

### Background Measurements

The radioactive isotopes U, Th, and K in PMTs are most serious sources of the backgrounds. PMTs are located in the buffer filled with non-scintillating oil. The buffer layer thickness should be enough to reduce the single rates of gammas with energy over 1 MeV in the target and  $\gamma$ -catcher region to less than 20 Hz. The radioactivity of PMT is directly measured at the underground experimental facility of DMRC (Dark Matter Research Center) at Yangyang, Korea. A sample PMT was located on top of a low-background HPGe detector and the gamma rates from the whole PMT were measured. Even though the loci of radioactivity on PMTs are not measured, the rate of backgrounds coming from PMT can be reasonably estimated since the distance between PMTs and the outer boundary of  $\gamma$ -catcher is comparable to the size of PMTs (see Sect. 6.6.4). GEANT4 simulation is used to get the efficiency of the HPGe detector and a secular equilibrium is assumed for U and Th activities. The measured activities for the PMTs tested are summarized in the Table 3.4.

The activity of  $^{238}\text{U}$  in XP1806 PMT is about a factor of two higher than the Hamamatsu R5912 PMT. However,  $^{232}\text{Th}$  activity in XP1806 is lower than that in R5912. If the PMTs tested are used in RENO detector, the rate of single events with energy over 1 MeV is expected to be 20–50 Hz. PMTs with lower radioactivity are available, and the expected single event

PMT	$^{238}U$	$^{232}Th$	$^{40}K$
R5912(Hamamatsu)	$1.2 \pm 0.04$	$0.74 \pm 0.02$	$3.0 \pm 0.2$
R7801(Hamamatsu)	$4.8 \pm 0.07$	$2.2 \pm 0.03$	$13.1 \pm 0.4$
R7801(Hamamatsu)-Low	$0.72 \pm 0.1$	$0.59 \pm 0.07$	$3.3 \pm 0.3$
XP1806(Photonis)	$2.5 \pm 0.05$	$0.35 \pm 0.01$	$5.2 \pm 0.1$
XP1804(Photonis)	$5.9 \pm 0.2$	$0.63 \pm 0.06$	$9.4 \pm 0.2$

Table 3.4: The radioactivity of candidate 8- and 10-inch PMTs from Hamamatsu and Photonis. The units are Bq/PMT.

rate will be about 5–10 Hz.

To reduce the background from PMTs, Hamamatsu makes 10-inch PMTs with low background glass (R7081-Low). We measured radioactivities on two R7081-Low PMT samples. The background level of R7081-Low is found to be about 25% of that of the normal glass R7081 PMTs. This value is higher than the values given by Hamamatsu, but the measurements were performed over the whole PMT including base and cable. Also it was assumed that the spatial distribution of radioactivity was uniform in the glass part, so the true value of radioactivity is questionable. However, the ratio between normal glass and low background glass would be still valid. The measured level of radioactivity of low background glass PMTs would be acceptable for RENO experiment.

### Gain Drift and Afterpulse

The nominal gain of PMTs tested is  $\sim 10^7$ . However, the gain is temperature dependent and is measured to increase by about 0.2% per degree for the samples tested. The temperature will be monitored with a precision better than  $0.5^\circ\text{C}$ , so the gain error will be an order of 0.1%. This will give a negligible systematic uncertainty in the energy resolution and neutrino detection efficiency.

Afterpulse of 8- and 10-inch PMTs occurs at several  $\mu\text{s}$  after the primary pulse and its size is 1–10% of the primary pulse depending on the quality of individual PMTs. All the tested PMTs show two afterpulse peaks at 2 and 7  $\mu\text{s}$  after the primary pulse as shown in Fig. 3.7. The amount of afterpulse is 4–5% for Hamamatsu 8- and 10-inch PMTs, which is a factor of 2 higher than the company specification.

Even though the afterpulse has timing characteristics similar to the inverse beta decay events, the energy distributions between the primary and secondary pulses are quite different. For high energy muon events the size of the afterpulse could amount to a few MeV, while its primary pulse should have a huge signal in the same PMT. However, the occurrence of such an event is expected to be a few percent of the total high energy muon events, thus will not cause any significant impact on the experiment.

After considering various performance parameters, such as single photoelectron resolution, afterpulse rate, radioactivity in PMT, and overall detector performance to cost ratio, we decided to use 10-inch low background PMTs by Hamamatsu (R7081-Low) for the RENO experiment.

### PMT base

We have tested different base configurations with a sample R7081 PMT. The bases were home-made with Hamamatsu sockets following the voltage division given Hamamatsu. The bases also included back termination. First, we compared single-cable (HV and signal in a single

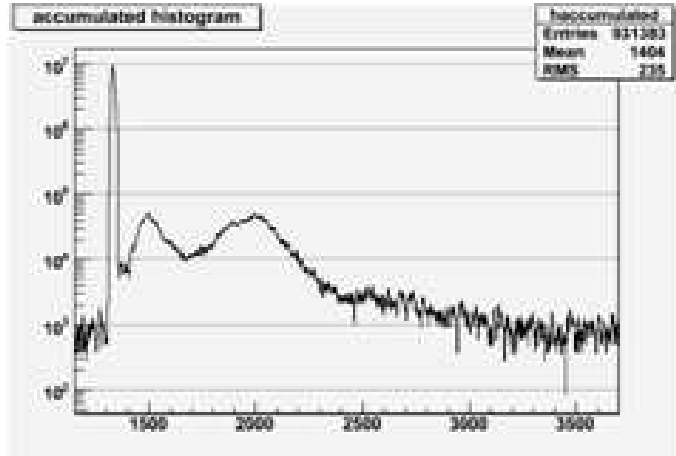


Figure 3.7: Afterpulse measurements of R5912 PMT. Two peaks occur at 2 and 7  $\mu$ s after the primary pulse. The unit of x axis is 10 ns.

cable) and two-cable (HV and signal in separate cables) base configurations. Second, two voltage divider configurations, 9.4 M $\Omega$  and 12.7 M $\Omega$  were tested. For all four base-cable configurations, the PMT signal gain was set at  $1.5 \times 10^7$ . The decoupling schemes for both single and two cable cases are shown in Fig. 3.8.

### SPE spectra

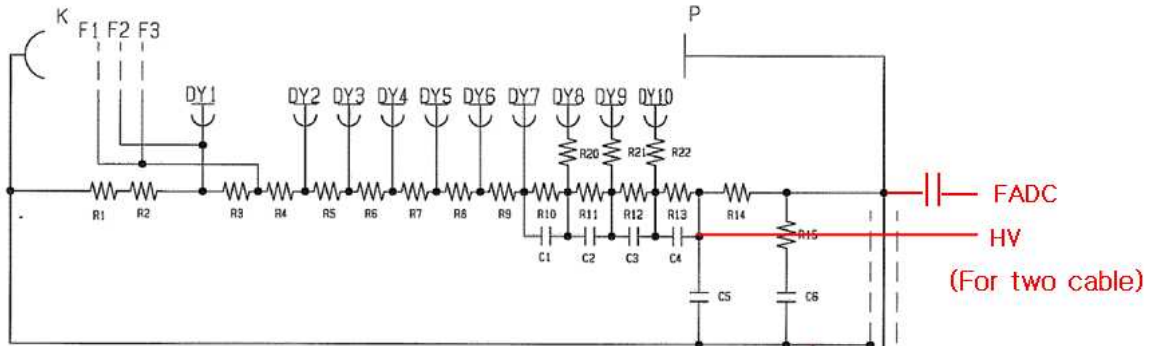
Single photoelectron spectra for all four base-cable configurations are shown in Fig. 3.9. There is little difference among four configurations. The 12.7 M $\Omega$  base appears to have a little higher quantum efficiency, maybe due to the efficient electron collection from photocathode. The 9.4 M $\Omega$  base has a higher gain than the 12.7 M $\Omega$  base, consistent with data provided with Hamamatsu.

### 3.6.3 PMT Holder

PMTs will be mounted on the inner wall of stainless steel buffer vessel. We want to minimize the amount of material while keeping the holding structure as stable as possible. Also the distance between PMT photocathode surface and buffer vessel should be minimized. The PMT holder is made of 1.5~2 mm thick stainless steel. The schematic is shown in Fig. 3.10. Two rings hold the glass bulb section of the PMT and the front ring defines the photosensitive area. The inner diameter of the rings is 12.3 cm. A mu-metal sheet surrounds the side of the structure to reduce the effects of external magnetic fields. The height of the mu-metal shielding will be determined based on the magnetic field survey at the experiment halls.

### 3.6.4 HV system

The PMTs are biased in such a way that the anode is connected to a positive high voltage and the cathode to ground. This prevents current leakage caused by discharges at the PMT glass. A schematic of the voltage divider of the PMT is shown in Fig. 3.11. A single cable (RG-303) will be used for carrying both high voltage and signal. A capacitor will decouple the high voltage and pulse signal from anode as shown in the schematic. The voltage difference between the photocathode and the first dynode is 622 V for an applied voltage of 1550 V.



R1, R2: 2.55 M $\Omega$  ( $\pm 5\%$  1/4 W)  
 R3: 180 k $\Omega$  ( $\pm 5\%$  1/4 W)  
 R4: 1.02 M $\Omega$  ( $\pm 5\%$  1/4 W)  
 R5: 1.5 M $\Omega$  ( $\pm 5\%$  1/4 W)  
 R6: 1 M $\Omega$  ( $\pm 5\%$  1/4 W)  
 R7: 499 k $\Omega$  ( $\pm 5\%$  1/4 W)  
 R8: 300 k $\Omega$  ( $\pm 5\%$  1/4 W)  
 R9: 360 k $\Omega$  ( $\pm 5\%$  1/4 W)  
 R10: 430 k $\Omega$  ( $\pm 5\%$  1/4 W)  
 R11: 680 k $\Omega$  ( $\pm 5\%$  1/4 W)  
 R12: 910 k $\Omega$  ( $\pm 5\%$  1/4 W)  
 R13: 750 k $\Omega$  ( $\pm 5\%$  1/4 W)  
 R14: 10 k $\Omega$  ( $\pm 5\%$  1/4 W)  
 R15: 49.9  $\Omega$  ( $\pm 1\%$  1/4 W)  
 R20-R22: 51  $\Omega$  ( $\pm 5\%$  1/4 W)  
 C1-C4: 10 nF (200 V)  
 C5, C6: 14700 pF (3 kV)

TOTAL RESISTANCE = 12.7 M $\Omega$   
 DIVIDER CURRENT: 158  $\mu$ A at +2000 V (MAX.)

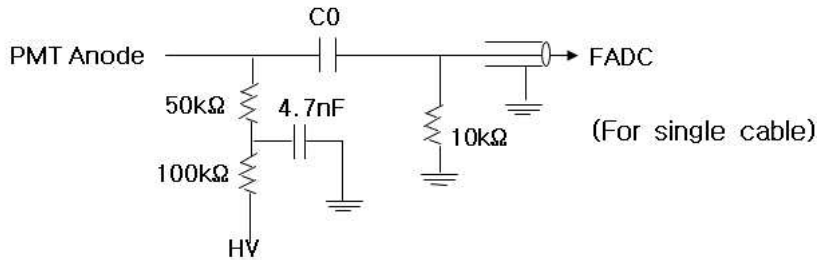


Figure 3.8: Single-cable (HV and signal via a single cable) and two-cable (HV and signal in separate cables) base configurations for the 12.7 M $\Omega$  base. Top figure is the decoupling circuit for two cable configuration with cables shown in red lines.

A 50  $\Omega$  termination will be in the PMT base side to match the impedance and the signal will be attenuated by a factor of two compared to the two cable case where signal is carried by a separate cable. Therefore, a higher voltage will be applied to compensate for the signal amplitude reduction. The cable length is 25 meter, identical for all the PMTs mounted in the buffer vessel.

For the high voltage module, two models of high density modules, A1932A (48 channel, 0.5 mA/channel, 8 channel/group) and A1535 (24 channel, 1 mA/channel), are being considered. For both modules, the schematic shown in the Fig. 3.11 can be applied. For A1535 modules, one HV channel will be used to bias four PMTs. This channel splitting scheme has been tested on the mock-up detector and no noticeable cross talk or increased noise level were observed.

For a detector, we have 421 PMTs. These PMTs will be in nine groups in HV supplying system as shown in Fig. 3.12. Each group consists of one A1932 48 channel HV supplying module and 48 channel decoupler box as shown in Fig. 3.11. Three 19" racks will house the whole system.

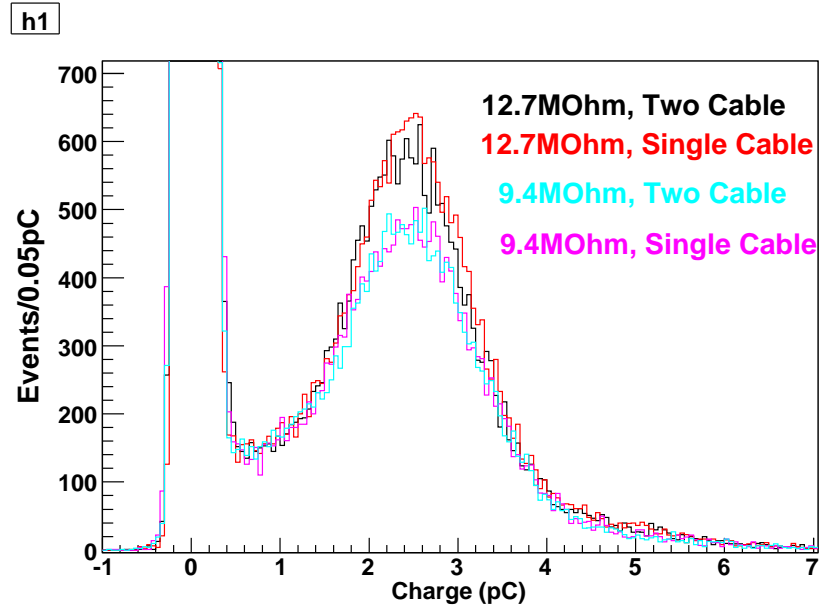


Figure 3.9: Single photoelectron spectra for four base-cable configurations.

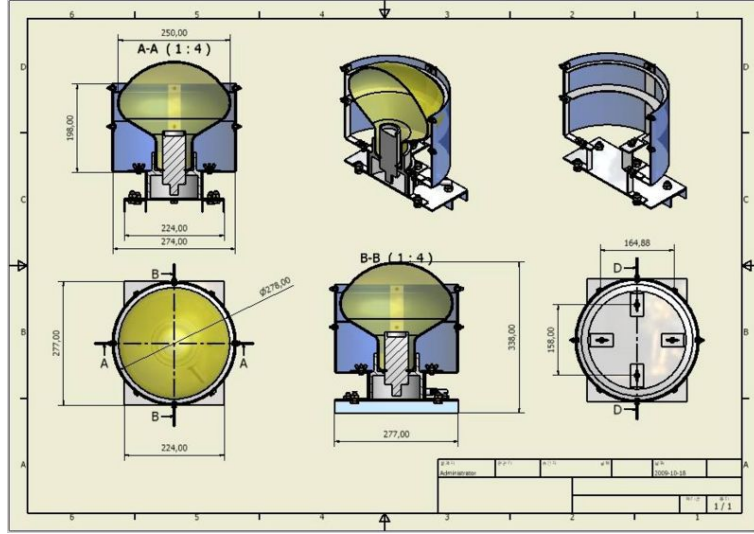


Figure 3.10: A design of PMT holder. Two stainless steel rims hold the glass of 10-inch PMT. A cylinder shape mu metal sheet will be outside of the rings surrounding the individual PMT to reduce the effect of the magnetic field.

## 3.7 Prototype Detector

The small prototype detector is built to test properties of liquid scintillators and validate the Monte Carlo simulation model based on GEANT4.

### 3.7.1 Detector Design

The prototype detector consists of two concentric cylindrical vessels filled with liquid scintillators with a cylindrical dark box surrounding the vessels. The vessels are 100 mm and

### HV Decoupler(48ch. Individual) circuit Signal Read-out Schematics

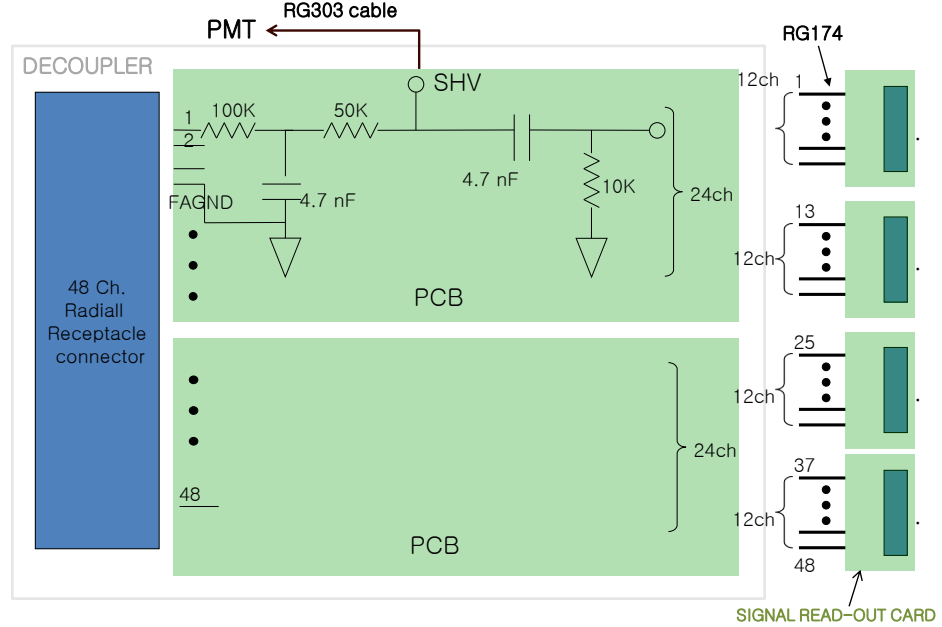


Figure 3.11: A schematic of 48 channel decoupler with a 48 channel HV power supplier module A1932P.

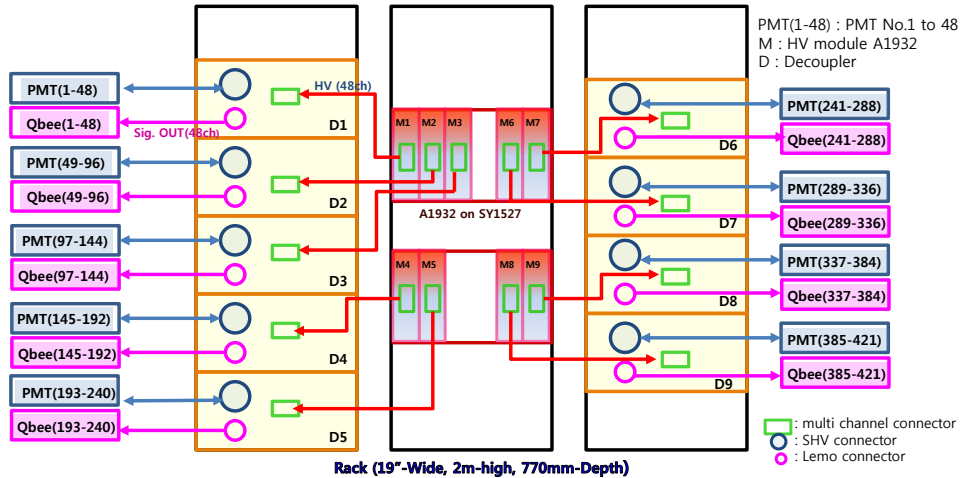


Figure 3.12: HV supplying and decoupling system for a detector of 421 PMTs. Each group consists of one A1932 48 channel HV supplying module and 48 channel decoupler box.

210 mm in diameter and 300 mm and 610 mm in height, respectively, and made of 10 mm thick transparent acrylic plastic. The smaller vessel is filled with Gd-loaded liquid scintillator (target) and the larger one with liquid scintillator ( $\gamma$ -catcher). There are ten equally spaced 5-inch PMTs mounted on the barrel section of the dark box through holes. The schematics and pictures of the assembly are shown in Fig. 3.13.

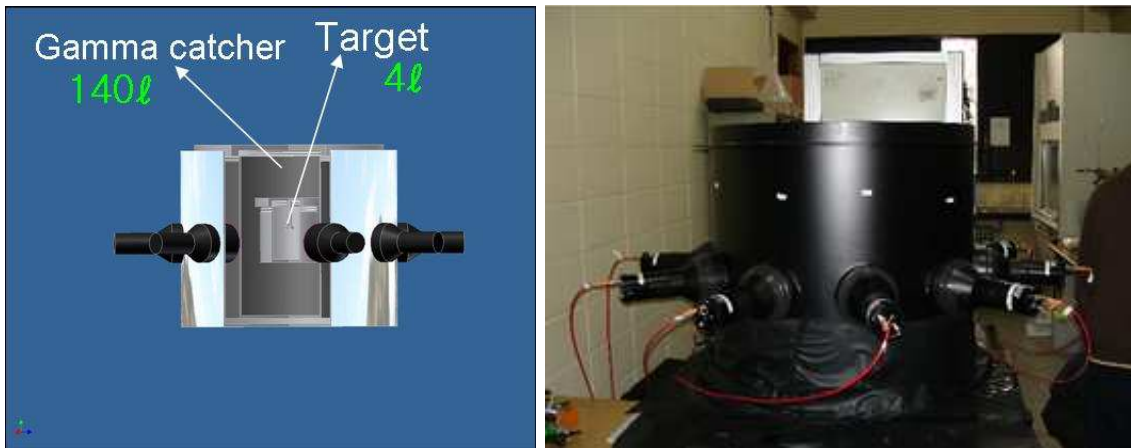


Figure 3.13: The prototype detector. Cut-away view of target and gamma catcher (left) and a picture of the exterior of the detector (right).

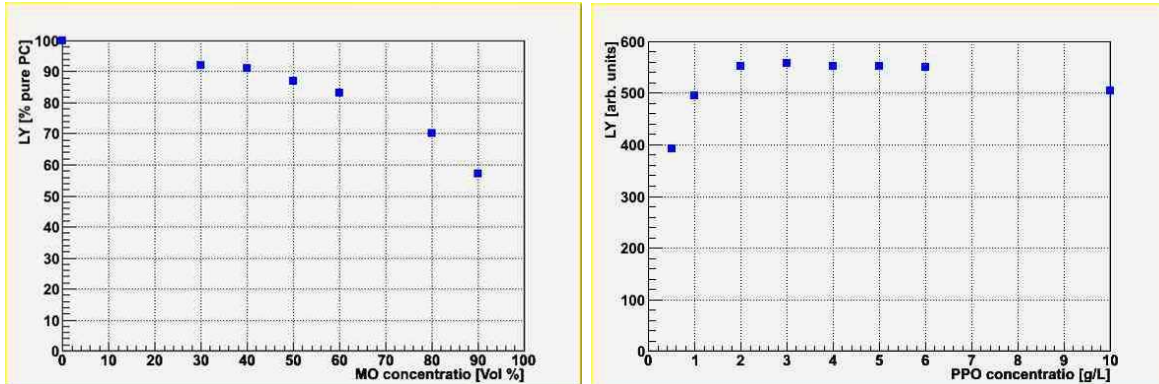


Figure 3.14: The light yield of PC and MO mixture as a function of MO concentration (left) and PPO concentration (right). About 85% light output is shown at the 60% MO with respect to pure PC. The highest light yield is shown at the 3 g/l PPO concentration.

### 3.7.2 Liquid Scintillator Mixture

The liquid scintillator used in the prototype detector consists of solvent, admixture of 40% pseudocumene (PC) and 60% mineral oil (MO) by volume, added with 3 g/l PPO and 0.05 g/l bis-MSB as fluor and wavelength shifter, respectively. This solvent mixture gives a light output of  $\sim 85\%$  with respect to that of pure PC. The target liquid scintillator is loaded with 1 g/l Gd. Table 3.5 summarizes the liquid scintillator mixture.

To prevent the deterioration in light yield by the oxidation of the solvent through the contact with air, Argon gas was bubbled through the liquid scintillator whenever the liquid scintillator was exposed to air. The material compatibility of the liquid scintillator with acrylic vessel was checked in a long term test. The performance of the liquid scintillator with various mixing ratios were tested. The results are shown in Fig. 3.14. For a detailed description of liquid scintillator, see Sect. 4.

	PC	MO	PPO	bis-MSB	Gd
Target	1.6 l	2.4 l	12 g	0.2 g	4.0 g
Gamma catcher	56.0 l	84.0 l	620 g	7.0 g	0.0 g

Table 3.5: Summary of liquid scintillator admixtures used in the prototype detector.

### 3.7.3 Electronics, Trigger, and DAQ Systems

#### Electronics

For the front-end electronics of the prototype detector, we utilized off-the-shelf commercial products. We used an 8-channel flash analog-to-digital converter (FADC) VME module with an 100 MHz sampling rate. The FADC has a 10-bit pulse height digitization. Since a typical signal pulse has a width of about 20 ns, FADC with an 100 MHz sampling rate (10 ns bin) has an inadequate time resolution to see the signal pulse structure. Therefore, the PMT signal was stretched five times in time before digitization.

#### Trigger and DAQ

A simple trigger and DAQ system was used for the prototype. We required a two-channel coincidence to collect events from  $\gamma$  sources. If any of two PMT channels fired, then the event was accepted and sent to FADC for digitization (see Sect. 3.7.4).

### 3.7.4 Performance

We analyzed the single photoelectron spectra using an LED light source. The energy resolution for the SPE events was measured to be  $\sim 50\%$ . The trigger threshold for each channel was set to fire for signal above 0.5 photoelectrons.

To measure the detector performance, a  $\gamma$  source, either  $^{137}\text{Cs}$  or  $^{60}\text{Co}$ , was placed at the center of the target. The results were compared to the simulation based on GEANT4. The threshold behaviour observed in data was modelled and applied to the Monte Carlo samples and the same trigger conditions were used for event selection.

Figure 3.15 shows the energy spectra obtained for  $^{137}\text{Cs}$  and  $^{60}\text{Co}$ . The background distribution was obtained from data collected without any sources in the detector. The energy response is estimated as 102 photoelectrons per MeV. We see discrepancies between data and Monte Carlo samples near the peak in both cases. It is under investigation.

## 3.8 Mock-up Detector

The mock-up detector is built to test the detailed design features as well as various subsystems to be incorporated into the full detector. It is also used to do a long term test on the performance of liquid scintillator and its compatibility with acrylic.

### 3.8.1 Design of the Mock-up Detector

The mock-up detector is about 1/15 of the full detector in volume. However, it has most features of the full detector to check the validity of the design features in the full detector as well as the performance of various detector components. The mock-up detector has structural similarities to the full detector; cylindrical target,  $\gamma$ -catcher, and buffer layers. However, it lacks a veto layer. The vessels are made of the same materials as those of the full detector. The

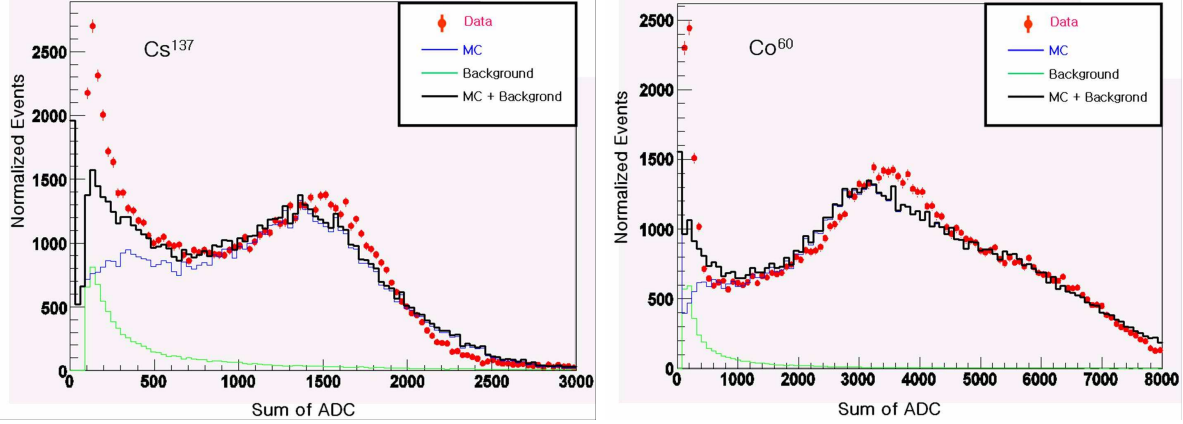


Figure 3.15: Energy spectra for  $^{137}\text{Cs}$  (left) and  $^{60}\text{Co}$  (right) measured with the prototype detector. The horizontal axis is the sum of ADC values over all PMT channels. The red dots indicate the on-source data and bold black histogram indicate the Monte Carlo sample with background estimation included. The Monte Carlo sample distributions are normalized to the data.

Chamber	Diameter	Height	Thickness of vessel
Target	60 cm	60 cm	10 mm
Gamma Catcher	120 cm	120 cm	10 mm
Buffer	220 cm	220 cm	4 mm/5 mm*

Table 3.6: Dimensions of the mock-up detector. ((\*)The thickness of SUS at side is 4 mm and the top and bottom are 5 mm.)

same model of 10-inch PMTs as in the full detector are used. Figure 3.16 shows the overall design of the mock-up detector and Table 3.6 shows the dimensions of the detector.

The sizes of the target and  $\gamma$ -catcher were determined such that the detector can measure most of neutron capture signal. The buffer layer is 50 cm thick to accommodate 10-inch PMTs and is filled with mineral oil. The Linear Alkyl-benzene (LAB) based scintillator is filled through chimneys connecting to target and  $\gamma$ -catcher vessels. The buffer vessel, made of stainless steel, is 4 mm thick for the side and 5 mm for top and bottom. The target vessel is constructed with a casted acrylic tube from Reynolds Co., USA. The  $\gamma$ -catcher vessel is made with GS233 Plexiglass casted acrylic supplied by Degussa GmbH, Germany and shaped as a cylindrical tube.

There are 31 10-inch PMTs(R7081) installed on the inner surface of the buffer vessel; 7 on the bottom, 6 on the top, and 18 on the side. The surface coverage of the PMT photocathode is 8%. PMTs are held in place by the PMT holders made with a 2 mm thick stainless steel strips. In mineral oil the side mounted PMTs shifted upward about 2 mm from the nominal position by buoyant force but stayed stable. All PMT cables are bundled together and potted with epoxy for sealing and are extracted to the outside of the buffer chamber.

A glove box is on top of the buffer vessel housing the calibration source driving system. The calibration sources are inserted in target or  $\gamma$ -catcher through chimneys. Two chimneys, one for target and the other for  $\gamma$ -catcher, are installed for filling liquids and transporting calibration sources. A part of each chimney is made with a 3-inch PTFE flexible tubes to relieve the stress between the acrylic vessels and the buffer vessel. The calibration source

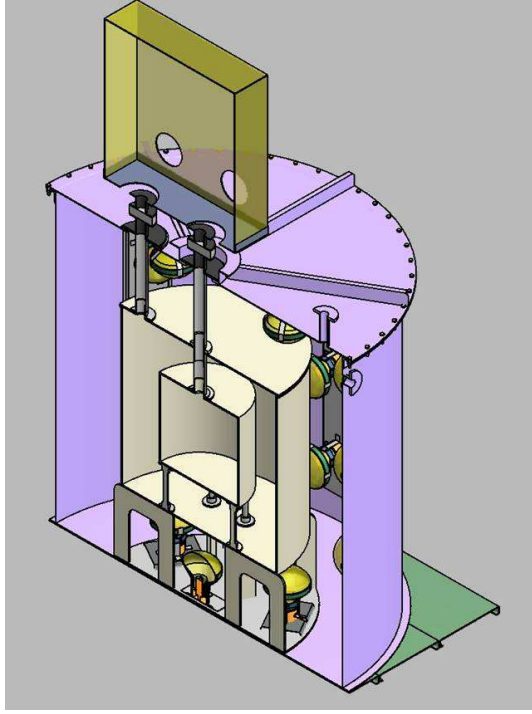


Figure 3.16: Cut-away view of mock-up detector. It has two layers of liquid scintillator (target and  $\gamma$ -catcher) contained in acrylic vessels surrounded by a non-scintillating mineral oil (buffer) in a stainless steel vessel. There are 31 10-inch R7081 PMTs mounted on the buffer vessel walls. The mock-up is about 1/15 of the full size detector in volume. A glove box housing calibration source driving system is installed on the top of the detector. Sources can be inserted in the target and  $\gamma$  catcher.

driving system is described in the Sect. 7.4. Each calibration source is enclosed in a 3 cm acrylic container and can be placed at various depths in the target and  $\gamma$ -catcher. Figure 3.17 shows the pictures of the constructed acrylic vessel assembly.

### 3.8.2 Performance of Mock-up Detector

The background rate is high because the mockup detector is installed at the ground level without much shielding. The 50 cm-thick mineral oil layer in the buffer reduces the ambient gamma background by more than a factor of ten. The background rate was reduced to  $\sim 10$  kHz over 100 keV energy threshold.

The gains of the PMTs were adjusted to be  $1.5 \times 10^7$ . Both target and  $\gamma$ -catcher were filled with LAB based liquid scintillator. The DAQ system is based on a 400 MHz FADC described in Sect. 3.9. The time window for an event was set at 320 ns and the signal starts at around 80 ns. The threshold of PMT signal was set to be 3 mV. At least five PMTs are required to have signal above the threshold to accept the event. This condition makes the total energy threshold at about 100 keV.

Figure 3.18 shows the number of photoelectron distributions obtained with  $^{137}\text{Cs}$ ,  $^{68}\text{Ge}$ , and  $^{60}\text{Co}$  sources. The expected background contribution obtained from data taken without the source was subtracted. The measured number of photoelectrons per MeV is 70. The overall spectral shapes of the source data were reproduced well with the GEANT4 based simulation. An acceptable linearity between energy values of the radioactive sources and the number of



Figure 3.17: Target and  $\gamma$ -catcher vessel assembly of mock-up detector (left) and with PMTs attached on the inner surface of the buffer vessel (right). The thickness of acrylic vessel is 1 cm.

measured photoelectrons.

### 3.9 DAQ System for Mock-Up Detector

The data acquisition system is based on 400 MHz flash analog-to-digital converter (FADC) as shown in Fig. 3.19. Eight FADC boards are installed in the two VME crates and two personal computers are used for data taking and online monitoring. After timing synchronization between the hit data from the VME crates, events are built. Figure 3.20 shows the photoelectron distribution produced by a  $^{137}\text{Cs}$  source inside of mockup detector. The reconstructed events are used to understand the performance of the mockup detector.

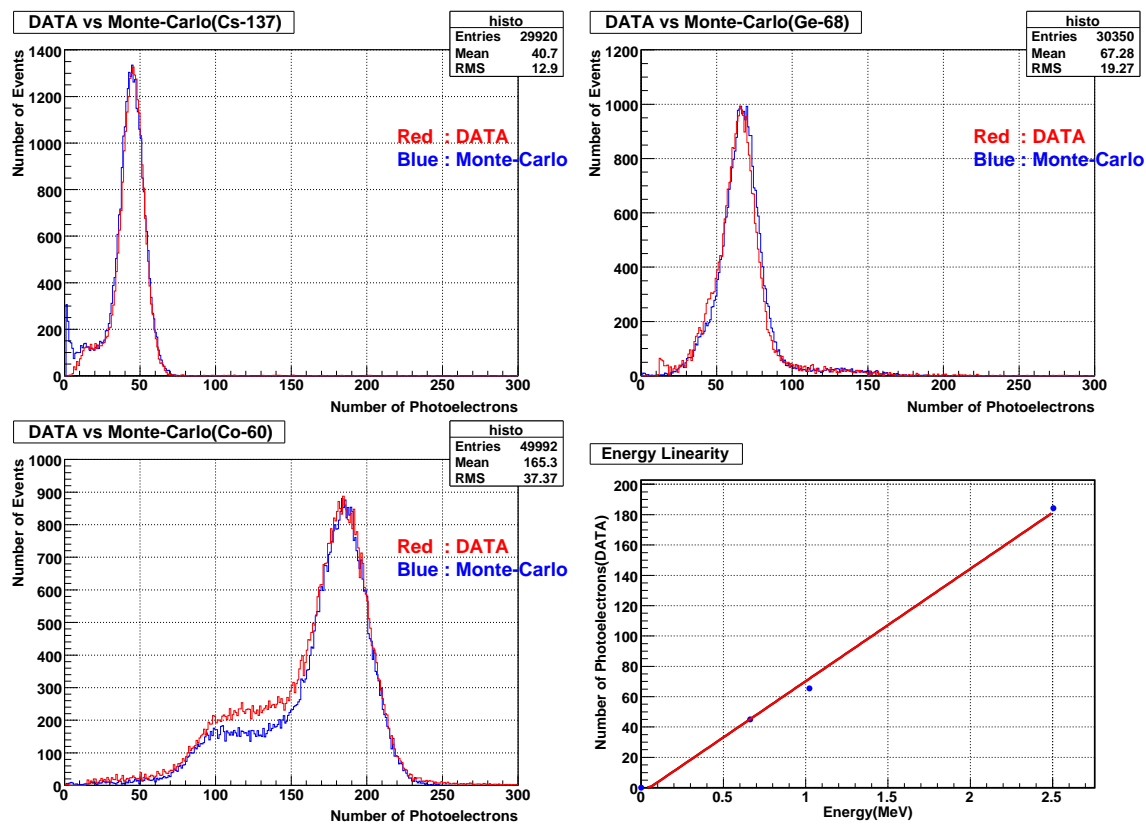


Figure 3.18: The number of photoelectron distributions of  $^{137}\text{Cs}$  (top left),  $^{68}\text{Ge}$  (top right), and  $^{60}\text{Co}$  (bottom left) sources placed at the center of target. The red histograms are the data and the blue histograms are the results of GEANT4 simulations. The bottom right figure shows the linear correlation between the measured and simulated number of photoelectrons.

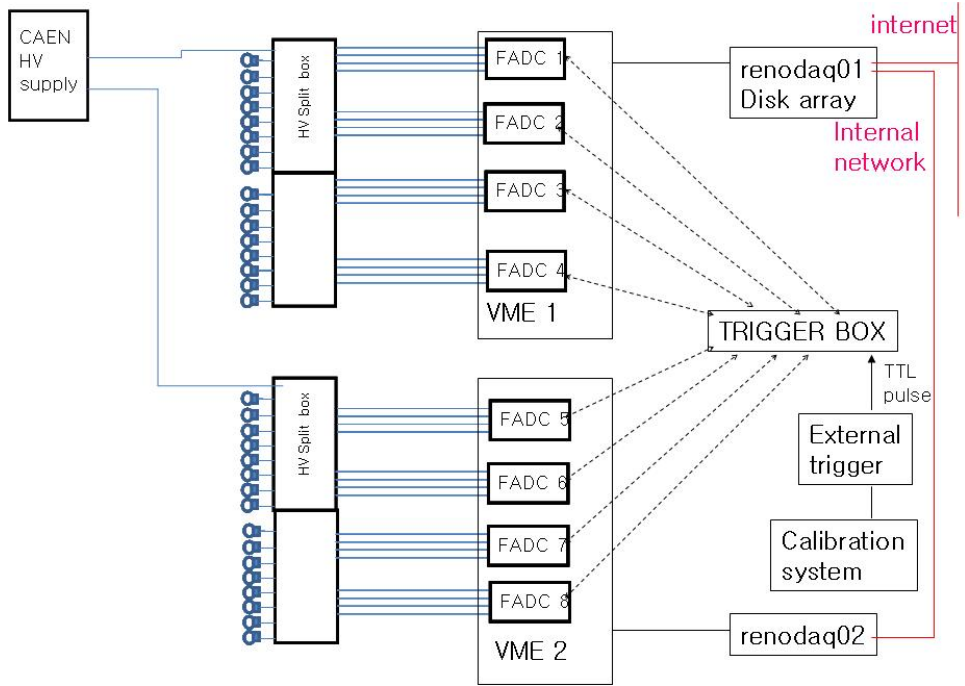


Figure 3.19: A schematic diagram of DAQ system for the mock-up detector. Each 400 MHz FADC board reads and digitizes the signals from four PMTs. An event is accepted if there are hits above 3 mV on more than five PMTs.

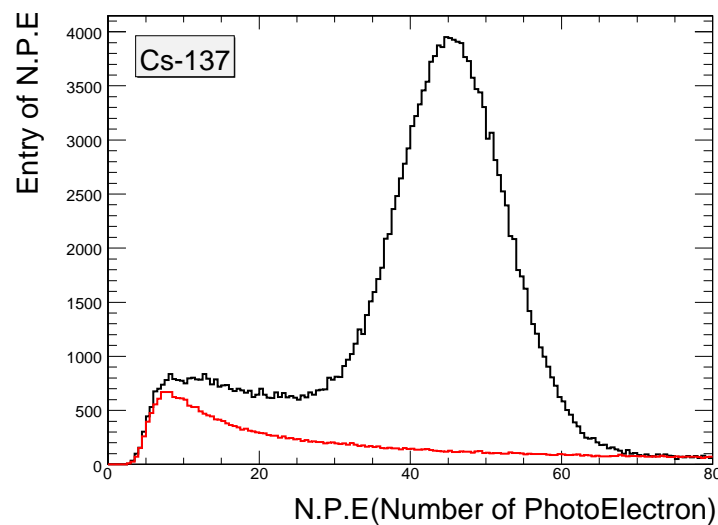


Figure 3.20: Distribution of photoelectron of  $^{137}\text{Cs}$  source. Data is taken with the threshold at 3 mV and multiplicity of 5.

# Chapter 4

## Liquid Scintillator

### 4.1 Introduction

The reactor anti-neutrinos are detected through the inverse beta decay process followed by a neutron capture. The prompt positron yields  $1 \sim 8$  MeV of visible energy. When a neutron is captured by a hydrogen, which forms a deuteron giving off photons with total energy of  $\sim 2.2$  MeV. However, when the liquid scintillator (LS) is loaded with Gadolinium (Gd), which has a very large thermal neutron capture cross section than a free proton, the delayed neutron capture signal is enhanced significantly over the radioactive background by producing photons with total energy of  $\sim 8$  MeV.

Liquid scintillators are contained in the target and  $\gamma$ -catcher layers of the RENO detector. Detection of a small energy deposit will be possible only if the scintillator has excellent light output and optical clarity. It is also required that the liquid scintillator should be relatively easy and safe to handle, cost effective to produce, and have desirable physical and chemical properties.

### 4.2 Liquid Scintillator and Buffer Fluids

The RENO detector uses organic liquids in target,  $\gamma$ -catcher, and buffer as summarized in Table 4.1. The acrylic vessel holding the target liquid is surrounded by the  $\gamma$ -catcher. The densities of the liquids should be similar in all volumes to minimize stress exerted on detector structures due to buoyancy force.

Important considerations for the liquid scintillator are light yield, stability, and radiopurity. Light yield requirement could be satisfied by the selection of adequate solvent and optimization of fluor concentration.

Region	Radius(mm)	Height(mm)	Volume (m <sup>3</sup> )	Type
Target	1388	3176	19.21	0.1% Gd loaded LS
Target vessel	1400	3200	0.48	Acrylic
$\gamma$ -catcher	1985	4370	34.37	Unloaded scintillator
$\gamma$ -catcher vessel	2000	4400	1.20	Acrylic
Buffer	2694	5788	76.64	Non-scintillating oil

Table 4.1: Organic liquids used in various parts of the RENO detector.

#### 4.2.1 Specification

The organic liquids should have good transparency, large attenuation length, high radiopurity, and chemical stability. Also, each liquid should have the following additional requirements: a) Gd-loaded scintillator (target) should have good light yield and high H/C ratio, b) scintillator ( $\gamma$ -catcher) should have a good light yield, and c) mineral oil (buffer) should be non-scintillating and has a similar density to liquids scintillator.

#### 4.2.2 Organic Solvent

Liquid scintillator consists of aromatic organic solvent, fluor, and wavelength shifter as shown in Table 4.2. A benzene ( $C_6H_6$ ) or benzene compounds have been used as aromatic solvent because of its excellent light transmission properties. Several aromatic scintillation liquids have been studied for RENO experiment.

Pseudocumene (PC or TMB,  $C_9H_{12}$ , 1,2,4-trimethylbenzene) is the most commonly used solvent for Gd-loaded liquid scintillator (Gd-LS). PC gives the highest light output among the widely used liquid scintillators. However, it attacks acrylic materials and has a low H/C ratio of 1.66. It is also flammable with low flash point ( $48^\circ C$ ) and develops harmful fume. Therefore, PC is usually used in an admixture with diluent solvents. The concentration of PC is determined by optimizing for the flash point, light output, and transparency. It is nearly insoluble in water, but well soluble in ethanol and benzene.

Another aromatic solvent, 1,2-dimethyl-4-(1-phenylethyl)-benzene (phenyl-o-xylythane, PXE,  $C_{16}H_{18}$ ), can be a candidate. Its flash point is  $145^\circ C$  and density is  $0.980 \sim 1.000 \text{ g/cm}^3$  at  $15^\circ C$ , but it has an even lower H/C ratio ( $\sim 1.37$ ) than PC. Borexino experiment [1] used PXE as the organic liquid scintillator due to its high density and high flash-point. Double Chooz experiment has proposed to use PXE [2].

Organic solvent should have good compatibility with acrylic vessel. Although PC has good light yield and optical properties, the compatibility with acrylic vessel is not good. Dilution component is added to PC to increase compatibility with acrylic vessel. Mineral oil (MO,  $C_nH_{2n+2}$ , where  $n = 11 \sim 44$ ) is used for a diluent solvent. Its density varies  $0.7 \sim 0.9 \text{ g/cm}^3$  depending on the products and manufacturers. A widely used liquid scintillator is a mixture of 40% PC and 60% MO and has a H/C ratio of  $\sim 1.87$ .

Instead of MO as a diluent solvent, dodecane ( $C_{12}H_{26}$ ) can be used. Normal dodecane does not have double chemical bonding nor a circular structure. It means that it is chemically stable and immune to oxidization. Normal dodecane has a higher flash point ( $83^\circ C$ ) than PC and, therefore, adding normal dodecane to aromatic solvent with a low flash point significantly improves the safety of liquid scintillator. Dodecane has a high H/C ratio of 2.17. Normal dodecane is produced by distillation normal paraffins within a very narrow temperature window. Therefore, its purity level is very high.

Because the liquid scintillator serves as a neutrino target in reactor neutrino experiments, it should have a high H/C ratio and its proton density should be known precisely. The solvents used in Palo Verde and CHOOZ experiment are admixtures of PC and MO. Mineral oil is liquid paraffin which has a high H/C ratio and a good light yield. The light yield of liquid scintillator is measured with Compton edge of gamma rays emitted from a radioactive source. For the light yield measurement,  $^{60}\text{Co}$  and  $^{137}\text{Cs}$  are used.<sup>1,2</sup> The light yield of MO increases

<sup>1</sup>  $^{60}\text{Co}$  ( $E_\gamma = 1173.2, 1332.5 \text{ KeV}$ ) has two Compton edges and  $^{137}\text{Cs}$  ( $E_\gamma = 661.6 \text{ KeV}$ ) has one Compton edge ( $447 \text{ KeV}$ ).

<sup>2</sup>For light yield measurement, Dodecane, Decane, and several MO samples with different kinetic viscosity values were prepared; Aldrich, KF-50, KF-70, KF-250, and KF-400. A larger KF number refer to higher kinetic viscosity. KF-series MO and decane are produced by SeoJin Chemical Co. and “Aldrich” MO and dodecane

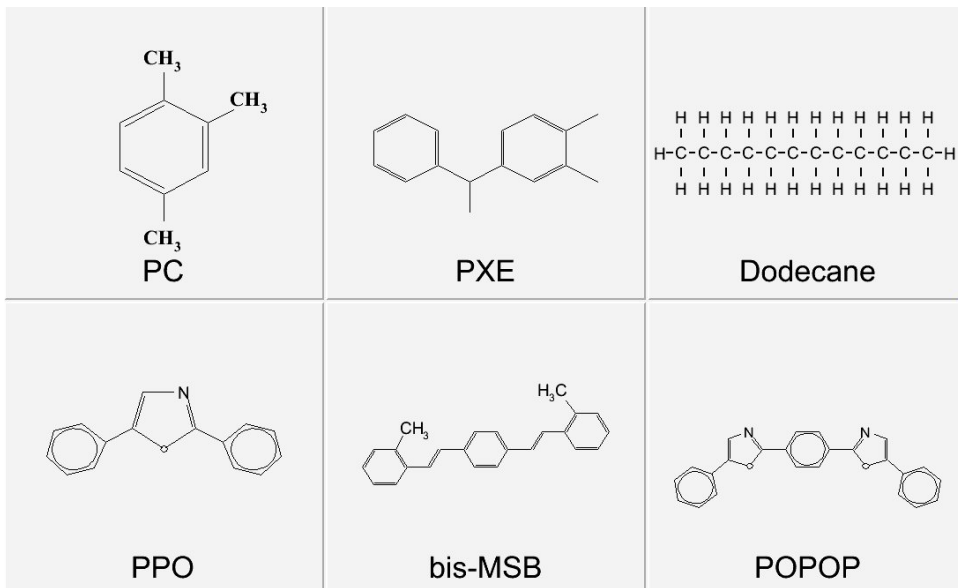


Figure 4.1: Chemicals used in liquid scintillators for the reactor neutrino experiments.

Aromatic Solvent	Diluent Oil	Fluor	WLS
PC, PXE DIN, PCH	Mineral Oil, Dodecane Decane, Tetradecan	PPO, BPO, PTF p-pTp, PMP, PDB	bis-MSB, POPOP

Table 4.2: Chemicals generally used for liquid scintillator admixtures.

as kinetic viscosity decreases. Dodecane based liquid scintillator has small light yield relative to MO based one because it has single bond between neighboring atoms whereas MO has some double bonds between neighboring atoms.

Initially we took the admixture of 40% PC and 60% MO, by volume, which is used by Palo Verde experiment [3], as a starting point of our organic solvent R&D. The addition of MO to PC reduces the light yield, but it improves the chemical compatibility with the acrylic. However, LAB has shown many advantages over the PC-diluent admixture and it will be used as the solvent for liquid scintillator for our experiment. This is described later in this chapter.

#### 4.2.3 Various Fluors

2,5-diphenyloxazole (PPO, C<sub>15</sub>H<sub>11</sub>NO) is used as the primary scintillation solute. Its emission spectrum peaks at  $\sim$ 360 nm. PPO is a fluor which has been widely used in liquid scintillators for high energy physics. In addition, BPO (2-(4-biphenyl)-5-phenyloxazole) and p-terphenyl (PTF) can be used. Unlike PPO, BPO does not need secondary wavelength shifter. However, BPO is more expensive than PPO.

1,4-bis(phenyl-2-oxazolyl)-benzene (POPOP, C<sub>12</sub>H<sub>16</sub>N<sub>2</sub>O<sub>2</sub>) is used as a wavelength shifter, whose absorption spectrum peaks at 385 nm and emission spectrum at 418 nm. For a secondary wavelength shifter, 1,4-bis(2-methylstyryl)-benzene (bis-MSB) could be used. Figure 4.1 shows molecular structure of various chemicals used as solvents, fluors, and wavelength shifters.

---

are purchased from Aldrich.

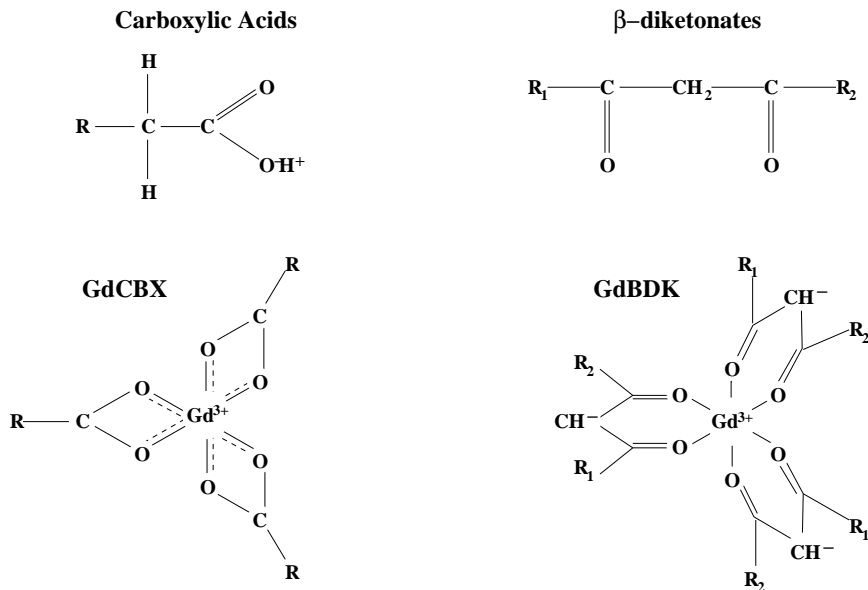


Figure 4.2: Gd compound structures of carboxylic acid and  $\beta$ -diketonate ligands. A range of liquid carboxylic acid radicals with different alkyl chains exist: C2 (acetic acid), C3 (propionic acid), C4 (isobutyl acid), C5 (isovaleric acid), C6 (2-methylvaleric acid, C5H11COOH, HMVA), C8 (ethyl-hexanoic), and C9 (trimethyl-hexanoic).

#### 4.2.4 Target

The hydrogen atoms (“free proton”) in the liquid scintillator serve as the antineutrino target in the inverse beta decay reaction. When a neutron is captured by a free proton, gamma rays with a total energy of  $\sim 2.2$  MeV are emitted. On the other hand, a neutron capture on a Gd atom leads to an emission of gamma rays with a total energy of  $\sim 8$  MeV, much higher than the energies of the gamma rays from natural radioactivities which are normally below 3.5 MeV. The mean thermal neutron capture cross section of Gd isotopes is four orders of magnitude larger than that of proton. Hence the liquid scintillator doped with a small amount of Gd is ideal for detecting inverse beta decay events.

Gadolinium is a silvery white soft ductile metal belonging to the lanthanide group. It is one of the most abundant rare-earth elements. It is never found as free element in nature, but is contained in many rare minerals. The metal does not tarnish in dry air, but oxide film forms in moist air. Gadolinium reacts slowly with water and dissolves in acids. It can form stable organometallic complexes with ligands such as carboxylic acids ( $\text{R}-\text{COOH}$ ) and  $\beta$ -diketones. Figure 4.2 shows molecular structures of Gd compounds with ligands.

It is difficult to add inorganic Gd salt to organic liquid scintillator to make a stable Gd loaded liquid scintillator. However, two formulations for Gd loaded liquid scintillator have shown promising results; liquid scintillators with Gd binding with carboxylate (CBX) ligands and with  $\beta$ -diketonate (BDK) ligands. Double Chooz and Daya Bay experiments report that both BDK and CBX Gd loaded liquid scintillators have excellent performances. Among these, TMHA is reported to be most promising [4].



Figure 4.3: White Gd-TMHA salt after filtration with  $0.2 \mu\text{m}$  pore size Teflon membrane filter.

#### 4.2.5 Synthesis of Gd-Complex

Since metal Gd by itself cannot be dissolved in the organic solvent, Gd salt with ligands is used. We chose to use CBX as our basis for ligands after consideration. There are three steps in synthesizing the Gd-carboxylate compound:

1.  $\text{Gd}_2\text{O}_3 + 6\text{HCl} \rightarrow 2\text{GdCl}_3 + 3\text{H}_2\text{O}$
2.  $\text{RCOOH} + \text{NH}_3 * \text{H}_2\text{O} \rightarrow \text{RCOONH}_4 + \text{H}_2\text{O}$
3.  $3\text{RCOONH}_4(\text{aqueous}) + \text{GdCl}_3(\text{aqueous}) \rightarrow \text{Gd}(\text{RCOO})_3 + 3\text{NH}_4\text{Cl}$

First, we need to make  $\text{GdCl}_3$  solution from  $\text{Gd}_2\text{O}_3$  based on step 1. In step 2, 3,5,5-trimethylhexanoic acid (TMHA) is neutralized with ammonium hydroxide. In step 3, two aqueous solutions from steps 1 and 2 are mixed to produce Gd salt. When two solutions are mixed, white Gd-carboxylate compound (Gd-TMHA) precipitates immediately. These reactions are very sensitive to pH. Precipitated Gd-TMHA is thoroughly rinsed with 18 MΩ ultra pure water several times and then dried in vacuum desiccator. The final Gd-TMHA product is shown in Fig. 4.3. The yield of the synthesis is about 83%. On the other hand, if we purchase  $\text{GdCl}_3$  directly from vendor, we do not need step 1. But  $\text{Gd}_2\text{O}_3$  is much cheaper and we start from step 1.

To study molecular structure and chemical bonds in organic compounds, we use Fourier Transform Infrared (FT-IR) spectrum technique. We require three conditions for our final sample to make pure Gd-TMHA.

- No  $\text{OH}^-$  radical in FT-IR ( $3200 \sim 3500 \text{ cm}^{-1}$ ).
- No free acid peak ( $\sim 1700 \text{ cm}^{-1}$ ) in FT-IR.
- Presence of carboxylic peak ( $\sim 1420$  and  $1580 \text{ cm}^{-1}$ ).

Figure 4.4 shows various FT-IR spectra for the Gd-TMHA with different pH conditions in step 3. We can see that there are no  $\text{OH}^-$  radicals or free acid group left in pH = 6 case.

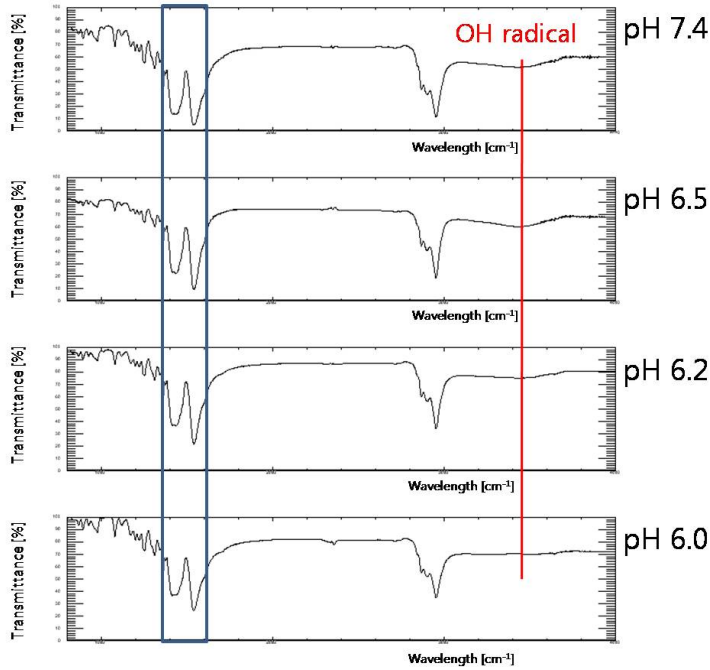


Figure 4.4: Various FT-IR spectra for Gd-TMHA salt made at different pH conditions in step 3). From top to bottom, values of pH in step 3 of the Gd-THMA synthesis are 7.4, 6.5, 6.2, and 6.0. The box shows where the carboxylic peaks are. The location of  $\text{OH}^-$  radical peak is also shown.

#### 4.2.6 Gamma Catcher

The purpose of  $\gamma$ -catcher is to contain gamma rays escaping from target region thereby providing correct energy measurement. The  $\gamma$ -catcher is a liquid scintillator, without Gd, enclosed in an acrylic vessel.

Figure 4.5 shows the scintillation yield of the non Gd-loaded, PC based scintillator as a function of MO concentration. The light yield of a sample is determined by measuring Compton edge from a  $^{137}\text{Cs}$  source. A scintillation yield of 80% with respect to pure PC is observed at a volume fraction of 60% MO. This figure shows how the light yield decreases for increasing dilution of the primary solvent by MO. The light transmittance of a scintillator with a solvent mixture of 60% MO and 40% PC with varying PPO concentration was measured with spectrophotometer.

#### 4.2.7 Buffer

To decrease the level of the accidental radioactive backgrounds, mainly coming from the PMT glass and surrounding rocks, non-scintillating oil is used to shield the scintillating layers from radioactive sources. Since the PMTs are immersed in a non-scintillating buffer, the buffer oil should have a good transmittance to the light coming from the scintillating layers. Also, the buffer oil should have a density similar to those of the target and the  $\gamma$ -catcher. MO and dodecane are possible candidates for the buffer oil.

Spectrophotometry has been used to measure optical transparency of MO. The transmittance of a collimated light beam through a sample in a 10-cm quartz cell is measured with a spectrometer. Figure 4.6 shows transmittance of MO with various viscosity values. At

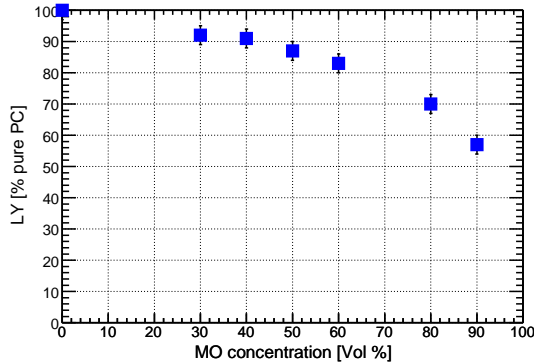


Figure 4.5: Scintillation light yield of PC and MO mixture based scintillator with varying mixture ratio with respect to that of 100% PC based scintillator. The PPO concentration is kept constant at 3 g/l.

wavelength above 400 nm the transmittance is flat without much differences among MOs with different kinetic viscosity values, whereas below 400 nm transmittance drops quickly with varying degrees depending on kinetic viscosity of solvent.

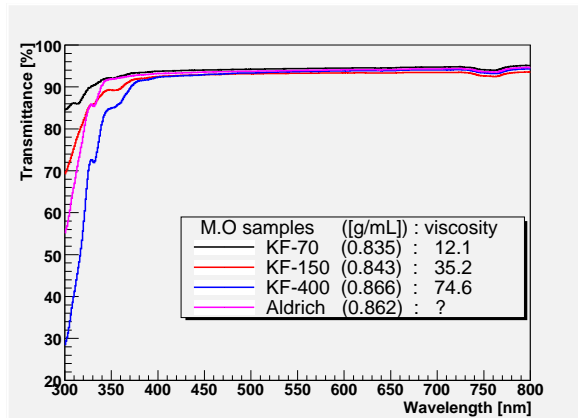


Figure 4.6: Transmittance of MO with different kinetic viscosity values. MO with low kinetic viscosity has better transmittance below  $\sim 400$  nm.

### 4.3 Fluor and Wavelength Shifter

The light yield was measured at different fluor concentrations from 1 to 10 g/l. Figure 4.7 shows the maximum light yield at PPO concentration about 3 g/l for both scintillators either with bis-MSB or POPOP as a wavelength shifter. At low PPO concentrations, the light output of the liquid scintillator is small. At concentrations above 3 g/l, the change in light output is very small. POPOP and bis-MSB are widely used as second wavelength shifter. Although the light yield is similar for the liquid scintillator with POPOP and the one with bis-MSB, it takes longer to dissolve POPOP in the solvent than bis-MSB. A second wavelength shifter is needed to change the wavelength of light from a fluor to about 410 nm, which is a sensitive region of bi-alkali type photocathode.

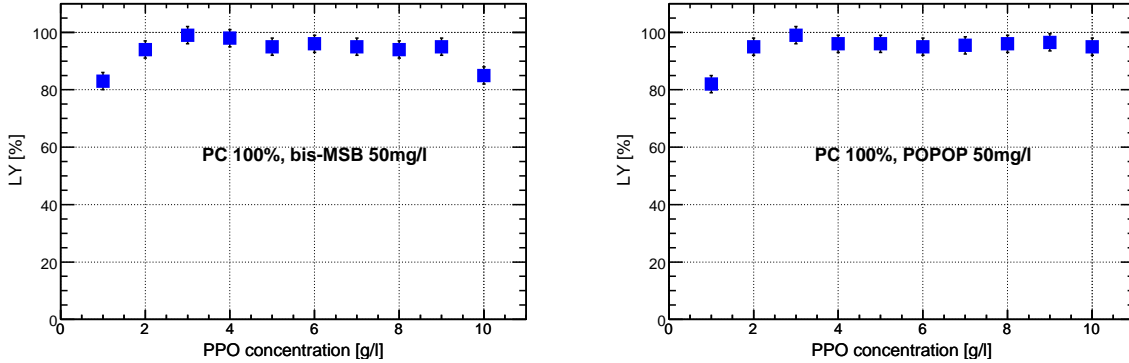


Figure 4.7: Relative light yield with different PPO concentrations in PC with respect to the light yield at 3 g/l PPO concentration. Bis-MSB (left) and POPOP (right) concentrations are both kept constant at 50 mg/l.

## 4.4 Long-term Stability

Besides the light yield, stability of the Gd loaded scintillator is another crucial matter. Gd-LS should be chemically stable for the duration of the experiment, *i.e.* several years. From Palo Verde and CHOOZ reactor experiments, unexpected problems with Gd-LS had been reported. Palo Verde had problems with precipitation, condensation, and slow deterioration of Gd-LS developing in time. In CHOOZ experiment, Gd-LS turned yellow a few months after deployment. A very rapid decay of attenuation length in Gd-LS had been measured [2].

Organic solvents can be oxidized in the presence of oxygen or water and develop coloration. This oxidation is accelerated by UV light and heat. Therefore, care should be taken to assure that moisture or humid air do not enter the sample. The liquid scintillators are flushed with nitrogen gas to purge oxygen and stored in air tight containers.

The long-term stability of the Gd-LS and liquid scintillator is investigated by means of spectrophotometric techniques. The transmittance is routinely measured in the wavelength range of  $300 \text{ nm} \leq \lambda \leq 800 \text{ nm}$ . The absorbance,  $A$ , is defined as

$$A = -\log_{10} \left( \frac{I}{I_o} \right), \quad (4.1)$$

where  $I_o$  and  $I$  are the intensities of the incident and the emerging lights, respectively. It is the absorbance that displays a simple dependence on the density and sample path length.

For extracting the attenuation length, Beer-Lambert-Bouguer law is used. It shows absorption of a beam of light as it travels through liquid for a distance  $L$ . The attenuation length,  $\lambda$ , at 420 nm is expressed as

$$\lambda = 0.4343 \left( \frac{L}{A_{420}} \right), \quad (4.2)$$

where  $L$  is path length in the sample and  $A_{420}$  is the absorbance at 420 nm. For a long term stability test, closed type cuvettes have been used to reduce oxygen contamination.

## 4.5 Material Compatibility

The target,  $\gamma$ -catcher, and buffer are in contact with acrylic vessels, so material compatibility of organic liquids with acrylic is crucial. Material compatibility tests for Gd-LS were performed.

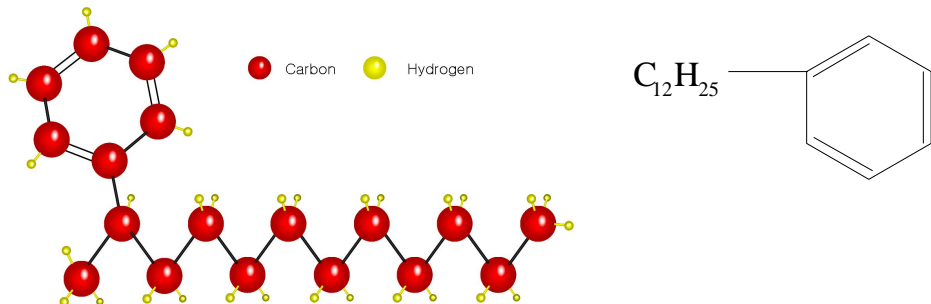


Figure 4.8: Molecular structure of LAB with a linear alkyl chain C<sub>12</sub>H<sub>25</sub>.

	PC	LAB
Molecular formula	C <sub>9</sub> H <sub>12</sub>	C <sub>n</sub> H <sub>2n+1</sub> -C <sub>6</sub> H <sub>5</sub> , n = 10 ~ 13
Molecular weight (g/mol)	120.19	233~237
Flash point (°C)	48	130
Density (g/ml)	0.89	0.86
Compatibility(acrylic)	Bad, need diluent	Good
Cost	Moderate	Low
Fluor dissolution	Very good	Moderate
Domestic availability	No	Yes
Toxicity	Toxic fume	Non toxic

Table 4.3: Comparison between PC and LAB.

The admixture of 40% PC and 60% MO by volume provides sufficient material compatibility and scintillation light yield. Material tests with other solvents also had been carried out. It was reported by Double Chooz collaboration that the Gd-CBX scintillator could react with steel [1]. Therefore, during the production of Gd-LS, any contact with steel surface will be avoided for the stability of Gd-LS.

## 4.6 R&D on LAB based Liquid Scintillator

### 4.6.1 Introduction

Recently, it has been brought attention of researchers to Linear Alkyl Benzene (LAB) as a possible solvent replacing PC and MO. LAB has been reported as having good light yield as well as desirable optical properties, *i.e.* high transmittance and large attenuation length. Unlike PC, it is non-toxic and bio-degradable. Also, it has a high flash point and, thus, can be handled safely. And it does not chemically interact with acrylic and stainless steel. It is commercially mass produced, cheap, and readily available.

As shown in Fig. 4.8, LAB (C<sub>n</sub>H<sub>2n+1</sub>-C<sub>6</sub>H<sub>5</sub>, n = 10 ~ 13) is composed of a linear alkyl chain of 10 ~ 13 carbon atoms attached to a benzene ring. Its density is 0.86 g/ml and is compatible to other organic liquids used for the experiment. Our current R&D is focused on a new liquid scintillator using LAB. Comparison of some chemical properties between LAB and PC is summarized in Table 4.3. LAB can be obtained domestically in Korea from ISu Chemical Ltd [6].

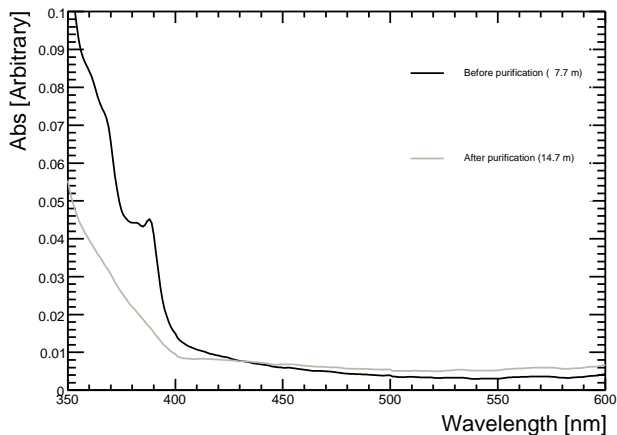


Figure 4.9: Absorption spectra of a LAB sample before and after purification by  $\text{Al}_2\text{O}_3$  column separation. Absorbance is measured using Jasco UV/VIS 530 spectrometer. Two curves have different baseline values.

#### 4.6.2 Purification of LAB

Purification of liquid scintillator is performed to remove chemical impurities as well as particulates containing radioactive isotopes. It enhances light transmittance and long term stability of liquid scintillator. Various purification methods were investigated by neutrino experiments; adsorption by activated  $\text{Al}_2\text{O}_3$  or silica gel, water extraction, vacuum distillation, and filtration by a particulate filter. Adsorption method has many advantages. Specific separation can be done based on high selectivity of adsorbents. A large amount of liquid can be continuously purified. Drawbacks include need for periodic replacement of adsorbent and slow purification speed for high viscosity liquids.

LAB was purified by adsorption by passing LAB through a column of activated  $\text{Al}_2\text{O}_3$ . Unpurified LAB samples obtained from ISu Chemical Ltd have an attenuation length  $7 \sim 10$  m at 420 nm, depending on production batches. These samples were delivered in 200 l steel drums. The absorbance of purified LAB started to decrease after passing LAB five times the volume of  $\text{Al}_2\text{O}_3$  used through the column. Therefore, we replaced  $\text{Al}_2\text{O}_3$  in the column with fresh one for each volume of LAB five times that of  $\text{Al}_2\text{O}_3$  used.

Figure 4.9 shows UV-visible spectra of LAB before and after  $\text{Al}_2\text{O}_3$  purification. The attenuation lengths at 420 nm calculated from absorption data before and after purification are  $7.7 \pm 0.3$  m and  $14.7 \pm 0.3$  m, respectively. This shows that  $\text{Al}_2\text{O}_3$  purification method could be used to improve optical properties of LAB.

ISu Chemical Ltd. kindly provided a high quality LAB sample obtained from the upstream in their production line specially for this test. This sample was handled with care and delivered in very clean plastic containers. First, we measured its attenuation length without any purification. The result showed that the attenuation length is greater than 20 m. Based on this, we decided that purification with  $\text{Al}_2\text{O}_3$  is not necessary to improve the attenuation length. Then we tried filtration on the sample with a Teflon membrane filter with  $0.2 \mu\text{m}$  pore size, but it also did not improve the attenuation length. From these results, it is evident that a high quality LAB does not need to go through purification processes to improve the attenuation length. Table 4.4 lists the attenuation lengths for several LAB samples.

Conditions	Attenuation Length (m) at 420 nm
Steel drum, unpurified	7 ~ 10
Steel drum, purified by Al <sub>2</sub> O <sub>3</sub>	15
Best quality, unpurified	> 20
Best quality, filtered	> 20

Table 4.4: The attenuation lengths of four LAB samples provided by ISu Chemical Ltd. in different conditions.

n	Composition (%)
10	7.17
11	27.63
12	34.97
13	30.23

Table 4.5: LAB composition measured with GC-MS method. Molecular formula of LAB is C<sub>n</sub>H<sub>2n+1</sub>-C<sub>6</sub>H<sub>5</sub>, n = 10 ~ 13.

#### 4.6.3 LAB Composition Measurement with GC-MS

To reduce the systematic uncertainty between near detector and far detectors at RENO experiment, it is important to know the exact composition of LAB. The composition of a LAB sample was measured by Gas Chromatography with Mass Spectrometry (GC-MS) at Korea Basic Science Institute [7]. The results are shown in Table 4.5 and Fig. 4.10. Based on this measurement, we can calculate the number of protons and H/C ratio of the sample. The sample has a H/C ratio of 1.66. Table 4.6 shows the proton densities of PC, PXE, dodecane, and LAB.

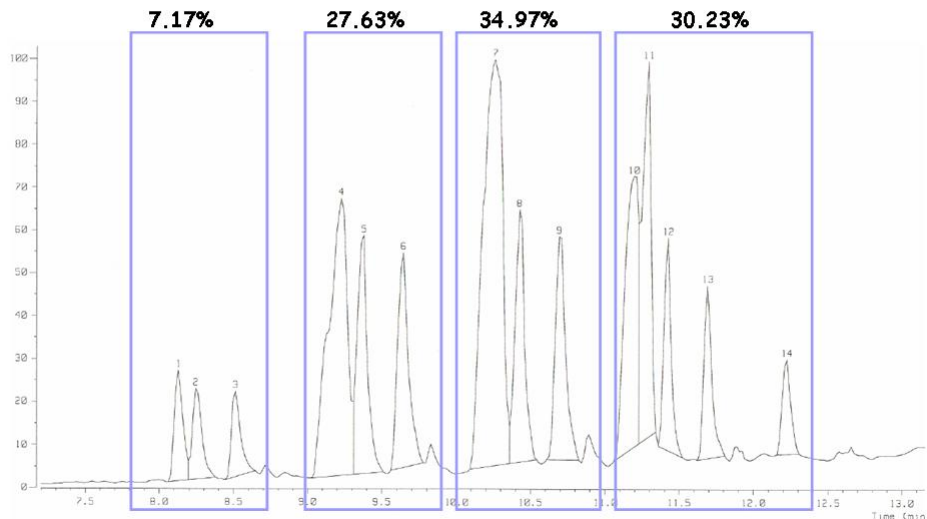


Figure 4.10: LAB components identified with GC-MS. This LAB sample consists of four main components; C<sub>16</sub>H<sub>26</sub>, C<sub>17</sub>H<sub>28</sub>, C<sub>18</sub>H<sub>30</sub>, and C<sub>19</sub>H<sub>32</sub>.

Solvent	Proton Density (/m <sup>3</sup> )
LAB( $C_nH_{2n+1}-C_6H_5$ , $n = 10 \sim 13$ )	$0.631 \times 10^{29}$
PC( $C_9H_{12}$ )	$0.530 \times 10^{29}$
PXE( $C_{16}H_{18}$ )	$0.512 \times 10^{29}$
Dodecane( $C_{12}H_{26}$ )	$0.694 \times 10^{29}$

Table 4.6: Numbers of hydrogen atoms per m<sup>3</sup> of various solvents for liquid scintillators. The composition of LAB is given in Table 4.5.

#### 4.6.4 Optical Properties

The acrylic that target and  $\gamma$ -catcher vessels are made of becomes opaque rapidly for light with wavelength below 400 nm. And the PMTs being used (R7081, Hamamatsu) is most sensitive to light at  $\sim 390$  nm but retains good sensitivity at  $400 \sim 430$  nm. Therefore, it is imperative for the liquid scintillator emitting light at  $\sim 420$  nm.

The optical and scintillation properties of the pure LAB solvent and of LAB-fluor mixture have been investigated by UV/VIS spectrometry. The emission spectra of LAB, PPO, and bis-MSB are shown in Fig. 4.11. The pure LAB solvent shows an emission maximum at 340 nm. Therefore, the wavelength of the scintillation light from LAB needs to be shifted above 400 nm. This is achieved by using PPO as a primary solute and bis-MSB as a secondary wavelength shifter. As shown in Fig. 4.11, PPO and bis-MSB emit photons at  $340 \sim 440$  nm and  $380 \sim 460$  nm, respectively.

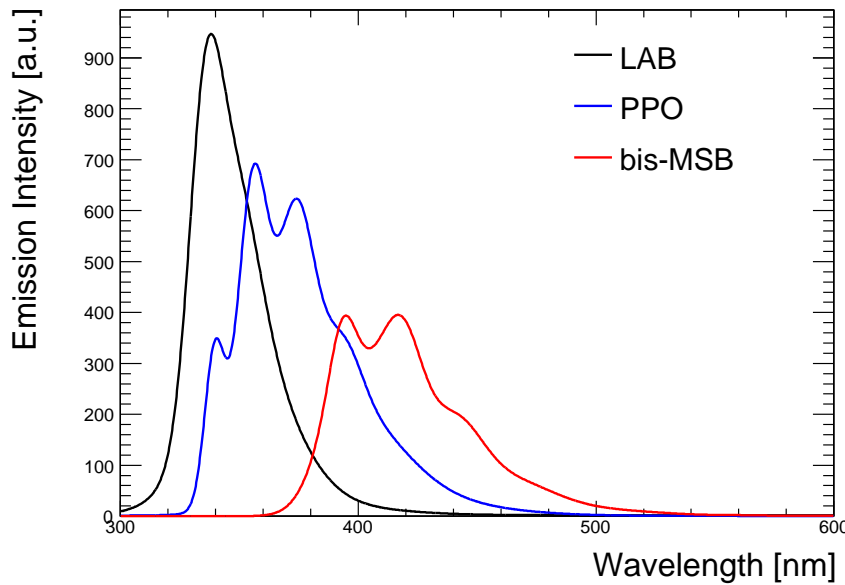


Figure 4.11: Emission spectra of the solvent LAB (black), the primary fluor PPO (blue), and the wavelength shifter bis-MSB (red).

The LAB based liquid scintillator has 3 g/l PPO and 30 mg/l bis-MSB dissolved in LAB. The attenuation lengths of the LAB based scintillator and its individual components are shown in Fig. 4.12. The sample's attenuation lengths were measured using a JASCO V530 UV/VIS spectrophotometer with a sample in 10-cm quartz cuvettes. The attenuation length of LAB

was measured to be 25.2 m at 420 nm. The attenuation length of the liquid scintillator has been measured to be 7.1 m at 420 nm. Based on the comparison of the attenuation lengths of LAB and LAB based liquid scintillator, it is evident that the absorption of photons with wavelength shorter than 420 nm is mostly by fluor.

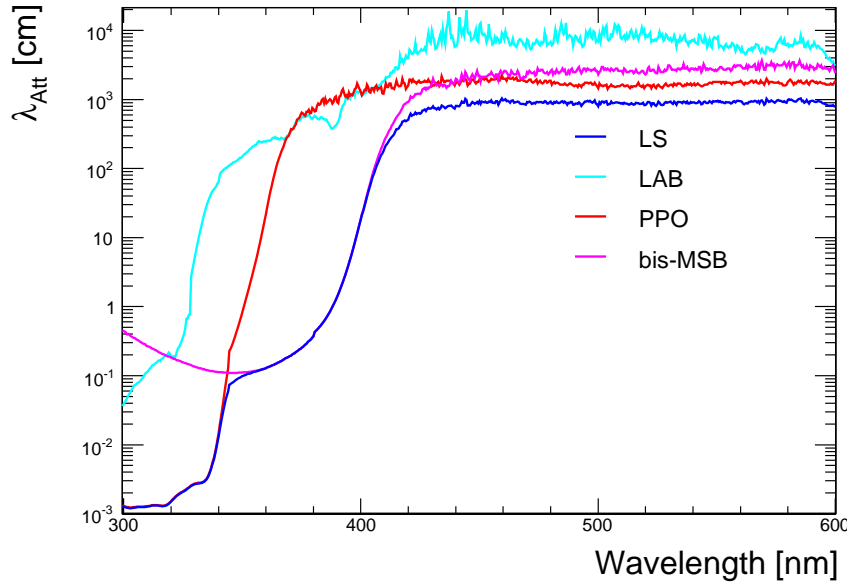


Figure 4.12: Attenuation lengths of the LAB based LS with 3 g/l PPO and 30 mg/l of bis-MSB (black), LAB (light blue), 3 g/l PPO (red), and 30 mg/l bis-MSB (light purple). Cyclohexane was used as the solvents when measuring PPO and bis-MSB attenuation lengths.

Below the wavelength  $\sim 340$  nm, photons are absorbed mostly by PPO and  $340 \sim 400$  nm by bis-MSB. PPO and bis-MSB molecules absorb a photon emitted by LAB and themselves and emit longer wavelength photons. A reemitted photon has random direction with respect to the absorbed photon. This absorption-reemission process could occur multiple times until either the photon escapes the scintillator volume or its wavelength falls in a region where PPO and bis-MSB absorption probability is negligible. Since the absorption probability of PPO and bis-MSB is much higher for the shorter wavelength photons than for the longer ones, successive absorption and reemission result in progressive red-shift of the spectrum (Fig. 4.13). The small attenuation length of liquid scintillator below 400 nm indicates that most of the absorption and reemission processes happen close to the location of the initial scintillation process.

The light yield is given as the number of optical photons emitted per one MeV deposited in the scintillator. A gamma ray source of  $^{137}\text{Cs}$  is used to measure the light yield of a scintillator in a dark box with 5-inch PMT (H6527, Hamamatsu). Liquid scintillator is filled in an 1-liter Teflon bottle. A GEANT based simulation shows the 1-liter Teflon bottle is too small for a gamma to deposit all of its energy. Thus Compton edge at 0.477 MeV from scattering of photons from  $^{137}\text{Cs}$  is used as a reference in the light yield measurement instead. After considering the PMT quantum efficiency and coverage of the PMT cathode, light yield of the our sample scintillator was measured to be 10 000 optical photons per MeV. Figure 4.14 shows comparison of data with the simulation result in which 10 000 optical photons per MeV was used as the input to the simulation.

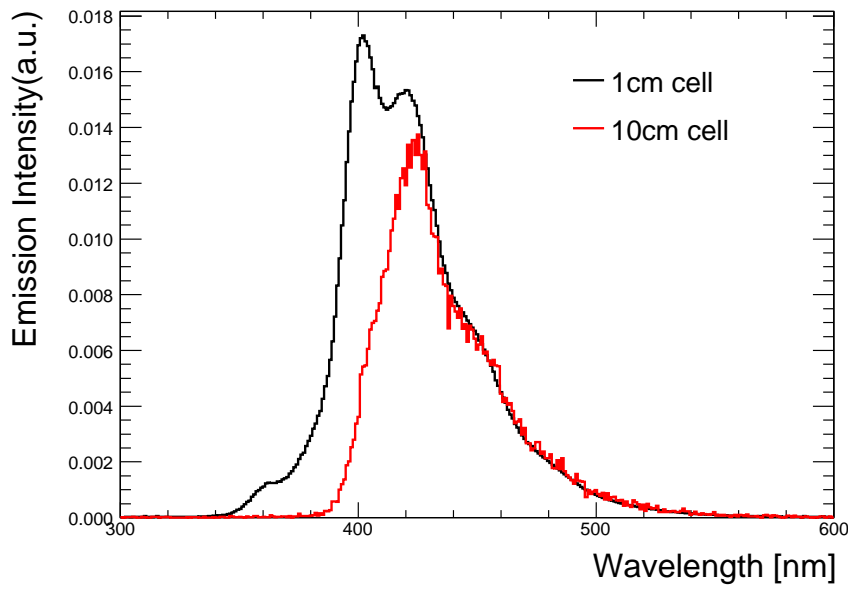


Figure 4.13: Fluorescent spectra of LS measured using 1 cm (black) and 10 cm (red) sample cells. The spectrum shapes are alike above  $\sim 430$  nm but quite different below, where absorption by bis-MSB is dominant. This indicates the short wavelength photon escaping scintillation volume before fully red-shifted through absorption-reemission process.

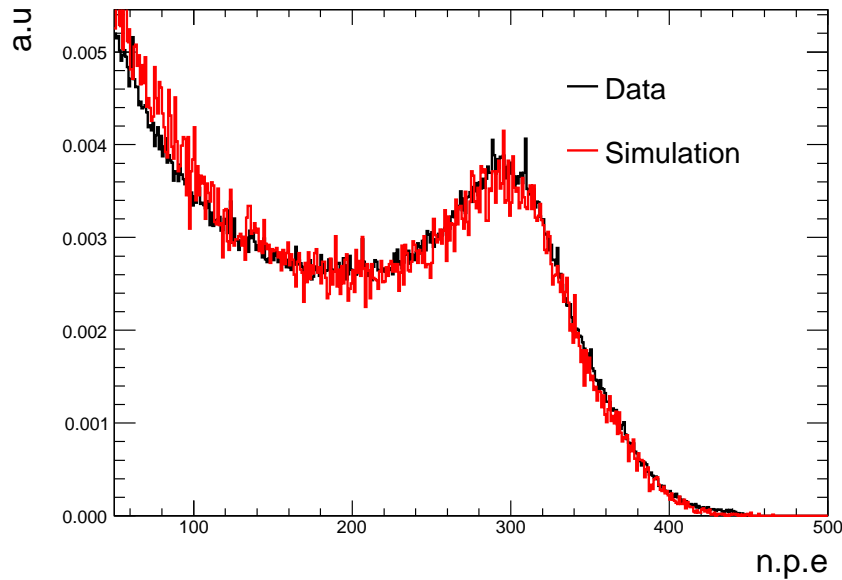


Figure 4.14: The number of photoelectrons distribution of  $^{137}\text{Cs}$  measured with the light yield measurement setup. Data is shown in black and simulation in red. The light yield value used for the simulation is 10 000/MeV.



Figure 4.15: EDTA, Xylenol orange indicator, and buffer solution. Microburette with bang pattern and lateral stopcock are used for titration.

#### 4.6.5 Titration of Gd Concentration

To measure the Gd concentration, a titration method was tested. We prepared Xylenol orange indicator, buffer solution, and EDTA (Ethylene Diamine Tetra Acetic acid). At pH>5, EDTA reacts with Gd until Gd is depleted in the Gd loaded solvent. But when more EDTA is added into solution, EDTA then reacts with the indicator and color of the solvent changes from violet to yellow as shown in Fig. 4.15. We can calculate the concentration of Gd from the following equilibrium equation,

$$V_{EDTA} \times C_{EDTA} = V_{sample} \times C_{sample}, \quad (4.3)$$

where  $V_{EDTA}$  is the volume of EDTA,  $C_{EDTA}$  is the concentration of EDTA (mol),  $V_{sample}$  is the volume of the sample, and  $C_{sample}$  is the concentration of Gd in the sample to be measured.

## 4.7 Radiopurity

The main radioactive sources of low energy gamma rays are  $^{238}\text{U}$ ,  $^{232}\text{Th}$ , and  $^{40}\text{K}$ . Double Chooz and Daya Bay experiments require the concentrations of each of these radioactive impurities in liquid scintillator to be less than  $10^{-13}$  g/g. An acceptable single event rate due to such radioactivity in the detector is estimated by Monte Carlo simulations. This is described in Sect. 6.6.4.

The radioactivities were measured by Inductively Coupled Plasma Mass Spectrometry (ICP-MS). ICP-MS is the simplest and fastest method but it cannot differentiate  $^{40}\text{K}$  from  $^{40}\text{Ar}$  because they have similar masses. In addition to ICP-MS, independent measurements of radioactivity are also available; High Resolution ICP-MS, Neutron Activation Analysis (NAA), and High Purity Germanium detector (HPGe).

Gammas and electrons from radioactive isotopes in the detector materials together with a neutron-like signal within a given time window can make an uncorrelated background. Assuming  $10^{-13}$  g/g of  $^{238}\text{U}$ ,  $^{232}\text{Th}$ , and  $^{40}\text{K}$  in the  $\gamma$ -catcher and target, we obtain 0.7 Hz of the single event rate using GEANT4 based simulation. This rate is quite smaller than the single event rate due to radioactivity of the PMT glass.

## 4.8 Liquid Handling and Purification System

The liquid system consists of three sets of liquid storage tanks, pumps, and  $0.05\ \mu\text{m}$  filters, each for target,  $\gamma$ -catcher, and buffer, as shown in Fig. 4.16. The speed of filling the detector with liquids should be carefully controlled to keep the equal liquid levels in target,  $\gamma$ -catcher, and buffer so as to avoid any stresses on acrylic vessels. The amount of liquid is measured by mass flow meters. Nitrogen purging is done during the liquid filling.

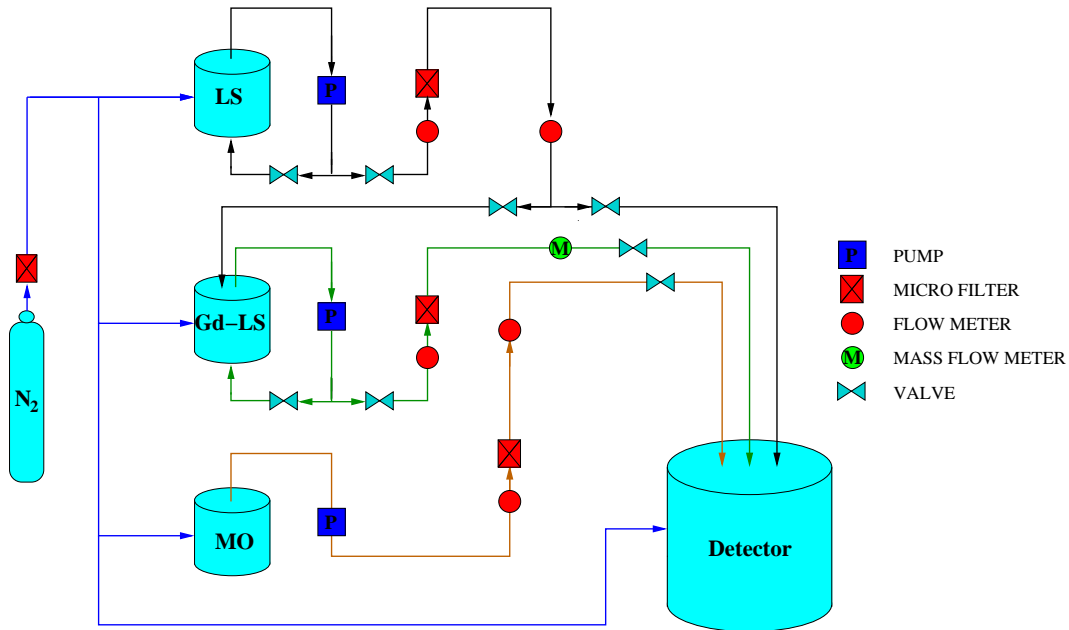


Figure 4.16: Schematic view of liquid handling and purification system.

# Bibliography

- [1] F. Ardellier *et al.* (2006), [hep-ex/0606025](#).
- [2] M. Apollonio *et al.*, Eur. Phys. J. C **27**, 331 (2003).
- [3] F. Boehm *et al.*, Phys. Rev. **D64**, 112001 (20010).
- [4] Yayun Ding *et al.*, Nucl. Instrum. Meth. A584, 238 (2008).
- [5] X. Guo *et al.*, (2007), [hep-ex/0701029](#).
- [6] <http://www.isuchemical.co.kr>
- [7] <http://www.kbsi.re.kr>
- [8] <http://www.rndkorea.co.kr>
- [9] <http://www.sial.co.kr>

# Chapter 5

# Front-End Electronics, DAQ, Trigger, and Slow Control

## 5.1 Front-End Electronics

The antineutrino interaction in the RENO detector produces scintillation lights, and a part of them are converted into photoelectrons at the PMT. To detect the antineutrino event, the RENO detector has 354 inner PMTs and 67 outer PMTs. A RENO readout system is designed to record the charge and arrival time of PMT hits. Based on the energy and timing information we can select the neutrino events, reject background events, and reconstruct the vertex of antineutrino interaction. The near and far detectors are designed to have the same PMT configuration and readout system.

The RENO DAQ employs a new electronics developed for Super-Kamiokande experiment which uses charge-to-time conversion chips to record hits at 60 kHz with no dead time. The following section describes the descriptions of the RENO DAQ electronics.

### 5.1.1 Specification of RENO Electronics

The readout electronics system records the charge and arrival time of PMT hits to measure the energy and reconstruct the neutrino interaction. Characteristics of RENO electronics are summarized below.

- PMT gain:  $\sim 10^7$
- Time window:  $\sim 300$  ns
- Dynamic range of PMT signals:  $1 \sim 1000$  photoelectrons
- Time resolution of each PMT signals:  $1 \sim 1.5$  ns
- Data size:  $\leq 200$  kbyte/s for each detector
- No electronic deadtime
- Time resolution between  $e^+$  signal and neutron-like signal :  $\sim 10$  ns

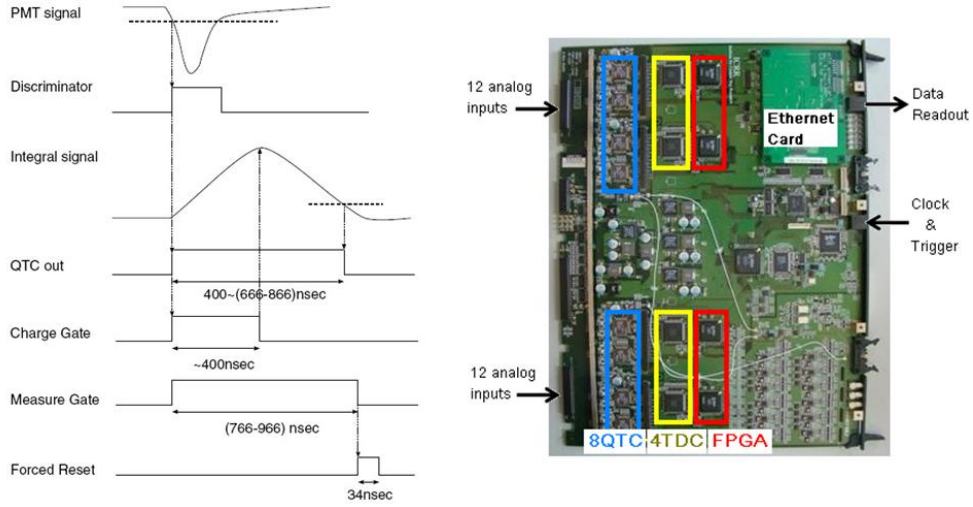


Figure 5.1: Operation logic diagram of QTC chip and QBEE board

### 5.1.2 QBEE Board

The QBEE board is a charge-to-time conversion chip (QTC) based electronics with an onboard ethernet card, developed for Super-Kamiokande experiment and used since Sept. 2008. The new electronics system are fast enough to record every PMT hits and are guaranteed for stable data acquisition over ten years. Each QBEE board has an 100 Mbps ethernet card, which is fast enough to transfer every hit information to online computer without any loss. The hit information is stored in the online storage and then software triggers are applied.

The PMT pulse generated by a photon hit is fed to a QTC chip. The QTC chip measures the hit time and charge of the PMT pulse and convert them into a form that can be easily read and stored by the TDCs. The output of the QTC chip is a logic pulse with its leading edge marking the hit arrival time and width representing the integrated charge of the PMT pulse. The characteristics of the QTC chip are summarized in Table 5.1.

The operation logic diagram of QTC chip is shown in Fig. 5.1. The QTC chip integrates charge of a PMT pulse fed to the chip and outputs a pulse with a width proportional to the integrated charge. The QTC chip produces two gates for its charge integration operation, one for charging the capacitor (charge gate) in the QTC chip and the other for discharging the capacitor for measuring the charge in the capacitor (measure gate). If an incoming PMT pulse exceeds a current threshold, the 400 ns wide charge gate and 966 ns wide measure gate are generated. Therefore, the width of output pulse from a QTC chip is between 400 and 966 ns which is proportional to the size of the integrated charge. A reset signal of 34 ns is generated after the measure gate. So the processing time of a QTC chip is 1  $\mu$ s per cycle. The output pulse from the QTC is fed into a multi-hit TDC where the timing information of all leading and trailing edges are recorded.

A QTC chip receives three analog inputs and processes each input with one of three gains of 1, 7, and 49. The charge resolution is about 0.1 pC and the dynamic range is 0.2 to 2500 pC. The timing resolution is 0.3 ns for one photoelectron and 0.2 ns for more than five photoelectrons.

A QBEE board accommodates eight QTC and four TDC chips to process 24 analog inputs. The QBEE board receives an external clock of 60 MHz and a periodical trigger signal of 60 kHz from a master clock. The 60 kHz periodical trigger signal initializes TDC and comes with a

Dynamic range	$0 \sim 2500 \text{ pC}$
Self trigger	Built-in discriminator
Number of input channels	3
Processing speed	$\sim 500 \text{ ns/cycle}$
Gain	1/7/49 (3 settings)
Charge resolution	0.05 p.e. ( $< 25 \text{ p.e.}$ )
(Non-) Linearity (Q)	$< 1\%$
Timing resolution	0.3 ns (1 p.e. = $-3 \text{ mV}$ ), 0.2 ns( $> 5 \text{ p.e.}$ )
Power dissipation	$< 200 \text{ mW/channel}$

Table 5.1: Characteristics of QTC chips. p.e. is photoelectron.

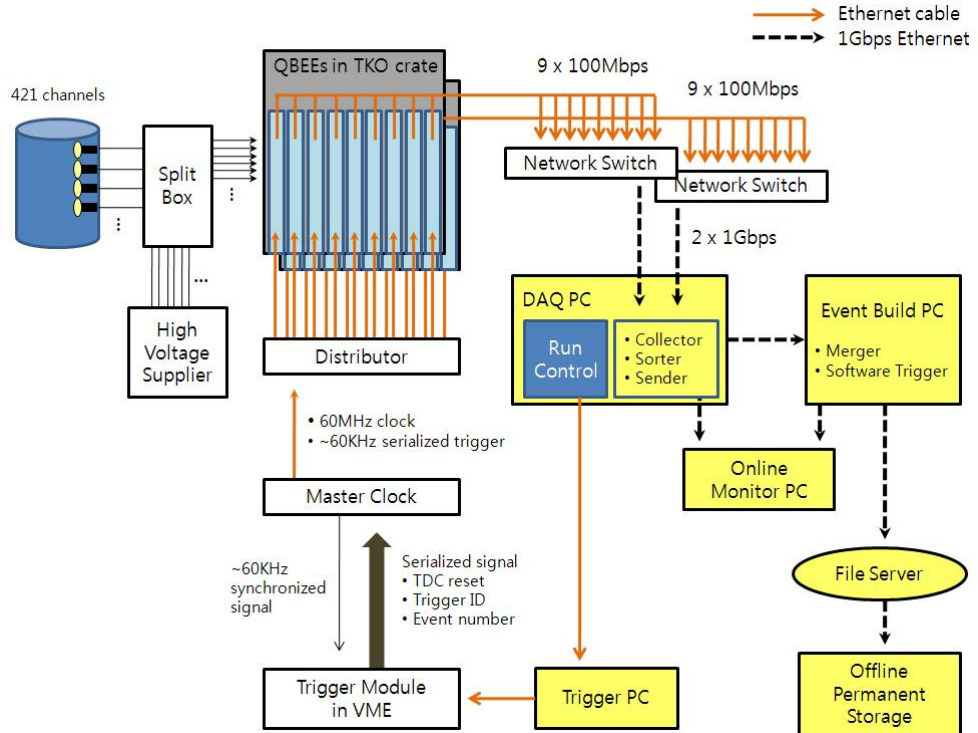


Figure 5.2: Diagram of DAQ system for RENO. There are 18 QBEE boards in two TKO crates collecting the hit signals from 421 PMTs (354 PMTs in inner detector and 67 PMTs in veto). The near and far detectors have the same DAQ architecture.

timing tag and an event number, which are used to identify the PMT hits in the same trigger. After collecting all the hits, an event is built and selected by software triggers. The adjustable QTC parameters for RENO are 1) the threshold level for a single photoelectron signal, 2) the length of charge gate and measure gate.

## 5.2 DAQ

The RENO data acquisition consists of data readout using front-end electronics, event builder, software triggers, data logger and run control. A schematic diagram of the RENO DAQ system is shown in Fig. 5.2 and Fig. 5.3.

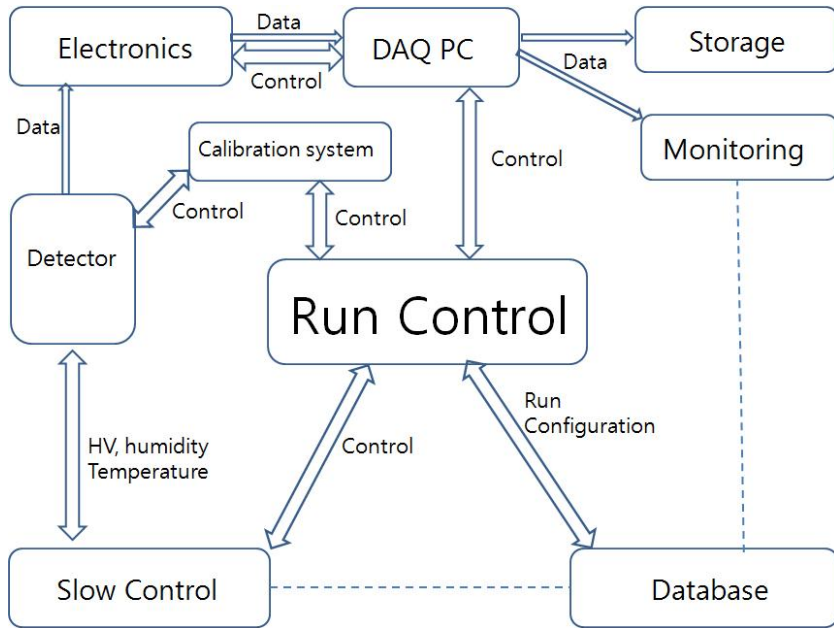


Figure 5.3: Flow diagram of run control for RENO. The run control sends commands to DAQ components and makes run conditions. Shift crew will use integrated GUI.

### 5.2.1 Data Readout and Run Control

The front-end electronics for data readout are based on QBEE boards in the TKO crate and ethernet cards on QBEE. A QBEE board receives 24 analog PMT inputs, digitizes them, and sends the signal outputs to the online computer through an 100 Mbps ethernet card. RENO uses 18 QBEE boards for 421 channels per detector, and data throughput rate is about 1.8 Gbps per detector. The near and far detectors have the same DAQ architecture.

The run control sends command to DAQ components and makes run conditions. Shift crew will use an integrated GUI, which can be used to select run mode, trigger type, and detector parameter. The possible run modes are data taking and calibration. The trigger type can be one of predefined trigger sets. The detector parameters are high voltage setting for PMTs.

### 5.2.2 Event Builder

All the QBEE boards are driven by a common 60 MHz master clock (MCLK). A 60 kHz periodical trigger and a serialized 32-bit event number are generated by a trigger module, and fanned out via a distributor to all the QBEE boards through network cables. All the hit data are sorted and merged according to the trigger event number and the timing information.

A periodic trigger of 60 kHz makes a data block of hits. The order of the data blocks is made according to the event number. The hits in a data block are sorted by their hit time and merged. The hit data in the same block are merged, sorted by hit time, and stored with an event number. An event builder constructs events by applying software trigger to the merged hit data. The merged data before the software trigger are stored 2 to 3 days and will be used for monitoring purposes.

### 5.2.3 Software Trigger

The software triggers are applied to the events constructed by the merger for identifying neutrino candidate events, cosmic muon events, or calibration events. The software trigger calculates the total number of hits (multiplicity) within a certain time window and constructs event if the hit sum exceeds a certain threshold number. The first hit time in an event is set to  $T_0$ , and time windows before and after  $T_0$  determine an event gate by software triggers. All of PMT hits within this event gate makes an event with “in gate event” flag and the hits are set with “in gate hit” flag. In analyzing data hits with “in gate hit” flag will be used. Some of QBEE bits are assigned for calibration trigger ID. If there is even a hit with those bits, a calibration trigger is generated. The software trigger rates are monitored in the online, and those events with “in gate event” flag are stored in the long-term storage.

## 5.3 Trigger

The triggering strategy at RENO is to record all the hits having signal over a given threshold, and then to select events by software triggers. The software triggers make decisions for neutrino-like events, cosmic ray muon events, background events, and calibration events.

### 5.3.1 Energy Threshold

The signature of a neutrino interaction in the RENO detector is a prompt signal from a positron with a minimum energy of 1.022 MeV followed by a delayed signal from a neutron. About 90% of the neutrons are captured on Gadolinium at the target of the RENO detector, yielding an  $\sim 8$  MeV gamma cascade with a capture time of  $\sim 30 \mu\text{s}$ . The main backgrounds to the signal in the antineutrino detectors are fast neutrons produced by cosmic muon interactions in the rock,  $^8\text{He}/^9\text{Li}$ , which are also produced by cosmic muons and accidental coincidences between natural radioactivity and neutrons produced by cosmic muons. Dominant backgrounds to the delayed event are related to cosmic muons.

The energy threshold should be set for the software trigger to accept both the prompt positron signal above 1.022 MeV and the delayed neutron capture event with a photon cascade of 8 MeV with a very high efficiency. This requirement for energy threshold expects the DAQ system to record all prompt positron signals produced from the antineutrino interactions and to make a complete energy spectrum analysis to be possible for increasing the sensitivity of  $\sin^2(2\theta_{13})$ . Furthermore, it requires the DAQ to register uncorrelated background events due to either PMT dark noise or low energy radioactivity for a detailed background analysis in the offline.

### 5.3.2 Event Building

After calculating the global time of hits, all the recorded hits are sorted and merged according to the timing information, and then software triggers are applied to select an event.

### 5.3.3 Online Software Trigger

There are two groups of triggers, one is for selecting neutrino events and the other is for calibration and monitoring backgrounds.

- neutrino triggers: energy sum trigger and multiplicity trigger.
- calibration triggers: LED, laser, and radioactive sources.

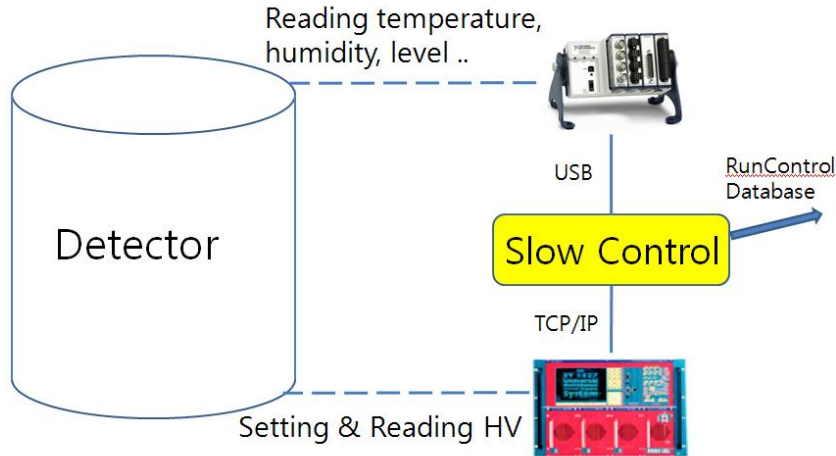


Figure 5.4: Diagram of slow control. The slow control system monitors detector conditions and controls PMT HV power supplies.

- random triggers: pedestal run and random background.
- cosmic trigger: cosmic ray muons.

## 5.4 Slow Control and Monitoring

An online monitoring computer located in the control room reads data from the DAQ host computer via network. It provides event display, online history histograms to monitor detector performance, and variety of additional tasks needed to efficiently monitor detector performance parameters and diagnose troubles of detector and DAQ system. The slow control monitors the status of the HV systems, the temperatures of the electronics crates and detectors, the fluids levels, and humidity. And the slow control is able to set up high voltage for each channel and turn on and off HV remotely. The slow control scheme is shown in Fig. 5.4. The data collected by the slow control system are sent to online monitoring system and database.

# Chapter 6

# Monte Carlo Simulation

## 6.1 Overview

As with other particle experiments, extensive studies using Monte Carlo simulation have been performed for RENO experiment. The Monte Carlo (MC) studies provide valuable guidance to optimize and determine various design parameters of the detector. The most cost effective design without much compromising the sensitivity of the experiment is attempted based on the studies using MC simulation. The MC simulation also helps the development of analysis tools to be used for the actual data from the experiment. In addition, some of systematic uncertainties can be estimated from simulation studies as well.

The RENO detector simulation is modified from `GLG4SIM`, a GEANT4 based program for liquid scintillator neutrino detectors. The “generic” program has been customized for the RENO detector with a new event generator which provides better physics models. More details on the simulation can be found later in this chapter.

Studies on backgrounds is also performed using MC simulations. Major background sources are cosmic muon induced events and radioactivities from the surrounding rocks and detector itself. The rates of these background events have been independently estimated and appropriate event generators have been added to the main simulation program so that we can obtain realistic results from the MC simulations.

This chapter describes the generation of inverse beta decay (IBD) events, calculations of the detector performance, and the background simulations. It also includes the description of the systematic uncertainties estimated from MC studies.

## 6.2 Event Generation

This section describes the event generator of inverse beta decay for reactor neutrinos.

### 6.2.1 Inverse Beta Decay Events

In reactor based neutrino experiments, the neutrino detection is made via the inverse beta decay (IBD) process that an incoming neutrino interacts with a free proton in the detector material, that is,

$$\bar{\nu}_e + p \rightarrow n + e^+. \quad (6.1)$$

In the event generator, the four-momenta are specified for all four particles involved in the IBD process. The energy dependence of anti-neutrino’s cross section and the observed spectra of reactor neutrinos are shown in Fig. 6.1.

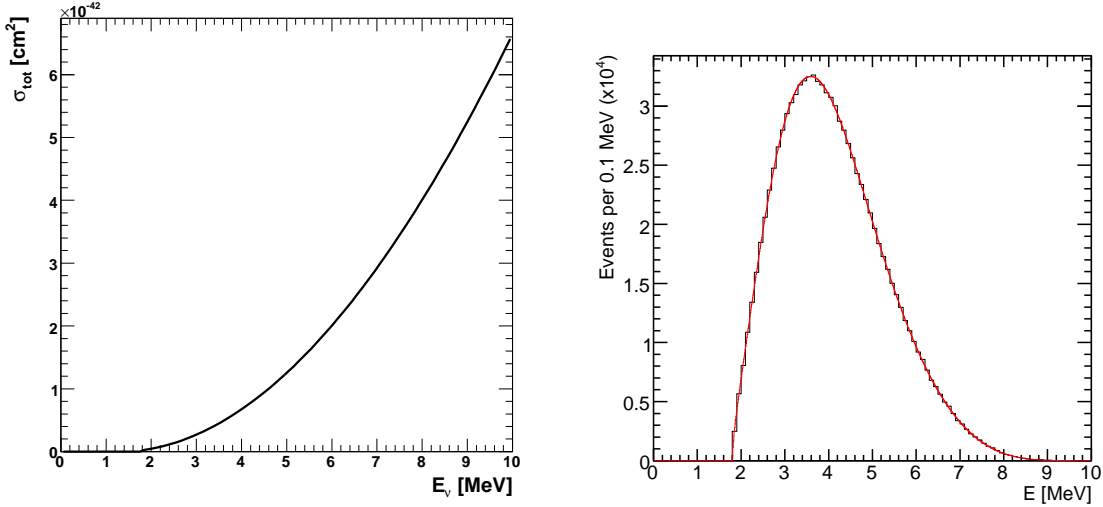


Figure 6.1: Energy dependence of anti-neutrino cross section (left) and observed spectrum of reactor neutrinos (right). In the observed spectrum, a theoretically calculated spectrum is shown as a red curve compared with that of the MC simulation shown as a black histogram.

The cross sections for quasi-elastic neutrino scattering on proton at energies greater than 1 GeV have been calculated by Llewellyn-Smith [1]. Vogel and Beacom [2] presented a simple and precise description of neutrino–nucleon scattering at a low energy region of a few MeV, relevant to reactor, solar, and supernova neutrinos.

The IBD event generator includes Vogel and Beacom cross section [2] and the total cross section at the first order in  $1/M$  is defined by

$$\sigma_{tot}^{(1)} = \sigma_0 \left( \alpha_1 + \beta_1 \frac{\Delta}{M} + \gamma_1 \frac{E_e^{(0)}}{M} \right) E_e^{(0)} E_e^{(0)}, \quad (6.2)$$

where  $E_e^{(0)} = E_\nu - \Delta$ ,  $\Delta = (M_n - M_p)$ , and  $M$  is the nucleon mass. The parameters in Eq. 6.2 are  $\alpha_1 = f^2 + 3g^2$ ,  $\beta_1 = -2(f + f_2)g - 2f^2 - 8g^2$ , and  $\gamma_1 = -4(f + f_2)g - 2f^2 - 10g^2$ , where  $f = 1$ ,  $f_2 = 3.706$ , and  $g = 1.26$ . The normalization constant  $\sigma_0$  is given as

$$\sigma_0 = \frac{G_F^2 \cos^2 \Theta_c}{\pi} (1 + \Delta_{inner}^R), \quad (6.3)$$

where  $G_F$  is the Fermi coupling constant,  $\Theta_c$  is the Cabibbo angle, and  $\Delta_{inner}^R \simeq 0.024$ . In the laboratory frame the threshold energy is  $E_\nu^{thr} = ((M_n - M_e)^2 - M_p^2)/2M_p = 1.806$  MeV as shown in Fig. 6.1. We calculated the neutrino spectrum at the detector using the total cross section weighted by the neutrino flux from the Yonggwang nuclear power plant, Korea.

### 6.2.2 Kinematics for Positron and Neutron

The event generator gives the energy and scattering angle distributions of a positron and a neutron coming from an IBD event. The generator is based on Vogel and Beacom's IBD differential cross section calculations [2]. The angular distribution of the positron is almost uniform as shown in Fig. 6.2. Unlike the positron from the IBD process, the neutron recoiling from the IBD process has a strong angular correlation with respect to the incoming neutrino

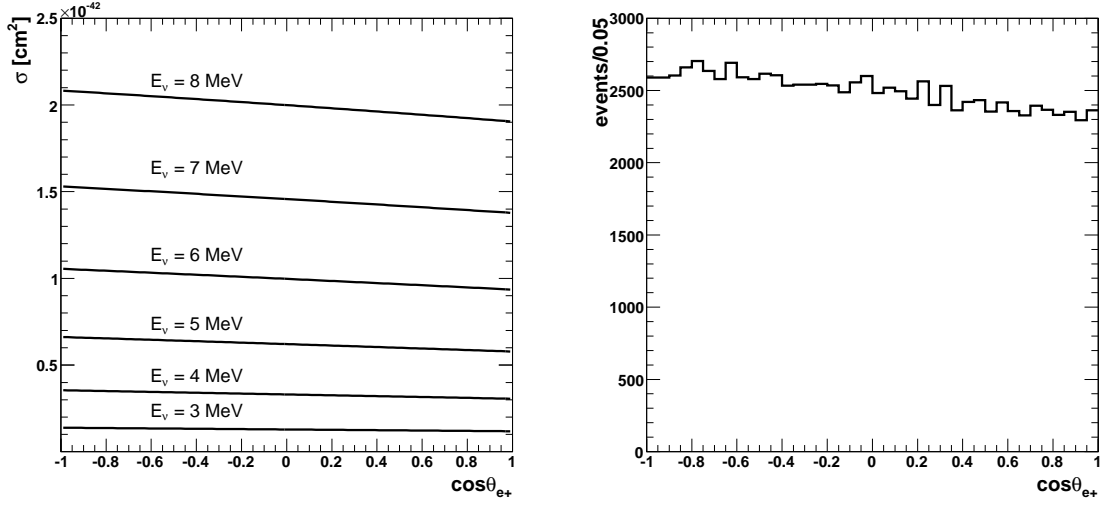


Figure 6.2: Differential cross section as a function of the angle between the positron direction and the incident neutrino direction for several neutrino energy values (left). Angular distribution of the positron from the IBD event generator (right).

direction. Since the proton is at rest in the laboratory frame, the neutron is essentially emitted in the forward directions with the maximum angle  $\theta_n^{\max}$ :

$$\cos(\theta_n^{\max}) = \frac{\sqrt{(2E_\nu\Delta - (\Delta^2 - m_e^2))}}{E_\nu}. \quad (6.4)$$

Figure 6.3 shows the differential cross section of IBD process as a function of the angle between the recoiling neutron direction and the incident neutrino direction for various incident neutrino energies. Also the angular distribution of the neutron with respect to the incident neutrino direction is shown. The kinetic energy of the neutron is given by

$$T_n = \frac{E_\nu E_e^{(0)}}{M} (1 - v_e^{(0)} \cos \theta_{e+}) + \frac{y^2}{M}, \quad (6.5)$$

where  $y^2 = (\Delta^2 - m_e^2)/2$  and  $v_e = p_e/E_e$ .

The kinetic energy spectrum of the positron from IBD process is given by

$$\frac{d\sigma}{dT_{e+}} = \frac{K}{ft} \left( \frac{T_e}{m} + 1 \right) \left[ \left( \frac{T_e}{m} + 1 \right)^2 - 1 \right]^{1/2} \rho(T_e - \Delta), \quad (6.6)$$

where  $\Delta = M_n - M_p + m = 1.804$  MeV,  $ft = 1087$  s,  $T_e$  is the kinetic energy of the positron,  $K = 2.63 \times 10^{-41}$  cm<sup>2</sup>·s, and  $\rho$  is the energy spectrum of the incident  $\bar{\nu}_e$  [3]. The kinetic energy spectra of the positron and the neutron are shown in Fig. 6.4.

### 6.2.3 Neutrino Flux

When fissile isotopes undergo fission, neutrinos are emitted isotropically. There are four dominant fissile isotopes in the nuclear fuel cycle; <sup>235</sup>U, <sup>238</sup>U, <sup>239</sup>Pu, and <sup>241</sup>Pu. On the average six neutrinos are emitted per fission with their energy peaked at around 1 MeV [4]. But only

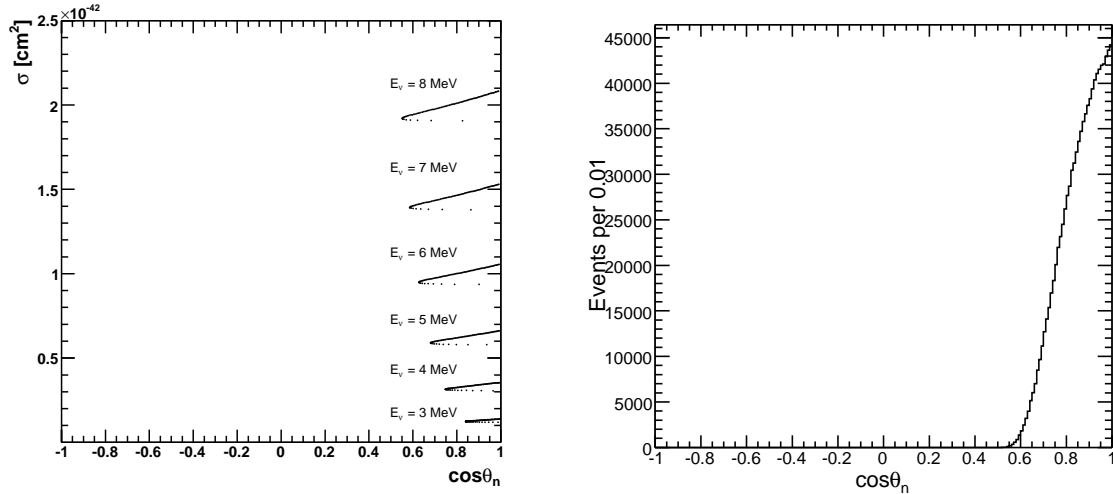


Figure 6.3: Cross section versus the cosine of neutron angles for several neutrino energies (left) and neutron angular distribution (right) from the IBD process.

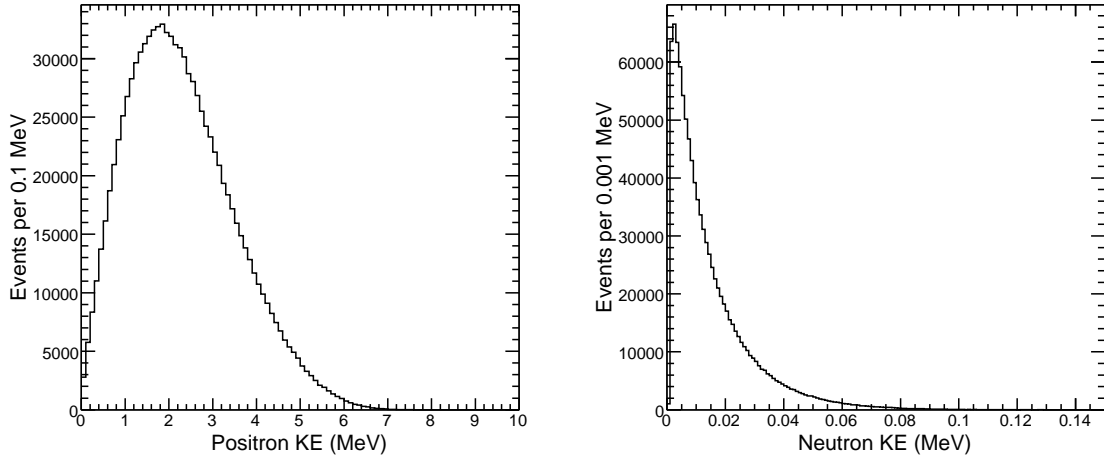


Figure 6.4: Positron kinetic energy spectrum (left) and neutron kinetic energy spectrum (right) from the IBD event generator.

neutrinos with energies above the threshold of 1.806 MeV contribute to the inverse beta decay. The mean energy and the number of neutrinos above  $E_\nu = 1.8 \text{ MeV}$  released from the fission of these isotopes are shown in Table 6.1.

The neutrino energy spectra from fission processes are parametrized in Refs. [7, 8] using

$$\frac{dN_\nu^{(j)}}{dE_\nu} = \exp \left( \sum_{i=0}^5 a_i^{(j)} E_\nu^i \right), \quad (6.7)$$

where  $a_i^{(j)}$  are the fit parameters for the  $j$ th isotope and  $E_\nu$  is a neutrino energy in MeV. The results are shown in Table 6.2 and Fig. 6.5.

Isotope	$N_\nu (> 1.8 \text{ MeV})$	$E_f (\text{MeV})$
$^{235}\text{U}$	$1.92(1 \pm 0.019)$	$201.7 \pm 0.6$
$^{238}\text{U}$	$2.38(1 \pm 0.020)$	$205.0 \pm 0.9$
$^{239}\text{Pu}$	$1.45(1 \pm 0.021)$	$210.0 \pm 0.9$
$^{241}\text{Pu}$	$1.83(1 \pm 0.019)$	$212.4 \pm 1.0$

Table 6.1: The total number of  $\bar{\nu}_e$  per fission above 1.8 MeV and energy released per fission from Ref. [9].

Parameter	$^{235}\text{U}$	$^{238}\text{U}^{(*)}$	$^{239}\text{Pu}$	$^{241}\text{Pu}$
$a_0$	3.519	0.976	2.560	1.487
$a_1$	$-3.517$	$-0.162$	$-2.654$	$-1.038$
$a_2$	1.595	$-0.790 \times 10^{-1}$	1.256	$4.130 \times 10^{-1}$
$a_3$	$-4.171 \times 10^{-1}$	—	$-3.617 \times 10^{-1}$	$-1.423 \times 10^{-1}$
$a_4$	$5.004 \times 10^{-2}$	—	$4.547 \times 10^{-2}$	$1.866 \times 10^{-2}$
$a_5$	$-2.303 \times 10^{-3}$	—	$-2.143 \times 10^{-3}$	$-9.229 \times 10^{-4}$

Table 6.2: Parameters of the polynomial of order of 5 for the neutrino flux from dominant isotopes in nuclear fuel. Parameters for isotopes  $^{235}\text{U}$ ,  $^{239}\text{Pu}$ , and  $^{241}\text{Pu}$  are from Ref. [7] and  $^{238}\text{U}$  from Ref. [8]. The resulting distributions are shown in Fig. 6.5.

The fission rate in a reactor with a power  $P_{th}$  is

$$n_{fis} = \frac{P_{th}}{\sum_i f_i \bar{E}_{fi}}, \quad (6.8)$$

where  $f_i$  and  $\bar{E}_{fi}$  are the fission fraction in the nuclear fuel and the mean energy released per fission of isotope  $i$  given in Table 6.1, respectively, and  $P_{th}$  is the reactor power. Then the number of fissions per second is related to the reactor power by  $(6.24 \times 10^{18}) \cdot n_{fis}$ , where  $P_{th}$  is given in Watts and  $E_{fi}$  in eV in calculating  $n_{fis}$  in Eq. 6.8.

The number of neutrinos with energy between  $E_{\min}$  and  $E_{\max}$  from the fission process of the  $i$ th isotope is

$$N_\nu = n_{fis} \cdot \sum_i f_i \int_{E_{\min}}^{E_{\max}} \frac{dN_\nu^{(i)}}{dE_\nu} dE_\nu \quad (6.9)$$

The neutrino flux is isotropic about the source and the neutrino flux at distance  $r$  is

$$n_\nu(r) = \frac{1}{4\pi r^2} N_\nu. \quad (6.10)$$

### 6.3 Detector Simulation

A major goal of the detector simulation, besides being used as a data analysis tool, is to optimize the detector design in the early stage of the experiment. To achieve the sensitivity goal of  $\sin^2(2\theta_{13}) > 0.02$  within the budget and time constraints, the detector design needs to be carefully studied and optimized.

The RENO detector is designed to have four concentric cylindrical modules, two active inner modules called target and  $\gamma$ -catcher and two inert outer modules called buffer and veto as shown in Fig. 6.6. Compared to the past reactor neutrino experiments, an additional active layer,  $\gamma$ -catcher, is added to the detector design, surrounding the target, to contain gamma

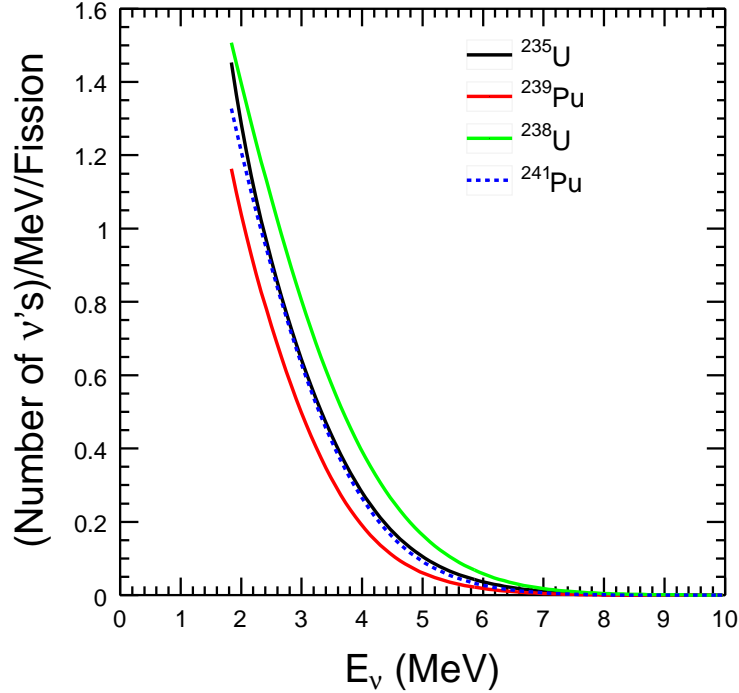


Figure 6.5: Neutrino flux of four main isotopes in the nuclear fuel using parametrization in Table 6.2 given in Refs. [7, 8].

rays escaping from target. There are 354 and 67 10-inch PMTs mounted on the buffer vessel wall and veto wall, respectively, pointing inward normal to the wall surfaces.

The geometrical parameters of the detector modules and the number of PMTs are determined based on the MC simulation studies as shown later in this chapter.

### 6.3.1 Software Tools

The primary software tool for modelling the RENO detector response is GLG4SIM, a GEANT4-based simulation package for liquid scintillator detectors derived from KLG4SIM of KamLAND collaboration. This software is designed for simulation of the detailed detector response to particles moving through and interacting with a large volume of liquid scintillator detector.

#### GEANT4 Simulation

The RENO detector has four concentric cylindrical sub-detectors each filled with Gd-loaded liquid scintillator, liquid scintillator without Gd, mineral oil, and water, respectively. The GEANT4 toolkits are used for simulating the physics processes involving particles with energies above a few keV propagating through the materials in the sub-detectors. However, the optical photon production and propagation through liquid scintillator, including processes like absorption, re-emission, and elastic collisions, are handled by specifically written codes in GLG4SIM.

In the detector simulation, the liquid scintillator consists of LAB for the organic solvent,

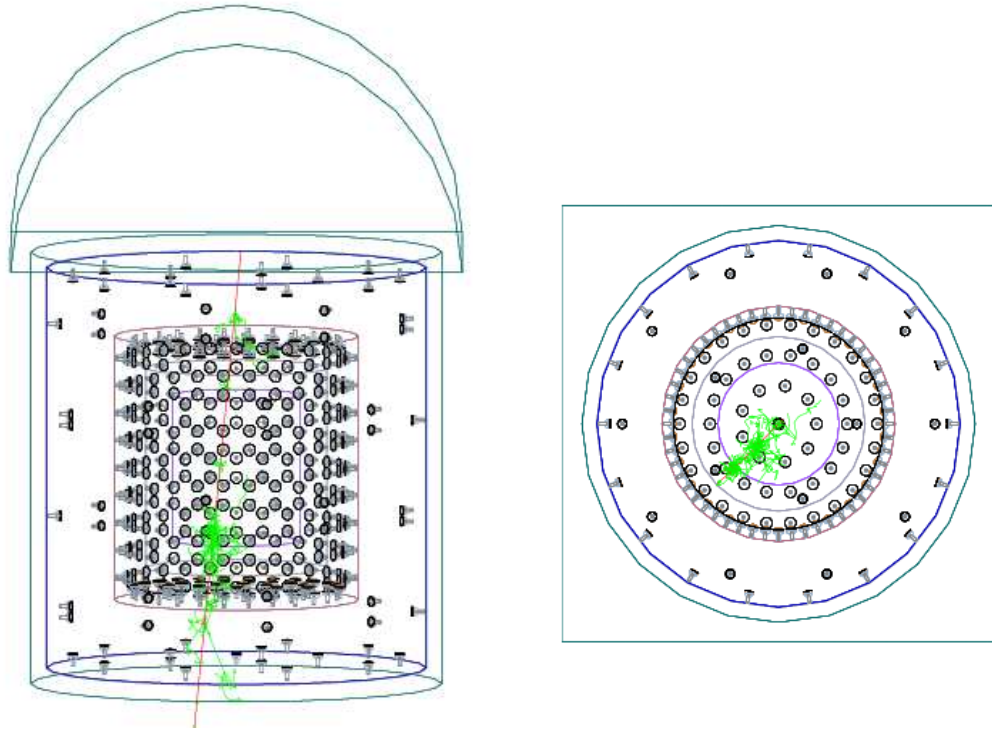


Figure 6.6: Side and top view of the RENO detector simulation with a muon (red line) passing through the target and leaving showers (green lines).

1.5 g/l of PPO as a fluor, and 0.3 mg/l of Bis-MSB as a secondary wavelength shifter. In the target region, 0.1% Gadolinium (Gd) is loaded. GEANT4 Neutron Data Library (NDL) version 3.8 gives a reasonable approximation for the continuum gamma spectrum after neutron capture on Gd. However, the discrete lines of high-energy gammas are not included in the NDL version 3.8. Fortunately, an update is available for GLG4SIM for an additional Gd support for a proper modelling of discrete lines of high energy gamma. The resulting distributions of the neutron capture distance and capture time are shown in Fig. 6.7.

GLG4SIM uses a custom written simulation code for PMT with detailed PMT geometries. This PMT simulation handles transmission, absorption, and reflection of optical photons at the photocathode. The PMT modelling includes a finite photocathode thickness and a wavelength dependent photocathode efficiency supplied by the PMT manufacturer.

### 6.3.2 Optical Photon Processes

Each photon generated in the simulation is tracked in the detector until it either reaches a PMT or is lost. The simulation accounts for several light propagation phenomena while tracking the photons. In the scintillator, photons can undergo absorption or elastic scattering (Rayleigh scattering) by solvent and fluor molecules.

Attenuation length,  $\lambda_{att}$ , of the liquid scintillator is defined as

$$\frac{1}{\lambda_{att}} = \frac{1}{\lambda_{scat}} + \frac{1}{\lambda_{abs}}, \quad (6.11)$$

where  $\lambda_{scatt}$  and  $\lambda_{abs}$  are the scattering length and the absorption length, respectively. The reciprocal value of the liquid scintillator attenuation length,  $1/\lambda_{att}^{LS}$ , is equal to the sum of those

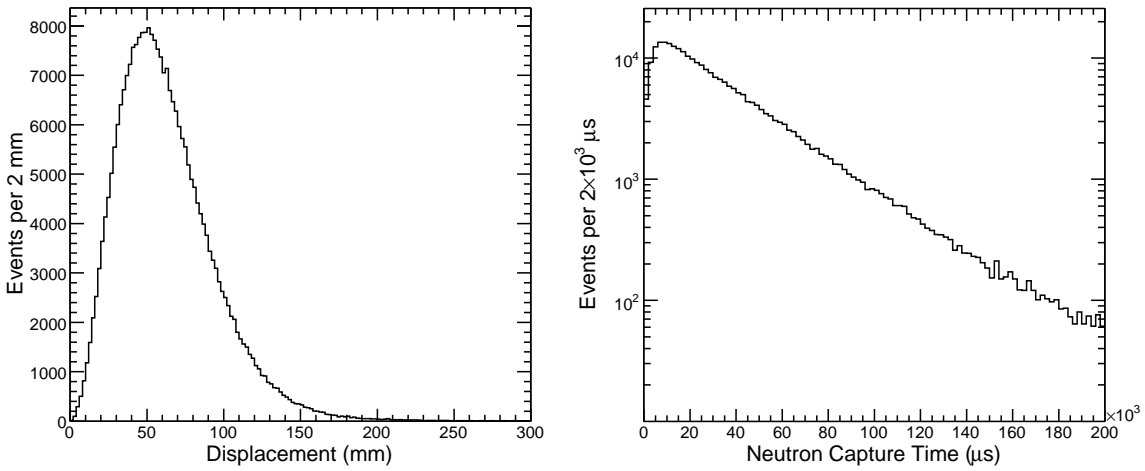


Figure 6.7: Neutron capture distance from inverse beta decay events (left) and neutron capture time (right).

of scattering lengths and absorption lengths,

$$\frac{1}{\lambda_{att}^{LS}} = \frac{1}{\lambda_{scat}^{LS}} + \frac{1}{\lambda_{abs}^{LS}} = \frac{1}{\lambda_{scat}^{LS}} + \frac{1}{\lambda_{abs}^{solvent}} + \frac{1}{\lambda_{abs}^{fluors}}. \quad (6.12)$$

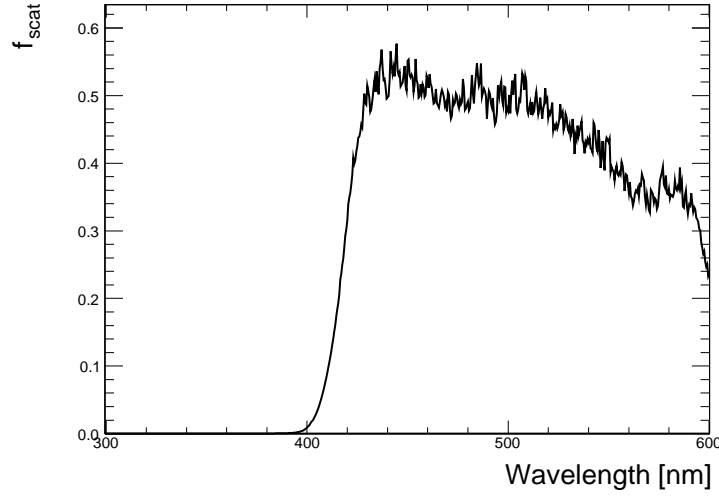


Figure 6.8: Measured scattering fraction of the LAB based liquid scintillator.

In the simulation photons can be either scattered or absorbed by the solvent and fluors according to appropriate fractions. Because a large fraction of liquid scintillator is the solvent, photons are scattered mostly by LAB. It has to be noted that the band gap for the lowest-energy electronic transitions in the LAB molecules is at 320 nm, and thus the absorption by LAB below 320 nm is strong. At wavelengths longer than 320 nm the absorbance by LAB drops rapidly and the measured extinction coefficient roughly obeys a  $\lambda^{-4}$  dependence, as

expected in Rayleigh scattering. The scattering fraction,  $f_{scatt}$ , can be obtained from

$$f_{scatt} = \frac{\lambda_{att}^{LS}}{\lambda_{scatt}^{LAB}}. \quad (6.13)$$

Figure 6.8 shows the measured scattering fraction of an optical photon in the liquid scintillator. If a photon undergoes elastic scattering, its wavelength remains unchanged but its direction is altered. The direction of a photon after elastic scattering has an  $(1 + \cos^2 \theta)$  dependence, where  $\theta$  is the photon scattering angle. Absorption of a photon by fluors can be followed by their re-emission, but there is a chance for an absorbing molecule undergoing non-radiative relaxation process depending on its quantum yield efficiency. The non-radiative relaxation results in the loss of the photon, and tracking in the simulation is terminated in that case. The absorption probability of LAB, PPO, and bis-MSB can be calculated by

$$P_{abs}^i = \frac{\lambda_{abs}^{LS}}{\lambda_{abs}^i}, \quad (6.14)$$

where  $i$  represents LAB, PPO, or bis-MSB. Figure 6.9 shows the measured absorption probability for each component in the liquid scintillator. Re-emission occurs isotropically and a longer wavelength than that of the absorbed photon, based on the emission spectrum, is assigned to the re-emitted photon.

The absorption of photons within the acrylic medium (vessel walls) is simulated according to the absorption probability calculated with medium's attenuation length. Also, the reflection and refraction of photons at the surface of the acrylic vessel are simulated using the Fresnel's law. The refractive indices of all dielectric materials in the detector are measured at different wavelengths and implemented in the simulation. Figure 6.10 shows the measured refractive indices of some of detector materials. After a photon enters a PMT and is absorbed by the photocathode, tracking is terminated, and a hit is made depending on the quantum efficiency of the photocathode.

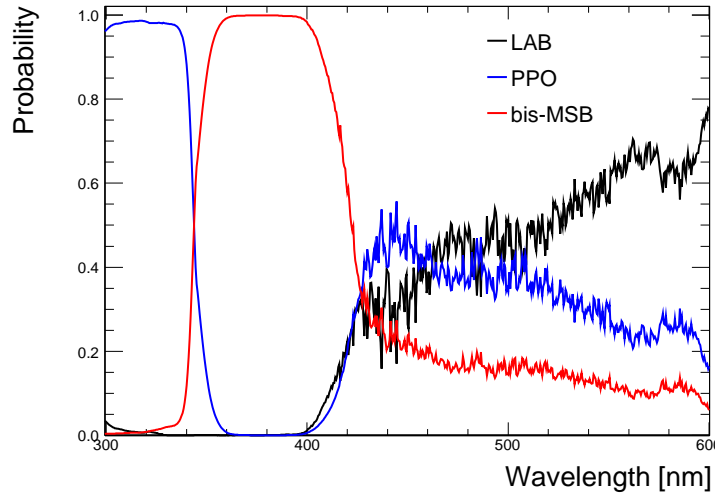


Figure 6.9: Measured absorption probabilities of LAB, PPO, and bis-MSB. These are used in the detector simulation.

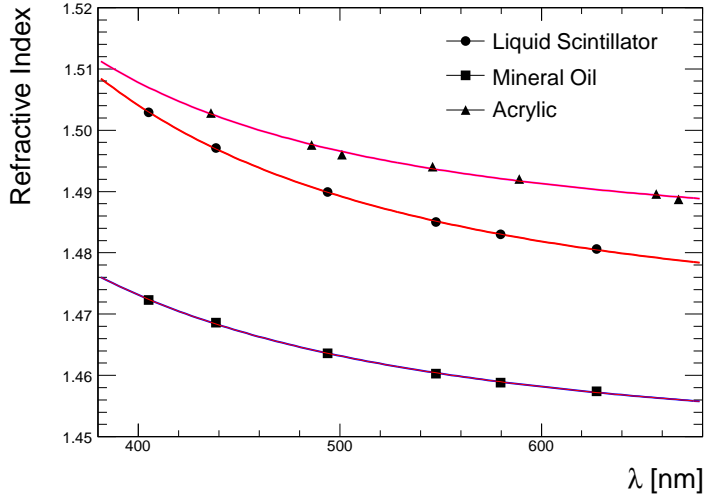


Figure 6.10: Measured refractive indices of liquid scintillator, mineral oil, and acrylic.

### 6.3.3 Event Reconstruction

#### Vertex Reconstruction

For vertex reconstruction, two independent algorithms, “charge weighting method” and “likelihood method,” have been used. The charge weighting method is simple and fast, and is suitable for the online event display or as a filter to extract interesting events to apply more sophisticated event selection criteria. The likelihood method has a better vertex position resolution than the charge weighting method but requires more CPU time and therefore to be used as an offline reconstruction method.

The event vertex in the charge weighting method is calculated as

$$\vec{r}_{vtx} = \frac{\sum_{i=PMT} n_i \vec{r}_i}{\sum_{i=PMT} n_i}, \quad (6.15)$$

where  $n_i$  is the number of photoelectrons on the  $i$ th PMT and  $\vec{r}_i$  is the vector pointing from the center of the detector to the  $i$ th PMT. The number of photoelectrons is calculated by  $n_i = c_i q_i$ , where  $q_i$  and  $c_i$  are the amount of charge measured on the  $i$ th PMT and the charge-to-number of photoelectron conversion factor on that PMT. Because the reconstructed vertex position calculated with the charge weighting method is inherently closer to the center of the detector than the actual vertex position, linear corrections are applied based on the detector simulation. The position resolution is found to be  $\sim 38$  cm for a 1 MeV gamma ray as shown in Fig. 6.11 and improves for a higher energy gamma.

The likelihood method uses not only the number of scillation photons detected by PMTs but also the arrival time of those photons. The expected number of photoelectrons on the  $i$ th PMT can be written as

$$\nu_i = N_{tot} \frac{A_i \cdot f(\cos \theta_i)}{4\pi R_i^2} \epsilon_i \cdot \prod_j e^{-R_{ij}/\lambda_j}, \quad (6.16)$$

where  $N_{tot}$  is the total number of optical photons generated,  $A_i$  and  $\epsilon_i$  are the frontal area of the cathode and quantum efficiency of the PMT, respectively,  $R_{ij}$  is the distance from the

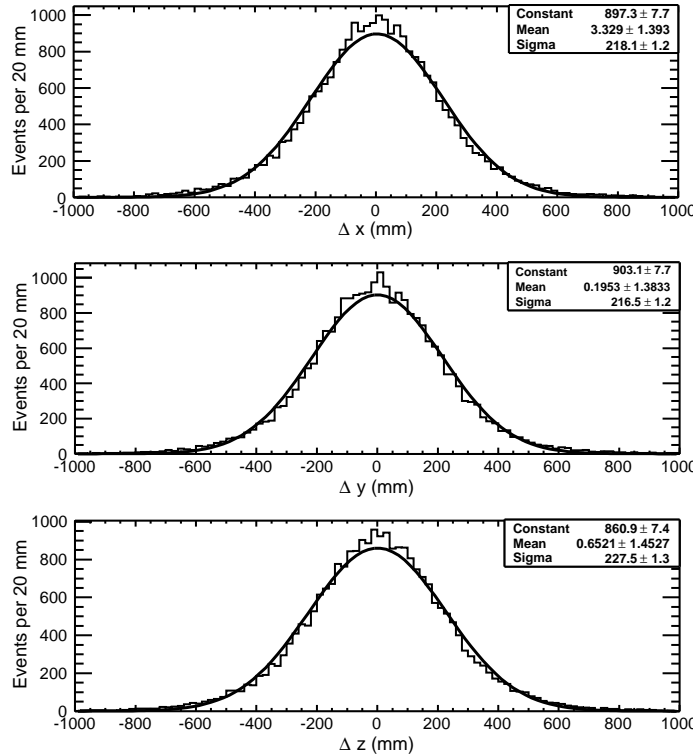


Figure 6.11: Difference between reconstructed and the generated vertex positions for an 1 MeV  $\gamma$  rays in random direction in the target using a simple weighting method.

vertex to the PMT in medium  $j$ , and  $\lambda_j$  is the attenuation length of the  $j^{\text{th}}$  medium in between the vertex and the PMT. The effective area of photocathode of the PMT seen from the incident angle  $\theta_i$  is accounted for in function  $f(\cos \theta_i)$ .

The likelihood is then written as

$$\mathcal{L} = \prod_{i=\text{PMT}} \mathcal{G}(n_i; \vec{r}; \nu_i, \sigma_i) \cdot \mathcal{T}(t_i; n_i, R_i), \quad (6.17)$$

where  $\mathcal{G}(n_i; \nu_i, \sigma_i)$  is the Gaussian probability with its mean of  $\nu_i$  and width of  $\sigma_i$ , and  $\mathcal{T}(t_i; n_i, R_i)$  is the probability of having the first hit of  $n_i$  hitting the  $i^{\text{th}}$  PMT to have the hit time of  $t_i$ . The number of observed photoelectrons,  $n_i$ , is calculated from the charge output from PMT using the charge-to-photoelectron conversion factor from calibrations. The negative log likelihood is then minimized using MINUIT to find the vertex position and the total number of optical photons created.

## Energy Reconstruction

Energy is calculated from the number of reconstructed optical photons. Since the PMT coverage depends on the position of event vertex, the reconstructed energy is dependent on the vertex position. This is naturally incorporated in the expected number of photoelectrons in Eq. 6.16. Energy can be written as  $E = \xi N_{\text{tot}}$  where  $\xi$  is a constant determined from simulation and source calibration.

The energy reconstruction has a good linearity and has the resolution of  $\frac{\delta E}{E} = \frac{0.065}{\sqrt{E}} \oplus 0.012$ , where  $E$  is given in MeV. Figure 6.12 shows the reconstructed energy distribution for an 1 MeV

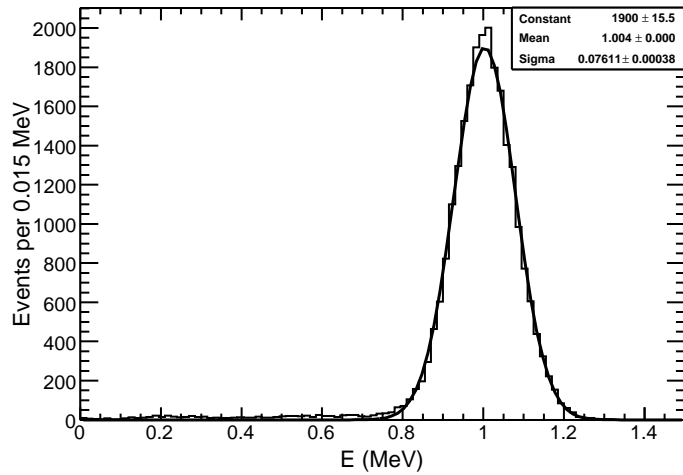


Figure 6.12: Reconstructed energy distribution of an 1 MeV  $\gamma$  in the target.

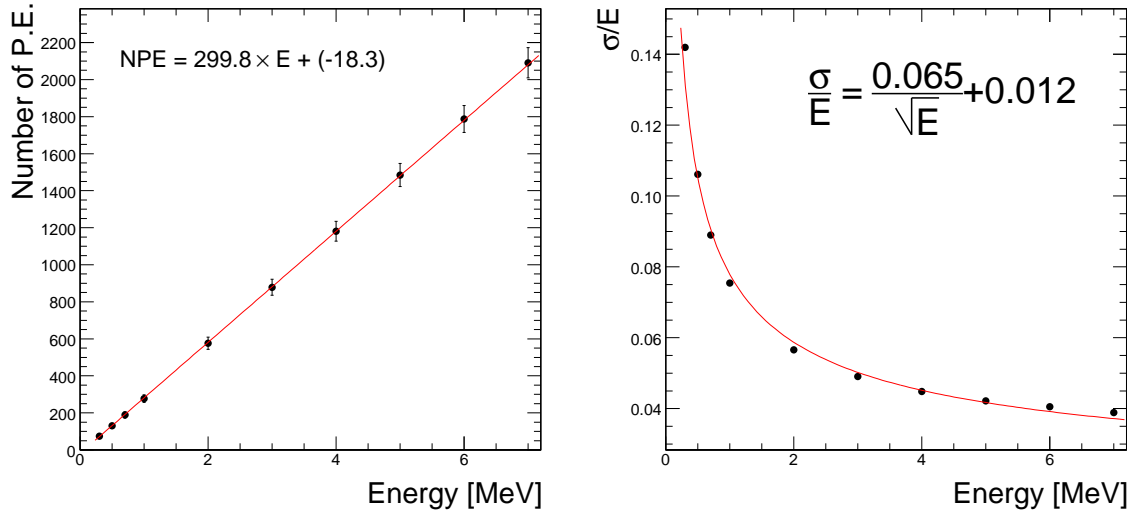


Figure 6.13: Energy linearity (left) and energy resolution (right).

gamma ray and Fig. 6.13 shows energy linearity and resolution.

### Muon Tracking

Even though the detectors are installed underground, the cosmic muons can still penetrate into the surrounding rocks and generate fake signals similar to the inverse beta decay from the anti-neutrinos. To reduce the background events from these cosmic muons, we have developed muon tracking algorithm.

- Muons passing through the detector

The RENO detector consists of four concentric cylindrical modules. Those modules are filled with different liquids; Gd loaded liquid scintillator in target, liquid scintillator in  $\gamma$ -catcher, mineral oil in buffer, and water in veto. Therefore, the muons can generate

photons in two ways through the detector; Cerenkov radiation and scintillation.

- Test of the earliest photon hit time

To study the arrival time of photons from incident muons, we have generated muons events with  $20 \text{ GeV}/c$ , going down vertically through the center of the detector. The relationship between the photon hit time and the number of photoelectrons was investigated for each PMT. It was found that the earliest photon hit was always registered in a PMT within a group of neighboring PMTs with photon hits (PMT cluster), which is true regardless of photon generation mechanism of a muon event. We also investigated the relationship between the distance of closest approach to a PMT and the amount of light it sees relative to the neighboring PMTs for the exit point of muon track.

- Muon tracking algorithm

The muon tracking algorithm finds the incident muon's entrance point on the detector by taking the PMT with the earliest time that has at least two nearest neighboring PMTs in a cluster. And the exit point of the muon track is determined using the PMT with the highest number of photoelectrons that also has at least two nearest neighboring PMTs with hits in a cluster. The muon track is obtained by tracing the straight path from the entrance and exit positions.

From the simulation, when muons pass through the active layers (target and  $\gamma$  catcher), muons are tagged with an 100% efficiency. To reconstruct the trajectory of each through-going muon, we combine information obtained from inner detector PMTs, which are mounted on the buffer vessel, as well as outer detector PMTs, which are mounted on veto wall. The best fit muon track is reconstructed by tracking the path from entrance point from inner detector PMTs and the exit point from outer detector PMTs (Fig. 6.14). The angular difference between the reconstructed muon track and the simulated muon track is shown in Fig. 6.15.

### Event Display

An event display tool based on ROOT is under development. Figure 6.16 shows a rudimentary event display of sample events.

## 6.4 Optimization of the Detector Design

One of the important goals of the Monte Carlo simulation studies is to design a cost effective detector with a good detection efficiency and performance. This section describes how the optimization of the RENO detector was done.

### 6.4.1 Target Mass

With the goal of having systematic uncertainty less than 1%, we estimated the 90% confidence level (CL) limit on  $\sin^2(2\theta_{13})$  as a function of target mass times number of years of data taking as shown in Fig. 6.17 (see Sect. 8.2). The target mass is determined to be 16 tons as a result of compromise between construction cost and measurement sensitivity. With three years of data taking and the target mass of 16 tons we expect to set a limit on the neutrino mixing angle down to  $\sin^2(2\theta_{13}) = 0.02$ .

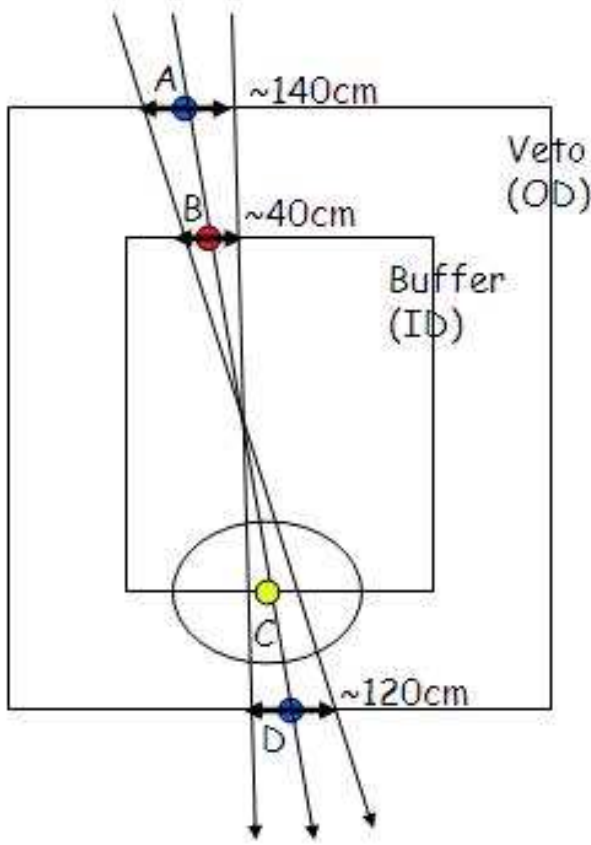


Figure 6.14: Schematic of the reconstructed through-going muon track. The best fit muon track is constructed with hit information from the inner detector PMTs for the entrance point and the outer detector PMTs for the exit point ( $\bar{B}\bar{D}$ ).

#### 6.4.2 $\gamma$ -Catcher Thickness

The purpose of  $\gamma$ -catcher is to contain energy of gamma rays escaping from the target vessel. In target,  $\gamma$  rays are produced by the positron-electron annihilation and by the neutron capture. It is found that some of gamma rays from the neutron capture can escape even from  $\gamma$ -catcher, and cannot be fully contained if  $\gamma$ -catcher is not thick enough. Using the simulation, neutron detection efficiency has been obtained for several different thicknesses of  $\gamma$ -catcher as shown in Fig. 6.18. Here, again a compromise has been made between detection efficiency and the construction cost. The thickness of  $\gamma$ -catcher is chosen to be 60 cm where 93% of Gd captured neutron events passing  $E > 6$  MeV requirement.

#### 6.4.3 Buffer Thickness

The buffer layer is used to shield the active area of target and  $\gamma$ -catcher against photons from radioactivities in the PMTs and the surrounding rocks. Increasing the thickness of the buffer layer reduces these photon backgrounds while increasing the construction cost as well.

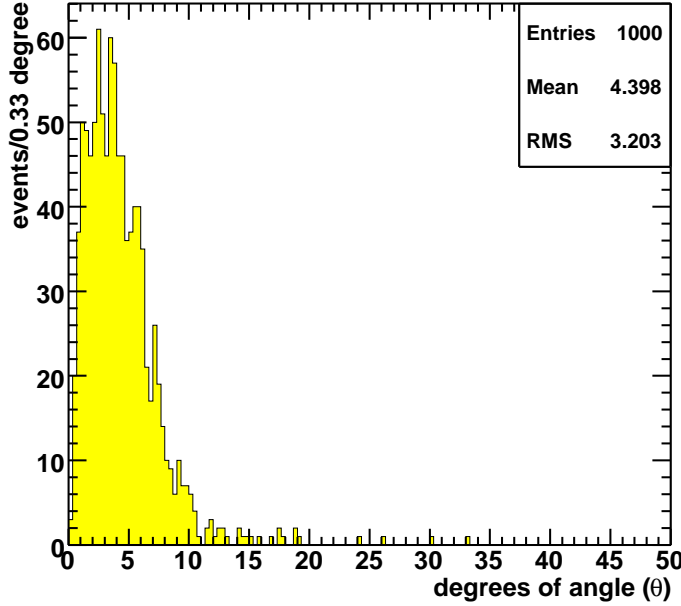


Figure 6.15: Angular difference between the reconstructed muon track and the simulated muon track.

Buffer Thickness (cm)	$^{40}\text{K}$	$^{232}\text{Th}$	$^{238}\text{U}$	Total
50	3.4	8.0	11.2	22.6
60	2.0	5.3	7.1	14.4
70	1.4	3.9	5.1	10.4
80	0.8	2.7	3.6	7.1
90	0.5	1.6	1.9	4.0
100	0.3	1.4	1.1	2.8

Table 6.3: Event rates from radioactivities in the PMTs with energy above 1 MeV. Rates are in Hz.

Therefore, the thickness of the buffer layer is determined to be large enough to reduce the photon backgrounds to an acceptable level from Monte Carlo studies.

The gammas from the radioactive decays of  $^{40}\text{K}$ ,  $^{232}\text{Th}$  and  $^{238}\text{U}$  in PMTs are simulated and traced through the whole detector media. The optical photons generated in the liquid scintillator due to the gamma rays are traced in the detector until they reach the PMTs. The simulation was repeated for six buffer thicknesses from 50 cm to 100 cm in steps of 10 cm and the results are shown in Table 6.3. We chose the buffer thickness of 70 cm to limit the rate of events above 1 MeV coming from the radioactivities.

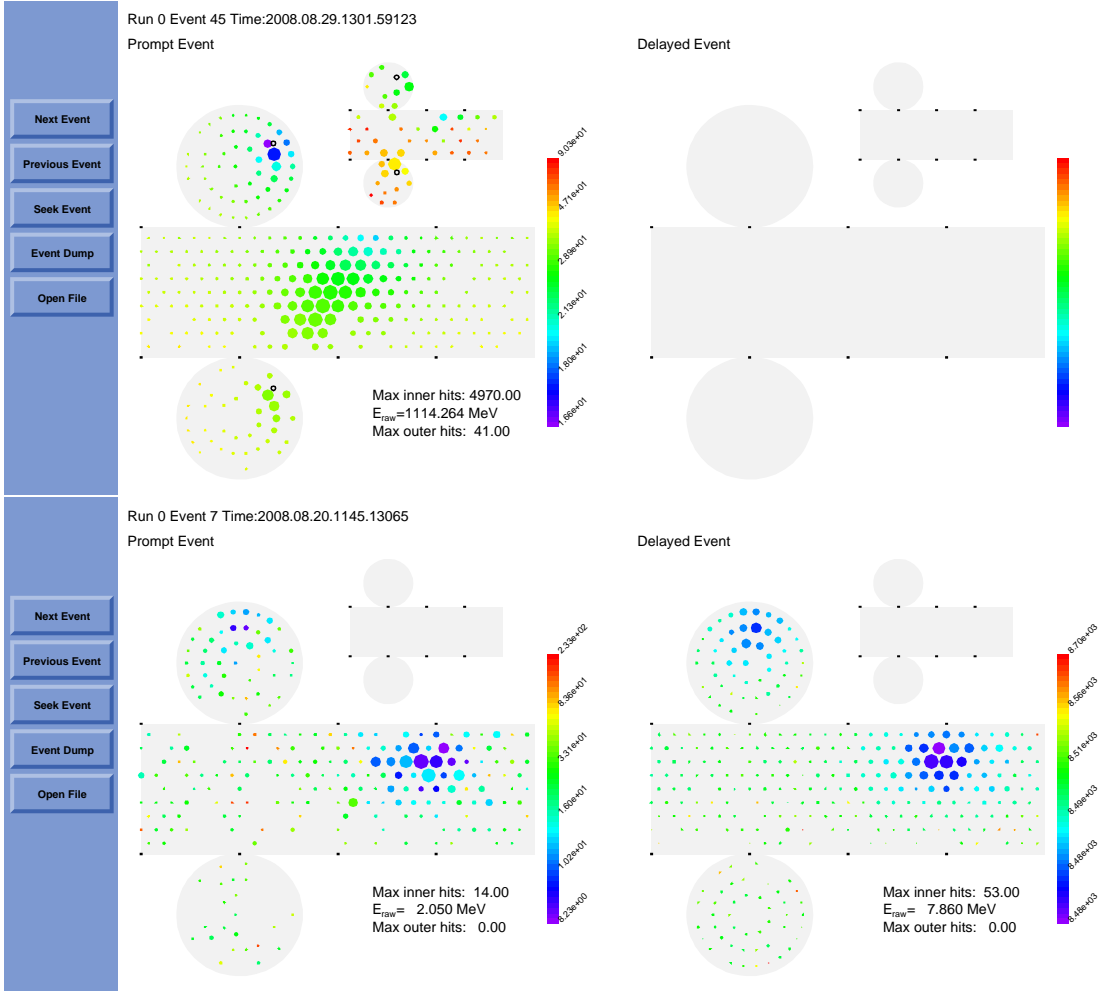


Figure 6.16: Examples of 2D-event display of a simulated cosmic ray event (top) and of a simulated inverse beta decay event (bottom). The large (small) cylinder development represents the buffer (veto) vessel surface where The colored circles shows the hits on PMTs with their radius proportional to the number of hits. The first hit time is color coded. Note that the PMT locations are not for the latest design.

## 6.5 Detection Efficiencies and Uncertainties

### 6.5.1 Introduction

Based on the various studies we have attempted to design the RENO detector with a good efficiency and small systematic uncertainties. Due to addition of  $\gamma$ -catcher and buffer modules, several geometrical requirements used by CHOOZ experiment are not needed at RENO experiment; fiducial cuts on positron and neutron vertices, and the cut on the positron-neutron vertex distance.

### 6.5.2 Positron Detection Efficiency

An IBD event is identified by a prompt signal from the positron followed by the neutron capture on Gd producing gamma rays with total energy of about 8 MeV. The positron deposits its

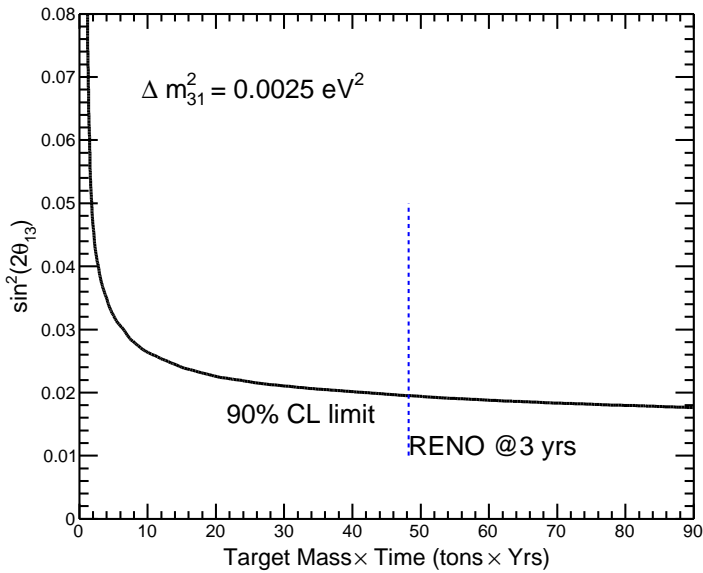


Figure 6.17: The 90% CL limit of  $\sin^2(2\theta_{13})$  as a function of number of years of data taking times target mass at  $\Delta m_{31}^2 = 0.0025 \text{ eV}^2$ . The intercept in the limit by the dashed line shows the expected limit by RENO experiment with target mass of 16 tons in three years.

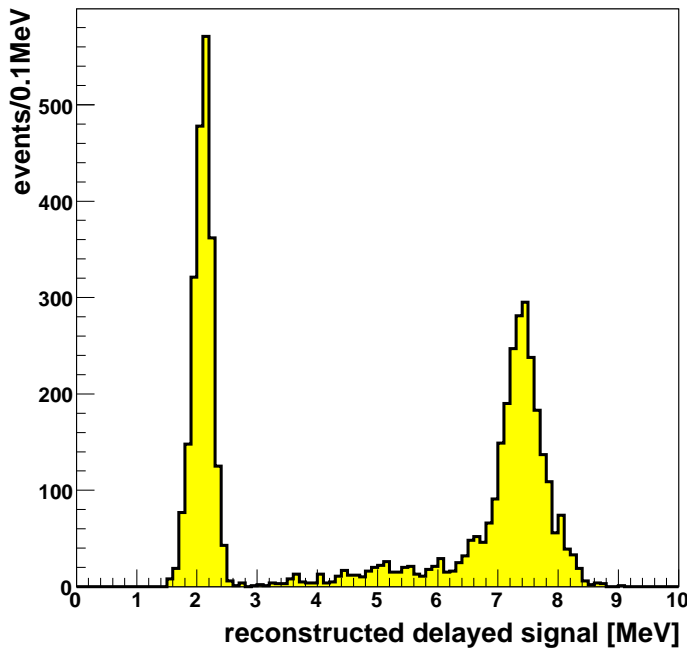


Figure 6.18: The reconstructed energy spectrum of neutrons captured in the target volume. The peaks at  $\sim 2.0 \text{ MeV}$  and  $\sim 7.5 \text{ MeV}$  are from neutrons captured by hydrogen and Gd, respectively.

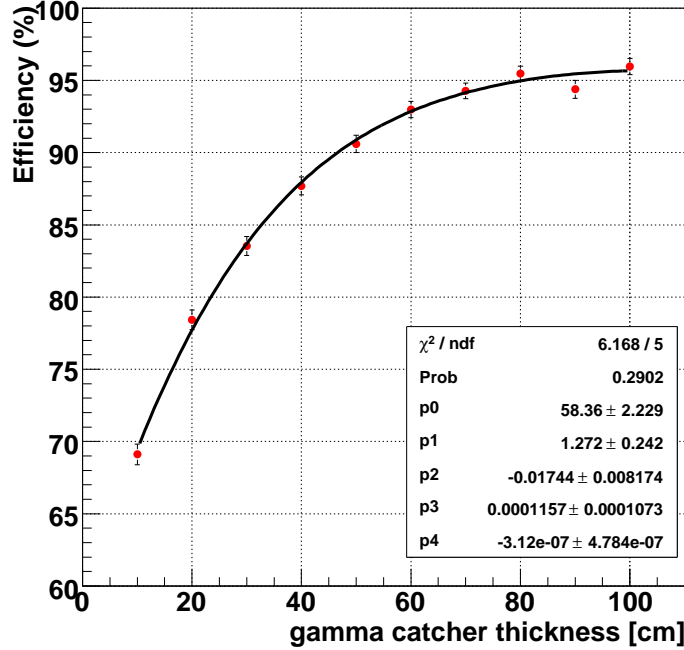


Figure 6.19: The Gd captured neutrino detection efficiency as a function of the  $\gamma$ -catcher thickness. The cut used is  $E > 6$  MeV.

kinetic energy through scintillation and then annihilates to yield two gammas with 0.51 MeV each. Thus the minimum energy from the prompt signal is 1.02 MeV. Therefore, the energy requirement of  $E > 1$  MeV for the prompt signal should be fully efficient. However, the reconstructed energy could be less than 1 MeV as shown in Fig. 6.20 because of a finite energy resolution of the detector, which is 6.5% at 1 MeV. We studied the change of the reactor neutrino event rate depending on the positron energy threshold assuming the energy scale uncertainty of 2% using Monte Carlo calculations. The detection efficiencies are found to be 99.23, 99.14, and 99.05% at the positron energy thresholds of 0.94, 1.00, and 1.02 MeV, respectively. Therefore, we estimate the positron detection efficiency with the 1 MeV threshold requirement as  $99.1 \pm 0.1\%$ .

### 6.5.3 Neutron Detection Efficiency

The efficiency for detecting a neutron is given by

$$\varepsilon = P_{Gd}\varepsilon_E\varepsilon_T, \quad (6.18)$$

where  $P_{Gd}$  is the probability of a neutron being captured by Gd,  $\varepsilon_E$  is the efficiency of the  $E > 6$  MeV cut for gamma rays from the neutron Gd capture, and  $\varepsilon_T$  is the efficiency of the delayed time cut,  $0.3 < T < 200 \mu s$ . The combined neutron detection efficiency is estimated to be  $79.3 \pm 0.5\%$ .

### Neutron Capture Fraction on Gd

The neutron capture fraction on Gd is expected to be 85.3% in a liquid scintillator with a 0.1% Gd concentration. We studied the relation between the neutron capture fraction on Gd

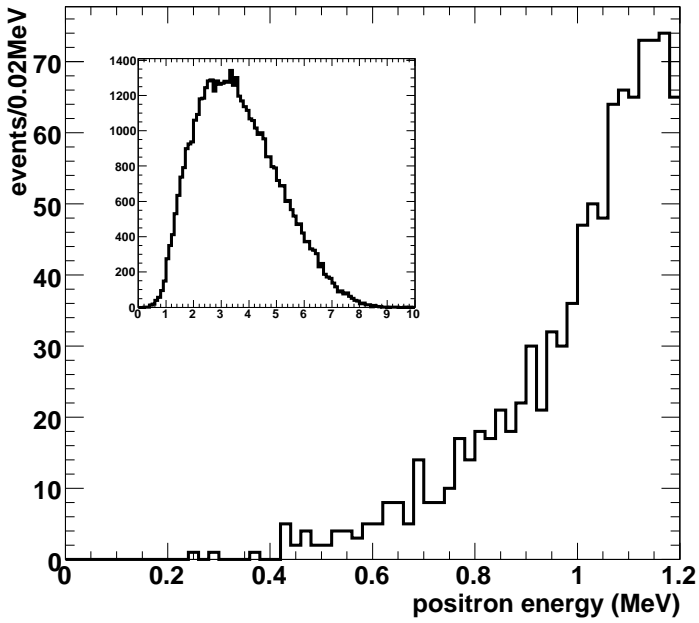


Figure 6.20: Simulated measured positron energy spectrum near the threshold from reactor neutrinos. The full range of the spectrum is shown in the inset.

and the capture time with the various concentration of Gd using Monte Carlo calculations. In Fig. 6.21 the result shows that the capture time difference of  $1 \mu\text{s}$  gives about 0.4% change in the Gd capture fraction. Our goal is to measure the relative Gd captured neutron fraction to 0.4% precision and ultimately to 0.1%. Since we expect to measure the capture time to better than  $1 \mu\text{s}$  uncertainty with less than  $10^4$  neutron capture events, which can be obtained in a few minutes of data taking with a neutron source, we take 0.4% to be the neutron capture fraction uncertainty.

### Efficiency of Energy Cut

The gammas Gd captured neutron event have a total energy of  $\sim 8 \text{ MeV}$ , whereas low energy backgrounds mainly coming from radioactive sources mostly have energy below 1 MeV. To discriminate low energy backgrounds as well as prompt signals and hydrogen captured neutron signals,  $E > 6 \text{ MeV}$  requirement is imposed on the delayed signal. This cut was studied using Monte Carlo simulation (see Fig. 6.19). The efficiency of the energy cut is found to be  $93.0 \pm 0.4\%$ , assuming the energy scale uncertainty of 2%.

### Efficiency of Delayed Time Cut

The delayed time cut of  $1.0 < T < 200 \mu\text{s}$  was studied using an MC simulation with a 0.1% Gd concentration in the liquid scintillator. The efficiency of the delayed time cut is found to be 95%. Assuming an 1 ns precision of the electronics, the systematic uncertainty of the efficiency of this cut is negligible.

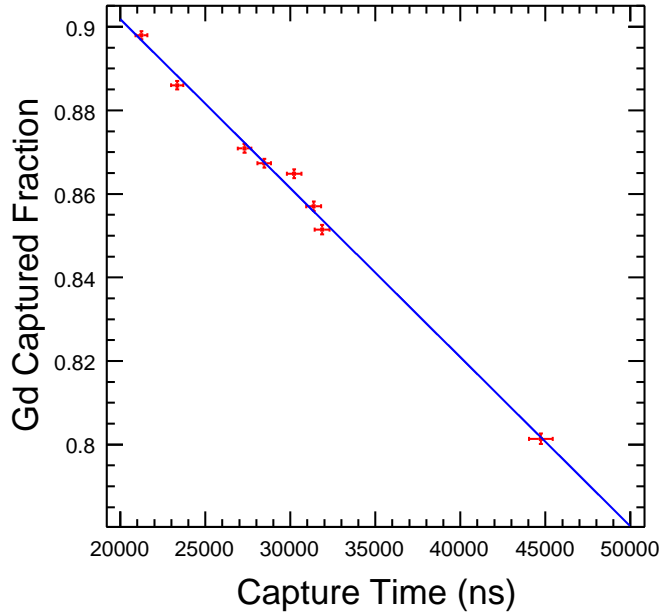


Figure 6.21: Fraction of neutrons captured by Gd vs. capture time for various Gd concentrations in the target liquid scintillator. The Gd concentration was varied from 0.06 to 0.15%.

### Neutron Multiplicity

In CHOOZ experiment the muon-induced spallation neutron events were rejected with an efficiency of  $97.4 \pm 0.5\%$  [9]. In RENO these events will be identified with a very high efficiency due to having the veto layer unlike CHOOZ. Therefore, we consider the cut efficiency on the neutron multiplicity fully efficient and its systematic uncertainty to be negligible.

#### 6.5.4 Dead Time

In RENO experiment the electronics does not introduce dead time. However, vetoing cosmic muon events can introduce dead time. We plan to use a 0.5 ms veto duration after each muon event. In RENO experiment the muon fluxes are estimated to be  $5.5 \text{ Hz/m}^2$  and  $0.85 \text{ Hz/m}^2$  for near and far detectors, respectively. Therefore, we estimate the veto efficiencies associated with dead time to be 75.4% and 95.8% for near and far detectors, respectively.

#### 6.5.5 Summary

The detector related efficiencies with respect to inverse beta decay events are summarized in Table 6.4. The total detection efficiencies are expected to be  $56.3 \pm 0.5\%$  and  $71.6 \pm 0.5\%$  for near and far detector, respectively.

Cut	Efficiency (%)	
	CHOOZ	RENO
Positron energy	$97.8 \pm 0.8$	$99.1 \pm 0.1$
Positron-geode distance	$99.9 \pm 0.1$	–
Neutron capture	$84.6 \pm 1.0$	$85.3 \pm 0.4$
Capture energy containment	$94.6 \pm 0.4$	$93.0 \pm 0.4$
Neutron-geode distance	$99.5 \pm 0.1$	–
Neutron delay	$93.7 \pm 0.4$	$95.0 \pm 0.0$
Positron-neutron distance	$98.4 \pm 0.3$	–
Neutron multiplicity	$97.4 \pm 0.5$	–
Dead time	–	$75.4$ (near) $95.8$ (far)
Total	$69.8 \pm 1.5$	$56.3 \pm 0.5$ (near) $71.6 \pm 0.5$ (far)

Table 6.4: Event selection efficiencies.

## 6.6 Background Simulation

### 6.6.1 Simulation of Muon Background

An accurate and efficient method of calculating the muon intensity and energy at the underground site requires the detailed profile of surrounding terrain and the parameterization of muon intensity at its surface. A standard atmospheric muon parameterization given by Gaisser [10] is well known for describing the muon intensity at the surface in the high energy region but poor in the low energy region. Since detector sites are at relatively shallow depth ( $\sim 200$  m), low energy muons can survive at the depth. To consider the effect, we use the modified Gaisser parameterization [11] in the low energy region. The Gaisser parameterization is written as

$$\frac{dN_{\mu 0}}{dE_{\mu 0} d\Omega} \simeq A \frac{0.14 E_{\mu 0}^{-\gamma}}{\text{cm}^2 \text{ sr } s \text{ GeV}} \left\{ \frac{1}{1 + \frac{1.1 \tilde{E}_{\mu 0} \cos \theta^*}{115}} + \frac{0.054}{1 + \frac{1.1 \tilde{E}_{\mu 0} \cos \theta^*}{850}} + r_c \right\}, \quad (6.19)$$

where muon energy  $E_{\mu 0}$  at the surface is measured in GeV. The standard Gaisser parameterization has  $A = 1$ ,  $\gamma = 2.7$ ,  $\tilde{E}_{\mu 0} = E_{\mu 0}$ , and  $r_c = 0$ . The detailed parameters for the modified Gaisser parameterization are

$$\begin{aligned} \gamma &= 2.70, \\ r_c &= 10^{-4}, \\ \Delta &= 2.06 \times 10^{-3} \left( \frac{950}{\cos \theta^*} - 90 \right), \\ \tilde{E}_{\mu 0} &= E_{\mu 0} + \Delta, \\ \text{and} \\ A &= 1.1 \left( \frac{90 \sqrt{\cos \theta + 0.001}}{1030} \right)^{\frac{4.5}{\tilde{E}_{\mu 0} \cos \theta^*}}, \end{aligned}$$

Depth	Integrated intensity ( $\text{cm}^{-2}\text{s}^{-1}$ )	Average energy (GeV)
70 m	$5.5 \times 10^{-4}$	34.3
200 m	$8.5 \times 10^{-5}$	65.2

Table 6.5: Result of muon transport simulation for the detector sites.

where  $\cos \theta^*$  is calculated using a simple geometrical extrapolation as

$$\cos \theta^* = \sqrt{\frac{x^2 + p_1^2 + p_2 x^{p_3} + p_4 x^{p_5}}{1 + p_1^2 + p_2 + p_4}}. \quad (6.20)$$

Here  $x$  denotes  $\cos \theta$  and  $\theta$  is the angle subtended between the incoming cosmic ray particle and the normal to the upper atmospheric layer, and  $p_1 = 0.102573$ ,  $p_2 = -0.068287$ ,  $p_3 = 0.958633$ ,  $p_4 = 0.0407253$ , and  $p_5 = 0.817285$ .

Muon generated uniformly in the energy range,  $\theta$ , and azimuthal angle are propagated through the rocks using MUSIC. MUSIC is a code that simulates the 3-dimensional transportation of muons through a slant depth of a material, taking into account the energy loss due to the ionization, pair production, Bremsstrahlung, and inelastic scattering [12, 13]. We calculated the integrated muon intensity and average energy at the near and far detector sites, 70 m and 200 m in depth, respectively, as given in Table 6.5. The muon energy spectra of the detector sites are shown in Fig. 6.22.

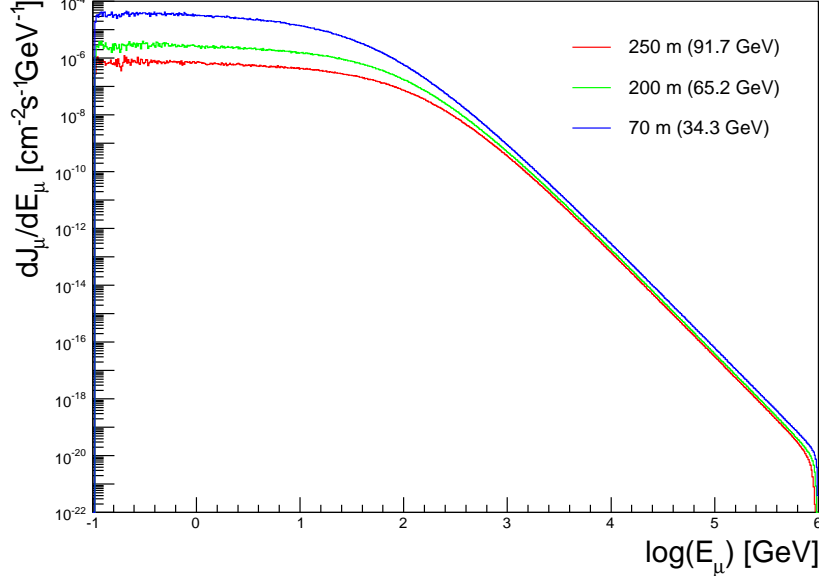


Figure 6.22: The differential muon intensity at depths of 70, 200, and 250 m underground. far detector candidates and near detector candidate. The numbers in the parenthesis are average muon energy.

### 6.6.2 External Neutron Background

The fast neutron produced by a cosmic muon in surrounding rock or in the detector can mimic an inverse beta decay signal in the detector in two ways. First, the fast neutrons with energy

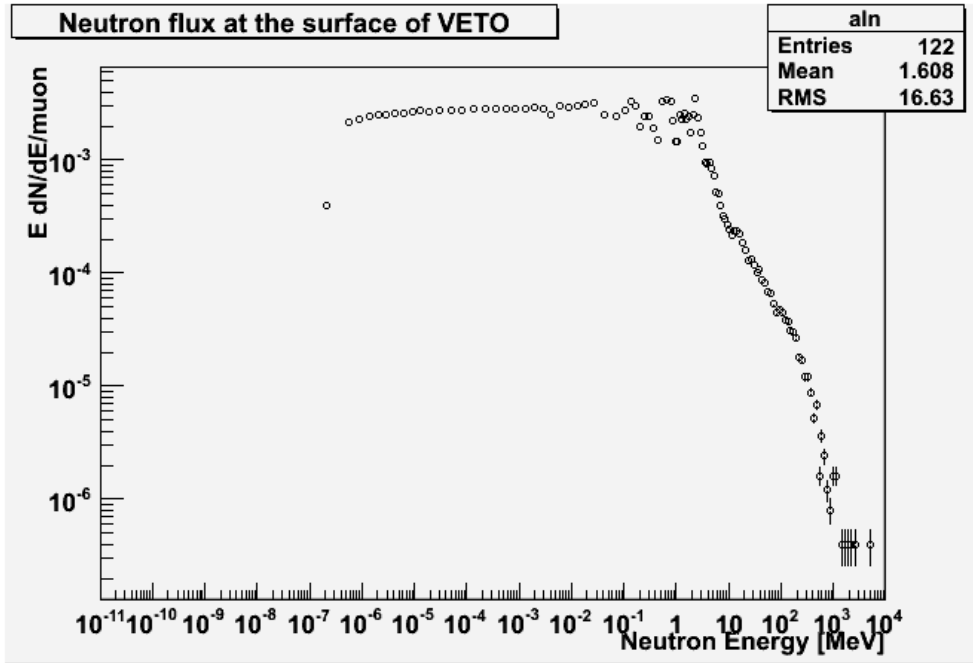


Figure 6.23: Neutron energy distribution coming from rock by cosmic muon

over 10 MeV can be scattered elastically from protons in the target or  $\gamma$ -catcher many times and be captured in the target volume. The quenched proton recoil scintillation signals can be the prompt signal with an energy between 1 and 10 MeV and the moderated neutrons can be captured with the same time distribution as the neutrino signal. Second, some neutrons are produced without recoil protons by cosmic muons and are captured in the detector. A single neutron capture signal has some probability to fall accidentally within the time window of a preceding signal caused by natural radioactivity in the detector, producing an accidental background. In this case, the prompt and delayed signals are from different sources, forming an uncorrelated background. A detailed neutron production simulation will give the estimation of the neutron background originating from cosmic muons.

A detailed simulation of the cosmogenic background requires accurate information of the overburden profile and rock composition. We assume an uniform rock density of  $2.70 \text{ g/cm}^3$  in the present background simulation. The modified Gaisser formula with corrected polar angle is used to describe muon flux.

At muon energies of several tens of GeV, the standard Gaisser formula has large discrepancies with data while the modified formula agrees with data in the whole energy range. Using the mountain profile data, the cosmic muons are transported from the atmosphere to the underground detector sites using the MUSIC package. The simulation results are shown in Table 6.5 for the detector sites.

The production rate of the cosmogenic neutrons originating from surrounding rocks depends not only on the cosmic muon flux and its average energy at the detector but also on the detector shielding. The external neutron background rate is calculated using FLUKA package, in which the detailed detector site geometries are accounted for. The resulting neutron energy distribution coming from the surrounding rocks is shown in Fig. 6.23.

Mei and Hime parametrized the total neutron flux as a function of mean muon energy at various depths at underground [14]. The neutron rate at far detector site is estimated using

	near	far
cross section ( $\mu\text{b}$ )	0.61	0.97
( ${}^9\text{Li} + {}^8\text{He}$ )/day	18.6	4.6

Table 6.6: Cosmogenic isotope production rates in RENO experiment estimated from the CERN cross section.

Mei's parameterization to be about  $10^{-2}$  neutrons/m<sup>2</sup>/s. In addition, the energy spectra of muon induced neutrons at rock is simulated again according to Mei's parameterization of the neutron energy spectra as a function of muon energy. We adopted the mean muon energy at far site for the energy spectra. Then GEANT4 simulation was done with  $5 \times 10^6$  neutrons produced at rock surrounding the far detector, and selection cuts for the inverse beta neutrino event were applied; 1–10 MeV for the prompt signal and 6–10 MeV for the delayed signal. The rate of coincident background events due to fast neutrons passing the selection cuts is 2.5 events per day at the far detector. A further reduction larger than a factor of two on the background rate is expected by rejecting the events with neutron induced signals at the veto detector. Therefore, the expected fast neutron background at the far detector is estimated to be about 1 event per day. We plan to understand the background rate with an uncertainty better than 50%.

### 6.6.3 Radioactive Isotopes Induced by Cosmic Ray Muons

From the experiences of previous reactor neutrino experiments such as KamLAND and CHOOZ, we know there are irreducible background events from the decay of cosmogenic isotopes. Most prominent radioactive isotopes are  ${}^8\text{He}$  and  ${}^9\text{Li}$ .  ${}^8\text{He}$  decays by  $\beta^- + n$  (16%,  $Q_{\beta^-} = 10.653$  MeV) with a half-life time of 119 ms.  ${}^9\text{Li}$  decays by  $\beta^- + n$  (49.5%,  $Q_{\beta^-} = 13.606$  MeV) with a half-life time of 178.3 ms. The  $\beta^- + n$  decay gives a prompt and delayed signal similar to an IBD events.

The production rates of these long-lived cosmogenic isotopes are studied initially by rock dating group. There are a lot of data available on the production rates of  ${}^{10}\text{Be}$  and  ${}^{26}\text{Al}$  from silicon and oxygen by cosmic muons. The production cross section of  ${}^8\text{He}$  and  ${}^9\text{Li}$  in the carbon has been measured with accelerator muon beams at an energy of 190 GeV at CERN[15]. Their combined cross section is  $\sigma({}^9\text{Li} + {}^8\text{He}) = (2.12 \pm 0.35) \mu\text{b}$ . The energy dependent production cross section is estimated as  $\sigma_{tot} = E_\mu^{0.73}$ , where  $E_\mu$  is the muon energy. The  ${}^8\text{He} + {}^9\text{Li}$  background cross section and rate are estimated by using the average muon energies at near and far detector sites and the results are listed in Table 6.6.

In addition, we can use the measured data in the previous reactor neutrino experiments to estimate the cosmogenic isotope production rates. The CHOOZ collaboration presented the  ${}^8\text{He}$  and  ${}^9\text{Li}$  background rate as  $0.7 \pm 0.2$  events per day for their 5 ton target mass [9]. If we scale this rate to RENO detector mass and use the dependence of production rate on the muon energy, then we have 9.3 and 2.3 events per day for near and far detectors, respectively, which are half of the event rates estimated with the CERN cross section data.

KamLAND experiment reported that their  ${}^8\text{He}$  and  ${}^9\text{Li}$  backgrounds are correlated with showering muons, which has more than  $10^6$  photoelectrons, and they applied two second veto for the muons. For RENO experiment, we plan to apply 1 ms veto for non-showering muons and 5 ms for showering muons. This veto on the showering muons will further reduce the  ${}^8\text{He}$  and  ${}^9\text{Li}$  background rate by about 70%. The final expected  ${}^8\text{He}$  and  ${}^9\text{Li}$  background rates will be 2.8 and 0.7 events per day for near and far detectors, respectively.

	$^{40}\text{K}$	$^{232}\text{Th}$	$^{238}\text{U}$
Target LS	0.20	1.34	1.25
Target Acrylic	0.09	0.67	0.79
GC LS	0.23	1.29	1.25
GC Acrylic	0.04	0.28	0.35
Buffer Oil	0.007	0.05	0.05
Buffer Vessel	0.0005	0.007	0.004
PMT	0.01	0.04	0.04

Table 6.7: Detector acceptance of the radioactive radiations from each detector subsystem with 1 MeV threshold.

#### 6.6.4 Radioactive Backgrounds

Radioactive isotope (*i.e.* radionuclide) is an atom with an unstable nucleus. They undergo radioactive decay, and emit a gamma(s) and/or subatomic particles like alpha, electron and positron, *etc*. Some radioactive isotopes, like  $^{40}\text{K}$ ,  $^{60}\text{Co}$ ,  $^{232}\text{Th}$ , and  $^{238}\text{U}$ , are naturally abundant in detector materials and rocks around the detector hall. Energetic gammas and particles coming from radioactive decay of isotopes in the inner detector can create accidental and correlated backgrounds. Especially, the signal made by radioactive gamma and electron can mimic the prompt signal of the inverse beta decay. This background can form an accidental (uncorrelated) background with the single neutron events induced by cosmic muons.

Radioactive background can come from a variety of sources, mainly inner detector materials and the rock. In this study, we consider K, Th, and U isotopes as the radioactive sources existing in the following materials.

- rocks surrounding the detector hall
- liquid scintillators
- acrylic vessels
- buffer oil
- stainless steel vessel
- PMT glasses

Most radioactive isotopes do not decay directly to a stable state, but rather undergo a series of decays until a stable isotope is reached eventually. Figures 6.24 shows the decay chains of  $^{238}\text{U}$  and  $^{232}\text{Th}$ . Figure 6.25 shows the energy level diagram for  $^{40}\text{K}$  decay. Gamma emission occurs not only when a radioactive isotope undergoes gamma decay, but also when a beta particle from an isotope decay emits gammas. To take account of probability of decay and coincidence of generated particle, a decay chain generator is developed.

Using the radioactive decay chain generator, radiations from three dominant decay chains are generated at the detector subsystem. We apply 1 MeV threshold to the reconstructed energy. Table 6.7 shows the detector acceptance of the radiation from each radioactive isotope decay chain.

The concentration of isotopes in the inner detector material is measured using ICP-MS and HPGe detector. With the concentration and the detector acceptance from full simulation, the single event rates caused by each detector subsystem are calculated. Table 6.8 shows

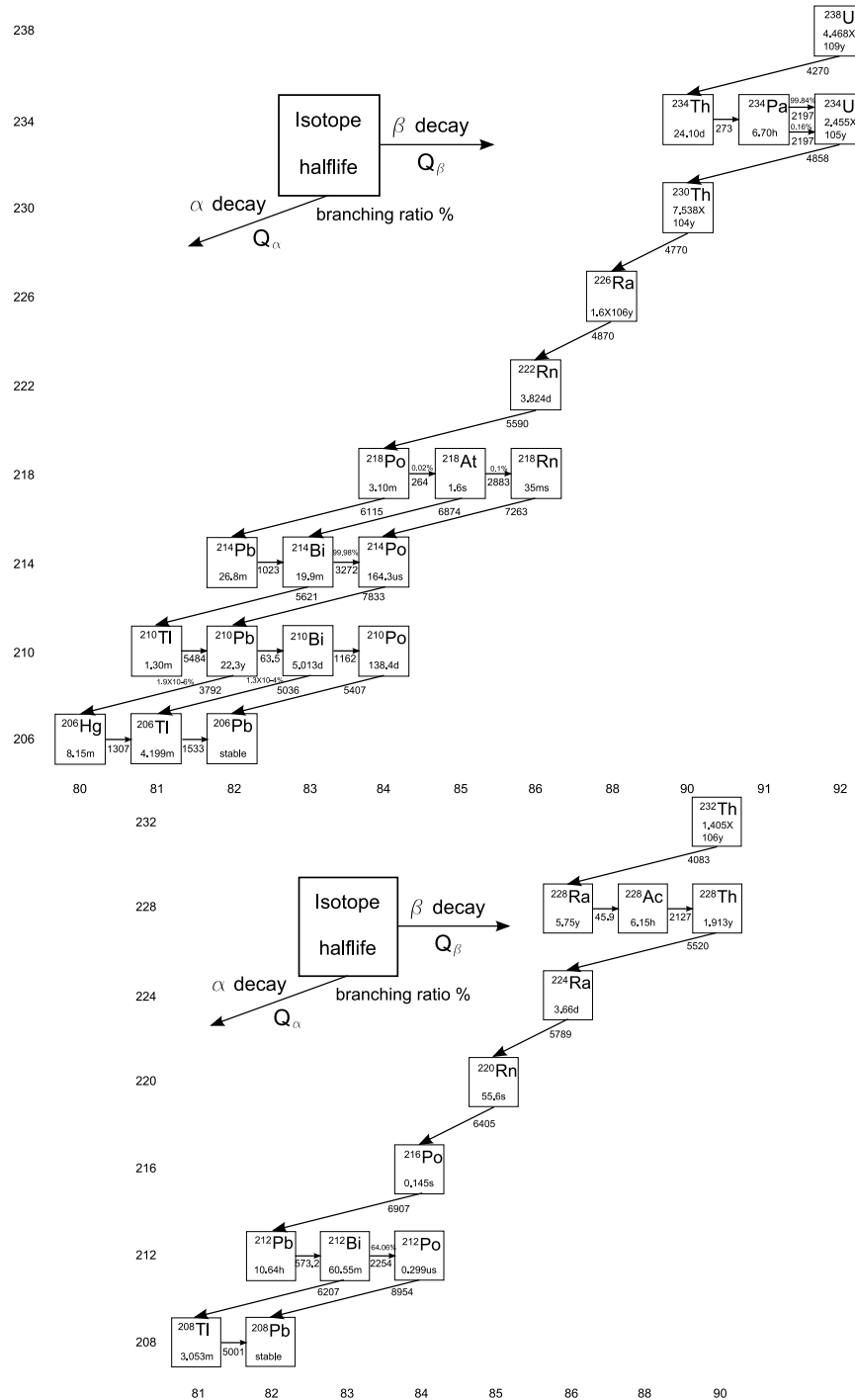


Figure 6.24: Decay chains of  $^{238}\text{U}$  and  $^{232}\text{Th}$  series

the results. The most dominant contribution comes from the liquid scintillator in target and gamma catcher. But if we control the concentration of the isotopes under  $10^{-12}\text{g/g}$ , these rates are negligible compared to that from PMT glass. Figure 6.26 shows the weighted energy spectrum from the radioactive isotopes in each detector subsystem.

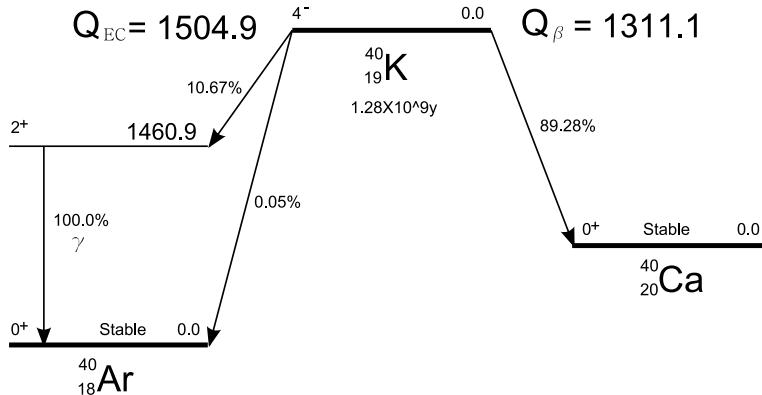


Figure 6.25: Level diagram for  $^{40}\text{K}$

	$^{40}\text{K}$ ppt	$^{232}\text{Th}$ ppt	$^{238}\text{U}$ ppt	Single Event Rate Hz
Rock	4.33(ppm)	7.58(ppm)	2.32(ppm)	9.2
Target LS	< 0.32	17.7	13.9	< 5.6
Target Acrylic	8	206.8	167.5	0.95
GC LS	< 0.32	17.7	13.9	< 8.4
GC Acrylic	8	206.8	167.5	0.87
Buffer Oil	10	19.7	5.0	1.07
Buffer Vessel	60	900	900	0.33
PMT	10.8	125.9	50.3	8.19
Total				< 34.6

Table 6.8: Concentrations of  $^{40}\text{K}$ ,  $^{232}\text{Th}$ , and  $^{238}\text{U}$  in surrounding rock and the main components of RENO detector, and their event rates.

## 6.7 Summary of Backgrounds

The background event rates are summarized in the Table 6.9. The single background rate over 1 MeV energy is about 45 Hz for both near and far detectors. The correlated background rates will be 1.7 and 5.8 events per day at far and near detector, respectively.

	Near	Far
Gamma Single Rates(Hz)	$\sim 30$	$\sim 30$
$^8\text{He} + ^9\text{Li}$ (/day)	2.8	0.7
Correlated Neutron Backgrounds (/day)	3.0	1.0

Table 6.9: Summary of backgrounds for single hit events over 1 MeV and correlated neutrino-like events at both near and far detector.

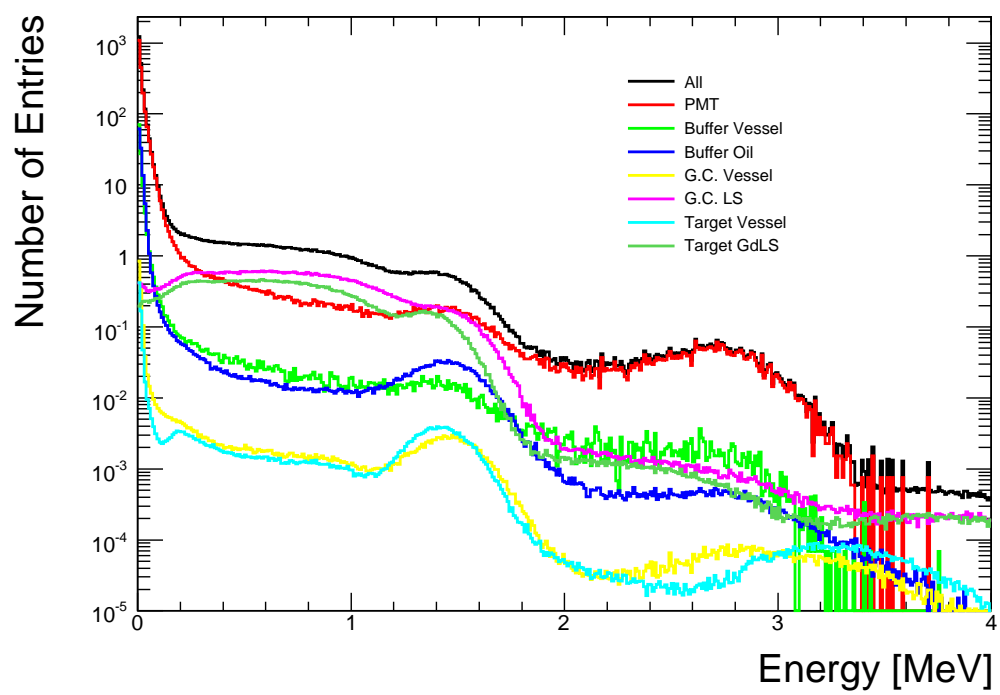


Figure 6.26: The energy distributions of backgrounds due to radioactive material in each subsystem.

# Bibliography

- [1] C. H. Llewellyn Smith, Phys. Rep. **3**, 261 (1972).
- [2] P. Vogel, J. F. Beacom, Phys. Rev. D **60**, 053003 (1999).
- [3] S. A. Fayans *et al.*, J. Phys. G. **5**, 209 (1979).
- [4] C. Bemporad, G. Grata, and P. Vogel, Rev. Mod. Phys. **74**, 297 (2002).
- [5] Th. Förster, Ann. Phys. (Leipz), 2 (1948) 55.
- [6] D.L. Dexter, J. Chem. Phys. **21** (1953) 836.
- [7] P. Huber and T. Scwetz, Phys. Rev. D **70**, 053011 (2004).
- [8] P. Vogel and J. Engel, Phys. Rev. D **39**, 3378 (1989).
- [9] M. Apollonio *et al.*, Eur. Phys. J. C **27**, 331 (2003).
- [10] T. K. Gaisser and T. Stanev, Phys. Lett. B **592**, 228 (2004).
- [11] A. Tang, G. Horton-Smith, V. A. Kudryavtsev, and A. Tonazzo, Phys. Rev. D **74**, 053007 (2006).
- [12] P. Antonioli, C. Ghetti, E. V. Korolkova, V. A. Kudryavtsev, and G. Sartorelli, Astropart. Phys. **7**, 357 (1997).
- [13] V. A. Kudryavtsev, E. V. Korolkova, and N. J. C. Spooner, Phys. Lett. B **471**, 251 (1999).
- [14] D.-M. Mei and A. Hime, Phys. Rev. D **73**, 053004 (2006).
- [15] T. Hagner *et al.*, Astropart. Phys. **14**, 33 (2000).

# Chapter 7

## Calibration

### 7.1 Overview

Since the  $\theta_{13}$  measurement depends on the systematic uncertainties in the relative parameters between near and far detectors, it is important to understand detector performance in great detail. There are three major motivations for having the calibration system. First, the characteristics of the events in the energy range of 1–10 MeV depend on the positions of the event vertex since the scintillation lights propagate through the liquid scintillator, acrylic vessel, and buffer oil. The vertex position dependence of energy measurement can be understood by placing a radioactive source at various locations inside the liquid scintillator and measuring the energy deposit. The detail optical parameters of the liquid scintillator and acrylic vessel, and stainless steel tank can be obtained and compared between two detectors. Second, liquid scintillators may change its scintillation and optical properties during the long-term data taking period. Therefore, it is crucial to monitor the detector response throughout the duration of the experiment. Also, the day and night oscillation in the energy measurement due to temperature and other environmental factors inside and outside of the detector could occur, so the monitoring should be done at all times. Finally, the calibration system could be used to calculate the dead time for inverse beta decay events. Any difference of the dead time between near and far detector should be understood.

### 7.2 Radioactive Sources

The purpose of using radioactive sources is to calibrate the detector response for the inverse beta decay of reactor antineutrinos. A neutrino event generates two signals separated by several tens of  $\mu\text{s}$ . The first signal is from  $e^+$  annihilation with  $e^+$  kinetic energy up several MeV, and the second signal from a neutron with kinetic energy of tens of keV. The neutron capture by Gadolinium isotopes produces several gammas of 1–2 MeV with their total energy of about 8 MeV. Table 7.1 shows the characteristics of radioactive sources to be used for calibrating the detector for both the  $e^+$  and neutron signals.

The size of the radioactive source is limited by the attenuation length of 0.511 MeV gamma ray in case of positron source. The attenuation length of 0.511 MeV gammas in the liquid scintillator is about 10 cm. Therefore, the overall size of the source should be smaller than the attenuation length by several times to minimize the amount of the scintillation light scattering by the source itself. The overall size of the source will be 2 cm  $\times$  3 cm. The material encapsulating the source should be compatible with the scintillator materials, and PTFE could be one of the best candidate materials.

type	sources	energy (keV)	calibration
$e^+$	$^{22}\text{Na}$	511(2)+1274.5	positron
	$^{68}\text{Ge}$	511(2)	position E threshold
$\gamma$	$^{137}\text{Cs}$	662	gamma
	$^{54}\text{Mn}$	835	
	$^{60}\text{Co}$	1173+1333	multiple gamma
neutron	$^{252}\text{Cf}$	neutron + $\sim 10$ MeV	neutron efficiency
	$^{241}\text{Am}+\text{Be}$	neutron + 4.4 MeV	

Table 7.1: A list of radioactive sources for RENO detector calibration.

### 7.3 Light Sources

Low energy background events may be analyzed to monitor the PMT gain and single photoelectron energy resolution. Additional light sources can be used with a definite external trigger for the same purpose. These two continuous monitoring methods are complementary. The light source calibration system can be also used to check the time and position resolutions at various energy ranges. Figure 7.1 shows a conceptual design of the light source and fiber optic system. Ultraviolet (UV) and blue LEDs are used as light sources. A pulse generator selectively fires one of the LEDs with a capability of generating double pulse with variable amplitudes. The pulse width is a few ns. The LED lights are fed into an integrating sphere to make a stable light source and transmitted through the optical fiber. Several different LED can be mounted on the integrating sphere.

In case of UV light the output fiber from the integrating sphere is fanned out into three identical optical fibers. There is an optical shutter for each fiber to be activate only one fiber at one time. The three optical fibers are fixed at the center and edge of target vessel and at the center of  $\gamma$ -catcher vessel. The UV light, when radiated into the target liquid scintillator, is absorbed within a few centimeters from the end of the optical fiber and generates isotropic blue light. The attenuation length is a few centimeters for the light with 400 nm wavelength. This system has advantages of a diffuser ball not being necessary and generating isotropic emission of similar wavelengths to real events. A  $400\ \mu\text{m}$  diameter bare optical fiber is used for light transmission. If a blue LED ( $470\ \mu\text{m}$ ) is used, then the attenuation length of the liquid scintillator can be measured directly, since the liquid scintillator does not undergo scintillation processes and, therefore, is transparent to the emission light.

Alternatively, a diffuser ball with a blue LED can be used. A diffuser ball can be made of a solid Teflon ball or a spherical acrylic shell filled with diffuser material such as Ludox.

The light source calibration system can be used to measure dead time for both near and far detectors by generating double pulses in light intensity corresponding to various neutrino energies. For this purpose, at least a set of fixed light source system will be set up for calibrating each detector for whole data taking period.

### 7.4 Source Driving System

It is a challenging work to load the various sources at desired locations within the liquid scintillator regions of the detector. Signals from a radioactive source should be similar to that of the inverse beta decay events and background events. Therefore, the source driving system itself should affect minimally the propagation of the scintillation lights throughout the detector. The main goals of the calibration using radioactive sources are to measure energy

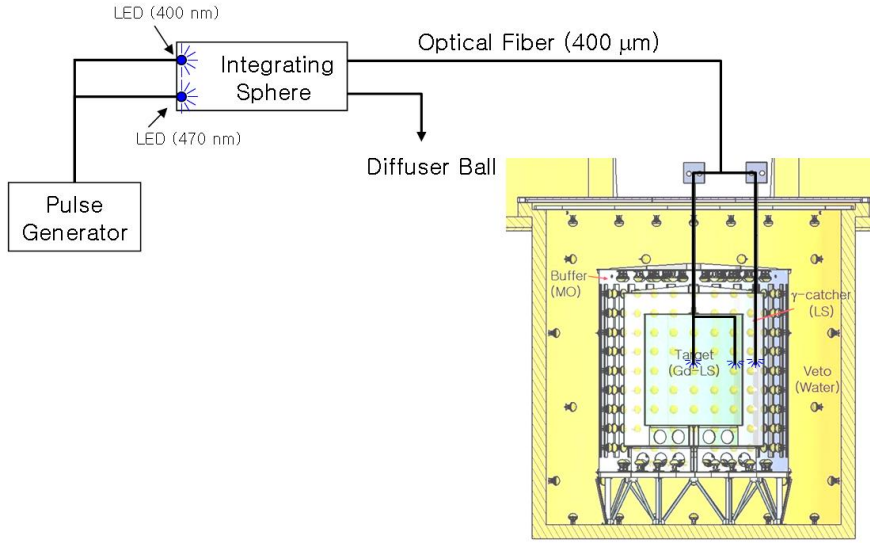


Figure 7.1: A conceptual design of light source system.

scale and resolution, and the vertex position dependence of energy measurement.

The source driving system consists of a stepping motor driven pulley with a polyethylene wire attached. The radioactive source container made of Teflon-PFA is connected at the end of the wire with a weight counteracting buoyant force when submerged in liquids. The pulley has a spiral groove to avoid entanglement of wire. The system is expected to have the z-position accuracy of an order of a few mm, which is much better than the the intrinsic vertex position resolution of the detector.

Figure 7.2 shows the design of the source driving system. The system is enclosed in an air-tight stainless steel glove box and is located on top of the detector as shown in Fig. 7.3. The source driving system is remotely controlled by a computer located in a main control room. The current system can move the radioactive source in z-direction only and a 3-dimensionally deployable system is under development.

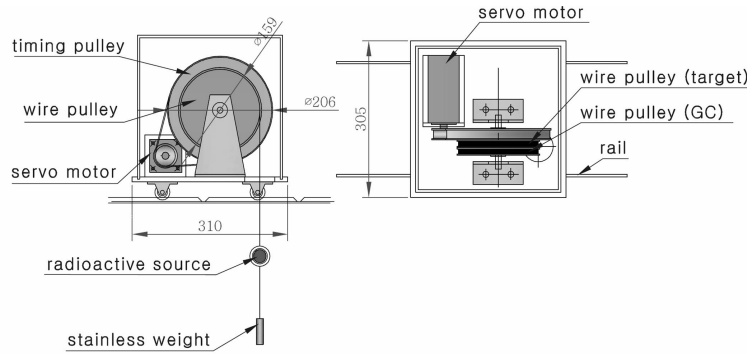


Figure 7.2: Design of RENO source driving system. The wire pulley is driven by a stepping motor via a belt. The radioactive source is encapsulated in a Teflon-PFA capsule attached to polyethylene wire.

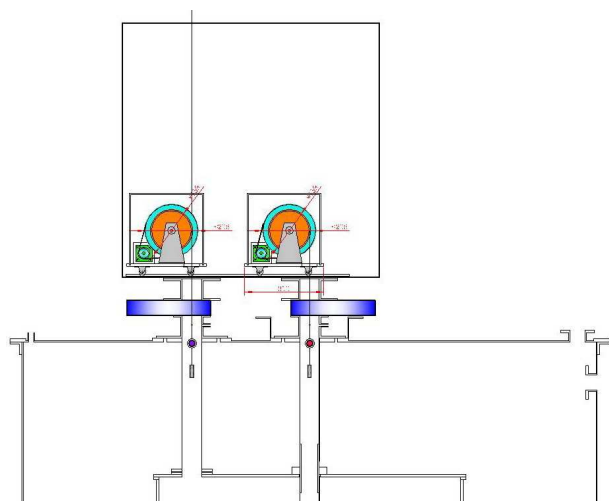


Figure 7.3: The source driving system for the mockup detector. A similar system will be used for the RENO detector.

# Chapter 8

# Systematic Uncertainties and Sensitivity

## 8.1 Systematic Uncertainties

The RENO experiment is expected to record  $\sim 5 \times 10^4$  inverse beta decay events at the far detector over the course of three years of data-taking, yielding a statistical uncertainty of  $\sim 0.4\%$ . Therefore, our goal for the systematic uncertainty is to keep the uncertainty comparable to 0.4% or less to achieve our target sensitivity of  $\sin^2(2\theta_{13}) \lesssim 0.02$  at 90% confidence level (CL).

As a comparison, the CHOOZ experiment, a previous reactor neutrino experiment has set a limit on  $\sin^2(2\theta_{13})$  at  $\lesssim 0.2$  at 90% CL, with 2.8% and 2.7% statistical and systematic uncertainties, respectively [1]. The uncertainties in neutrino flux was dominant source of systematic uncertainty accounting 1.9%. The systematic uncertainty goals for RENO are shown in Tables 8.1 and 8.2.

The sources of systematic uncertainties are reactor related, detector related, and background related. By using two identical detectors, the detector related systematic uncertainties could be mostly cancelled out and, in addition, the effects of reactor related uncertainties are greatly reduced.

### 8.1.1 Reactor Related Uncertainties

At CHOOZ experiment, the dominant source of systematic uncertainty was the neutrino flux, which amounts to 1.9% [1]. The expected neutrino fluxes at the near and far detectors depend on various factors; the fission rate, the number of neutrinos per fission, the composition of fissile materials in the fuel, and the distance between the reactor and detector and so on. For an experiment with a single reactor, uncertainties from the neutrino flux can be completely

Uncertainty Source	RENO
Reactor Power	0.4
Energy Released per Fission	< 0.1
Reactor/Detector Distances	0.06
Combined	<0.5

Table 8.1: Reactor related systematic uncertainties for RENO.

Uncertainty Source	CHOOZ (%)	RENO (Goal %)
H/C Ratio	0.8	0.1
Target Mass	0.3	0.1
Gd Capture Fraction	1.0	0.4
Positron Energy	0.8	0.1
Positron Geode Distance	0.1	–
Neutron Energy	0.4	0.2
Neutron Geode Distance	0.1	–
Neutron Capture Time	0.4	< 0.1
Positron–Neutron Distance	0.3	–
Dead Time	0	< 0.1
Neutron Multiplicity	0.5	< 0.1
Combined	1.7	< 0.5

Table 8.2: Detector related absolute systematic uncertainty goals for RENO compared with CHOOZ experiment.

removed by using two identical detectors through normalization of the neutrino flux, if the distances between the reactor and detectors are precisely known. However, the Yonggwang power plant has six roughly equally spaced reactors with its span comparable to the distance between the reactor baseline and the far detector. The neutrino flux from each reactor is comparable at the far detector but quite different at the near detector, where the nearest two reactors contributing  $\sim 60\%$  of the total neutrino flux. Therefore, uncorrelated uncertainties among the reactors can be reduced but not as much as the case for having one or two reactors.

### Reactor Power Uncertainties

At Yonggwang power plant, the thermal power of each reactor can be measured better than 1.6% when the power output is above 90% of the rated power output of the reactor [2]. The correlations in the power output measurements among reactors are not yet explicitly investigated.

To be conservative, we assumed no correlations in the reactor power output uncertainty among the reactors and estimated the effects of the uncertainty. Each reactor was assumed to have the same power output as well as the same amount of uncertainty on the power output. The change in the ratio of the number of events detected at the near detector to that of the far detector was numerically calculated when the power output is fluctuated.

Figure 8.1 shows the resulting uncertainty in the ratio of the number of detected neutrino events at a detector at an arbitrary position to that of the near detector, assuming uncorrelated uncertainty of 1%, as a reference, in the power output for each reactor. For the RENO’s far detector position, the uncertainty in the ratio is less than 0.4% for uncorrelated uncertainty of 1.6% in power output in each reactor.

### Energy Released Per Fission

Depending on the composition of fissile materials in the nuclear fuel, the average energy, the number of neutrinos per fission, and the shape of the neutrino spectrum vary. The evolution of the fissile material composition can be calculated using ORIGEN code [3] using the reactor operational conditions and initially loaded fuel composition. The effect is under investigation.

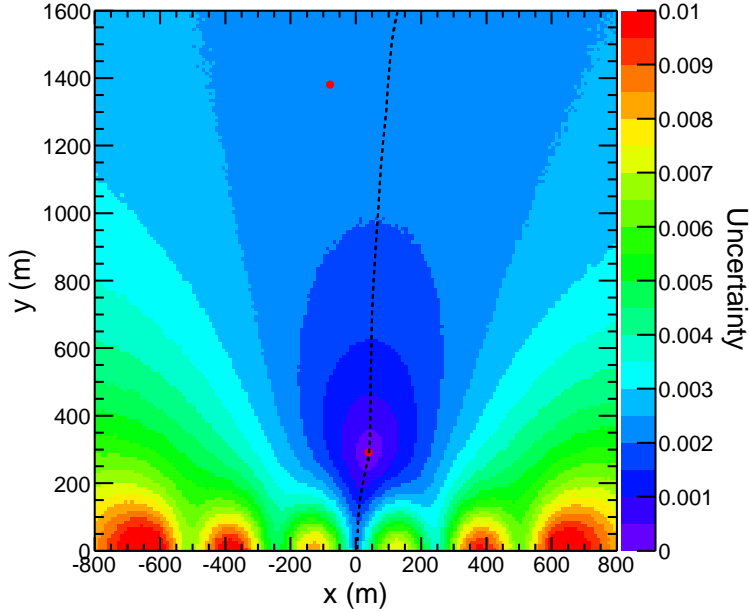


Figure 8.1: The uncertainty of ratio of numbers of events in the near detector to far detector for uncorrelated power uncertainty. The reactor power is assumed to be the same and has an 1% uncertainty as a reference. The red dots represent the locations of the near and far detectors. The dotted line represents the minimum uncertainty at a given distance from the reactor baseline (y-axis).

However, the effect should be minimal since this effect is correlated among reactors.

## Distances

The distances between the center of the fuel assembly in the reactors and the detectors can be determined with a precision better than 10 cm. The barycenter of the neutrino source can change from the fuel load-up over the reactor operation due to fuel burnup. The Burgey experiment was able to determine the barycenter position at a level of a few centimeters laterally [5]. Therefore, uncertainty of 5 cm was used to calculate the effect. The combined uncertainty on the ratio of the event rate at the far detector to that of at the near detector is 0.06%.

### 8.1.2 Detector Related Uncertainties

In CHOOZ experiment, the detector related uncertainty is 1.7%. However, uncertainties are greatly reduced by using two identical detectors at RENO. The relative normalization between the two detectors is the main source of the uncertainties. The liquid scintillator for the near and far detectors will be prepared from a single batch. Therefore, the compositions of the liquids will be, in principle, same for both near and far detectors and there will be no systematic uncertainties originating from the free proton density and the Gadolinium (Gd) concentration.

## Number of Target Protons

The number of observed IBD events in the detector is proportional to the number of free protons in the target. If the ratio of hydrogen to carbon (H/C) is known, the number of free protons can be determined from the target mass. The uncertainty on the target mass can be reduced by the accurate measurement of the target volume and weight.

Since the target liquid will be prepared in a single batch, the chemical compositions of the liquid in the near and far detectors are, in principle, the same. Therefore, the uncertainty in the Hydrogen to Carbon ratio, H/C, will vanish in the normalization. However, we assign 0.1% uncertainty on the H/C measurement which we can achieve with Gas Chromatography-Mass Spectrometer (GC-MS) method.

The target liquid mass will be measured by two methods; mass flow meters and weight sensors. A Coriolis mass flow meter measures the mass and density of the liquid flowing through the device. Commercially available Coriolis mass flow meters have the typical absolute precision of 0.1% and repeatability of  $\sim 0.05\%$ . The weight sensors will be used to cross check the mass flow meters. To maintain a constant fluid density, the variation of the target temperature will be kept under  $1^\circ\text{C}$ . Our goal is to measure the difference between the near and far target masses with an accuracy better than 0.2%.

## Positron Event Selection

If an inverse beta decay event occurs close to the target vessel, sometimes gammas may escape the scintillator volume (target and  $\gamma$  catcher) and not fully deposit energy in the scintillator. However, the effect of geometrical difference of detectors is negligible and the effect of energy scale difference between two detectors is dominant.

We will require the prompt events to have  $> 1$  MeV energy to remove low energy backgrounds. Although the minimum energy from the positron event is 1.022 MeV, the value of measured energy may go below 1 MeV due to energy resolution of the detector. A 2% uncertainty in the energy scale leads to a 0.1% uncertainty in the positron event selection.

## Gadolinium Capture Fraction

The Gadolinium (Gd) concentration of the liquid scintillator in the target affects the neutron capture time as well as the fraction of neutron captured by Gd. The Gd-doped liquid scintillator from the same batch will be used for the near and far detectors. Therefore, as with the H/C, the Gd concentration in the target will be, in principle, identical for both detectors.

The CHOOZ experiment showed that the neutron capture time can be measured at a level of 0.3% [1]. Also, we can measure the neutron capture time using a Californium (Cf) source. Using the same Cf source will allow us to estimate the difference in the fraction of the neutrons captured by Gd between the near and far detectors better than 0.4%.

## Neutron Capture Energy

As with the positron identification, the effect of geometrical difference of detectors is negligible and the effect of energy scale difference between two detectors is dominant. An energy scale uncertainty of 2% gives 0.4% uncertainty in the neutron event selection.

## Neutron Capture Time

The time distribution of neutrons captured by Gd exhibits an exponential like behavior. The mean capture time is  $\sim 30 \mu\text{s}$ . Using the acceptance window of  $0.3 \sim 200 \mu\text{s}$  and the assuming

the time resolution of electronics of  $\sim 10$  ns, we expect the relative uncertainty between near and far detector to be less than 0.1%.

### Neutron Multiplicity

Muon induced spallation neutrons can give multiple neutron capture event and can mimic a signal event. In CHOOZ experiment, such events were removed, resulting in a  $2.6 \pm 0.5\%$  inefficiency. However, RENO detectors have veto layer that can identify such events with a very high efficiency and we consider the uncertainty to be negligible.

### Dead Time Measurement

Due to small overburden, the near detector is expected to experience a large flux of cosmic muons compared to the far detector. This will incur a large fraction of dead time in the near detector to veto the cosmic muons. The dead time for near and far detectors are expected to be  $\sim 25\%$  and  $\sim 4\%$ , respectively, assuming 0.5 ms veto after each muon event. The electronics dead time is expected to be much smaller than the veto caused dead time.

Because the dead time will be significantly different for near and far detectors, it is crucial to measure the dead time precisely to reduce the overall systematic uncertainty. The methods of dead time measurement and its uncertainties are being investigated but the uncertainty is expected to be negligible.

#### 8.1.3 Background Subtraction Uncertainties

The studies on backgrounds are in progress and the uncertainties from the background subtraction will be estimated shortly.

### Spent Fuel

A third of fuel assembly in each reactor at Yonggwang power plant is replaced with a fresh batch about every 18 months. All the replaced spent fuel since the start of the operation of the power plant is stored in on-site water pools located within each reactor complex. Some of fission products in the spent fuel emit neutrinos above 1.8 MeV of energy, which are in equilibrium with long lived predecessors. Therefore, the effect will be present even long after the spent fuel is placed in the pool. The effects of the spent fuel is under investigation.

## 8.2 Sensitivity and Discovery Potentials

### 8.2.1 Experiment Parameters

The average total thermal output of the Yonggwang power plant is 16.4 GW. It is assumed that each reactor has equal thermal power output. The fuel composition is assumed to be constant at 0.556, 0.326, 0.071, and 0.047 for  $^{235}\text{U}$ ,  $^{239}\text{Pu}$ ,  $^{238}\text{U}$ , and  $^{241}\text{Pu}$ , respectively.

Each detector has  $1.2 \times 10^{30}$  free protons in the target vessel with a volume of  $18.7 \text{ m}^3$ . We expect  $4.7 \times 10^5$  and  $4.2 \times 10^4$  inverse beta decay interactions within the target volumes of the far and near detectors, respectively. We assume 40% and 70% event acceptance and selection efficiencies for the near and far detectors, respectively, accounting for the dead time incurred by cosmic muon veto. Therefore, we expect  $5.6 \times 10^5$  and  $8.7 \times 10^4$  events for three years at the near and far detectors, respectively. The reactor-detector distances are shown in Table 8.3 and the detector parameters are summarized in Table 8.4.

	Reactor 1	Reactor 2	Reactor 3	Reactor 4	Reactor 5	Reactor 6
Near	668.9 m	453.2 m	306.9 m	338.0 m	515.2 m	740.0 m
Far	1557.0 m	1456.6 m	1396.4 m	1381.8 m	1414.2 m	1490.5 m

Table 8.3: Reactor-detector distances used in the sensitivity calculation.

	Near	Far
Target Free Protons		$1.21 \times 10^{30}$
Overall Efficiency	40%	70%
Number of events (3 yrs.)	$5.6 \times 10^5$	$8.7 \times 10^4$

Table 8.4: Detector parameters used in the sensitivity calculations. Overall efficiencies include the dead time. The thermal power of each reactor is assumed to be 2.73 GW.

The backgrounds contributions are under investigation and are not included in the sensitivity calculations.

### 8.2.2 Sensitivity

The sensitivity of the experiment to  $\sin^2(2\theta_{13})$  is calculated using the pull approach described in Ref. [4], where the correlations in the uncertainties are naturally accounted for. The  $\chi^2$  function, constructed using positron spectral information, is written as

$$\begin{aligned} \chi^2 = \min_{\alpha} \quad & \left\{ \sum_{d=N,F} \left\{ \sum_{i=1}^{N_b} \left[ \left( \frac{O_i^d - N_i^d}{U_i^d} \right)^2 + \left( \frac{c_i}{\sigma_{shape}} \right)^2 \right] + \left( \frac{b^d}{\sigma_b} \right)^2 + \left( \frac{g^d}{\sigma_{cal}} \right)^2 \right\} \right. \\ & \left. + \left( \frac{a}{\sigma_a} \right)^2 + \sum_{r=1}^{N_c} \left( \frac{f_r}{\sigma_{cfl}} \right)^2 \right\}, \end{aligned} \quad (8.1)$$

where  $O_i^d$  is the number observed events in the  $i$ th bin of the positron energy spectrum of near ( $d = N$ ) and far ( $d = F$ ) detectors, and  $\alpha = \{a, b^d, c_i, f_r, g^d\}$  are the parameters to minimize  $\chi^2$  against. If we define  $T_{ir}^d$  to be the expected number of events in the  $i$ th bin of the energy spectrum on detector  $d$  of positrons originating from reactor  $r$ , then  $N_i^d$  is written as

$$N_i^d = (1 + a + b^d + c_i) \sum_{r=1}^{N_c} (1 + f_r) T_{ir}^d + g^d M_i^d, \quad (8.2)$$

where  $N_c$  is the number of reactors, and  $M_i^d$  is the first order differential of the  $\sum_{r=1}^{N_c} T_{ir}^d$  with respect to  $g^d$ . The uncorrelated uncertainty is

$$U_i^d = \sqrt{O_i^d + B_{ij}^d (1 + \sigma_{bj}^d B_{ij}^d)}, \quad (8.3)$$

where  $B_{ij}^d$  and  $\sigma_{bj}^d$  are the number of events of the  $j$ th background in the  $i$ th energy bin in detector  $d$  and its uncertainty. To estimate the sensitivity of the experiment, we use the expected positron spectrum with oscillation as the observed spectrum. The energy scale uncertainty is accounted for in  $g^d$  to the first order by

$$T_i^d \simeq T_i^d(g^d = 0) + g^d M_i^d, \text{ with } M_i^d = \left. \frac{dT_i^d}{dg^d} \right|_{g^d=0}, \quad (8.4)$$

where  $T_i^d$  is the number of events.

The uncertainty on the overall normalization,  $\sigma_a$ , on the event rates of the near and far detectors accounts for correlated uncertainties and any bias that would affect the near and far detectors in the same way and, therefore, does not degrade the sensitivity of the experiment. This uncertainty is taken to be 2.0%.

The relative uncertainty,  $\sigma_b$ , accounts for uncorrelated uncertainty between the event rates of the near and far detectors. We take 0.6% as the relative uncertainty as shown in Sect. 8.1. The uncorrelated reactor power output uncertainty is taken to be  $\sigma_{cfl} = 1.6\%$  as shown in Sect. 8.1.1,

The uncorrelated bin-to-bin spectrum shape uncertainty is taken to be  $\sigma_{shape} = 2.0\%$  [5]. The energy scale uncertainty is taken to be  $\sigma_{cal} = 1.0\%$ . The uncertainties  $\sigma_{b1}$ ,  $\sigma_{b2}$ , and  $\sigma_{b3}$  are the uncertainties for the fast neutron backgrounds, accidental backgrounds, and cosmogenic isotope backgrounds, respectively.

The  $\chi^2$  is minimized against the parameters  $a$ ,  $b^d$ ,  $c_i$ ,  $f_r$ , and  $g^d$  for a given point in the oscillation parameter phase space. We used energy range from 1.0 MeV to 8.0 MeV with a bin size of 0.25 MeV. Figure 8.2 shows the 90% CL limits on the  $\Delta m_{31}^2$  vs  $\sin^2(2\theta_{13})$  space for three years of data taking. The discovery potential with a  $3\sigma$  significance is also shown in Fig. 8.2. The total efficiencies of 70 and 40% for inverse beta decay events for near and far detectors, respectively, are assumed. Since the background contributions are not yet fully understood, background contributions are not included in this calculations. The limits with the power uncertainty of 0.8% and 3.2% (1/2 and 2 times of the nominal uncertainty of 1.6%) are also shown. For the region of interest,  $\Delta m_{31}^2 = 0.002 \sim 0.003$  eV $^2$ , the expected exclusion region for  $\sin^2(2\theta_{13})$  lies around  $\sin^2(2\theta_{13}) = 0.02$  for the nominal set of uncertainty values. The limit in this region is somewhat sensitive to the reactor power uncertainty worsening by as much as 0.003 for the change in the power uncertainty from 1.6% to 3.2%.

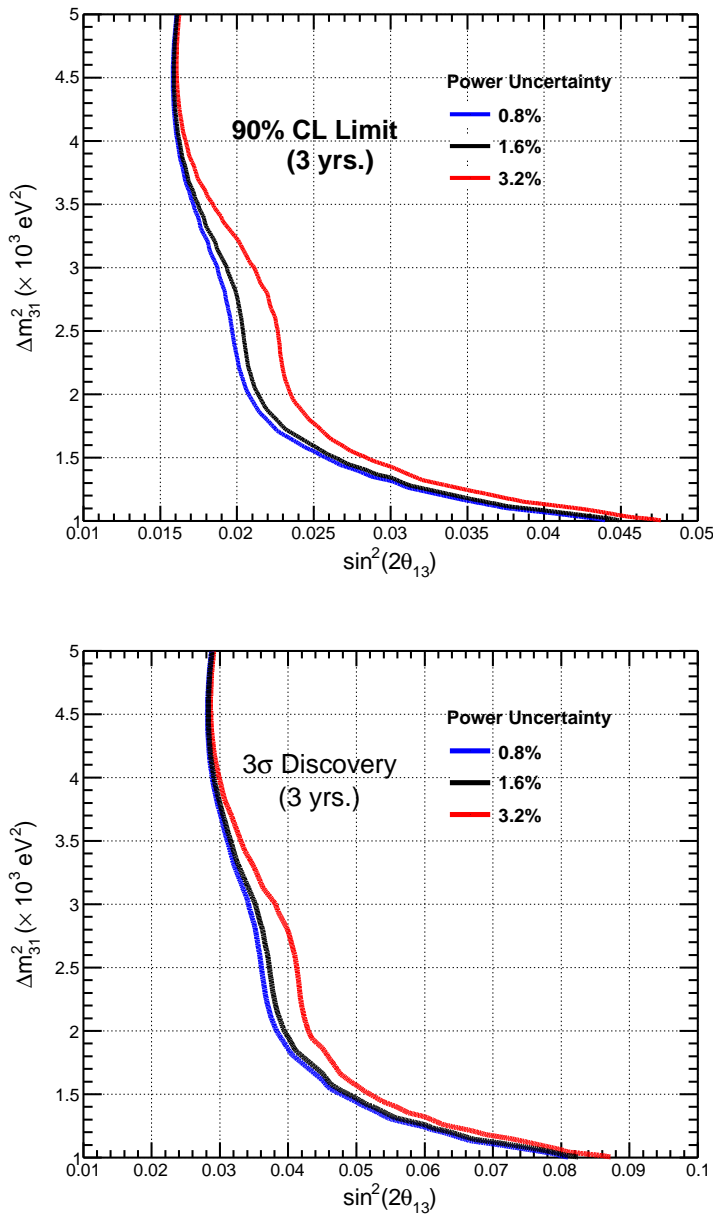


Figure 8.2: Expected 90% CL limits (top) and discovery potential at  $3\sigma$  (bottom) for three years of data taking with the systematic uncertainties given in Tables 8.1 and power uncertainties of 0.8%, 1.6%, and 3.2% for each reactor. The total efficiency of 70 and 40% for inverse beta decay event acceptance for near and far detector are assumed, respectively. Background contributions are not included.

# Bibliography

- [1] M. Apollonio *et al.*, Eur. Phys. J. C **27**, 331 (2003).
- [2] S. K. Ji (Korea Power Engineering Co.), private communications. The power output under a normal reactor operation at Yonggwang is well over 90% of the rated power.
- [3] S. M. Bowman, J. E. Horwedel, I. C. Gauld, and D. L. Barnett, American Nuclear Society/Radiation Protection & Shielding Division, 12<sup>th</sup> Biennial RPSD Topical Meeting, Santa Fe, MN, USA (2001), <http://www.ornl.gov/webworks/cppr/y2001/pres/113173.pdf> *not sure if KEPCO is using ORIGEN-ARP*
- [4] G. L. Fogli, L. Lisi, A. Marrone, D. Montanino, and A. Palazzo, Phys. Rev. D **66**, 053010 (2002).
- [5] Y. Declais *et al.*, Nucl. Phys. B **434**, 503 (1995).